Helsinki University of Technology Control Engineering

Espoo 2008 Report 156

IMPROVING THE PERFORMANCE OF ADAPTIVE OPTICS SYSTEMS WITH OPTIMIZED CONTROL METHODS

Visa Korkiakoski

TEKNILLINEN KORKEAKOULU
TEKNISKA HÖGSKOLAN
HELSINKI UNIVERSITY OF TECHNOLOGY
TECHNISCHE UNIVERSITÄT HELSINKI
UNIVERSITE DE TECHNOLOGIE D´HELSINKI

Helsinki University of Technology Control Engineering

Espoo April 2008 Report 156

IMPROVING THE PERFORMANCE OF ADAPTIVE OPTICS SYSTEMS WITH OPTIMIZED CONTROL METHODS

Visa Korkiakoski

Dissertation for the degree of Doctor of Science in Technology to be presented with due permission of the Faculty of Electronics, Communications and Automation, for public examination and debate in Auditorium AS1 at Helsinki University of Technology (Espoo, Finland) on the 17th of June, 2008, at 9 a.m.

Helsinki University of Technology

Faculty of Electronics, Communications and Automation

Department of Automation and Systems Technology

Distribution:
Helsinki University of Technology
Department of Automation and Systems Technology
P.O. Box 5500
FI-02015 TKK, Finland
Tel. +358-9-451 5201
Fax. +358-9-451 5208
E-mail: control.engineering@tkk.fi
http://www.control.tkk.fi/

ISBN 978-951-22-9411-4 (printed)
ISBN 978-951-22-9412-1 (pdf)
ISSN 0356-0872

Yliopistopaino
Helsinki 2008

Available on net at http://lib.tkk.fi/Diss/2008/isbn9789512294121

ABSTRACT OF DOCTORAL DISSERTATION	HELSINKI UNIVERSITY OF TECHNOLOGY P. O. BOX 1000, FI-02015 TKK http://www.tkk.fi

Author Visa Antero Korkiakoski

Name of the dissertation

Improving the performance of adaptive optics systems with optimized control methods

Manuscript submitted 17.12.2007	Manuscript revised 31.3.2008
Date of the defence 17.6.2008	
[X] Monograph	[ ] Article dissertation (summary + original articles)

Faculty	Faculty of Electronics, Communications and Automation
Department	Department of Automation and Systems Technology
Field of research	Control Engineering
Opponent(s)	Prof. David L Shealy, Prof. Pasi Vahimaa
Supervisor	Prof. Heikki Koivo
Instructor	PhD Miska Le Louarn

Abstract

This thesis investigates control aspects of adaptive optics (AO), a technology to compensate the rapidly changing distortions that affect light after propagating through the turbulent atmosphere. In particular, two different astronomical applications are considered: partial correction of wide fields (needed for surveys) and high accuracy correction of very small fields (needed for detecting faint companions, like exoplanets).

The performance of typical current and future AO systems has been analyzed through numerical simulations, and methods to improve their performance have been studied. In the first part of the thesis, an optimum compensation of wide fields has been shown to be achievable by traditional control methods. The latter part of the thesis concentrates on the nonlinearity issues of a pyramid wavefront sensor (P-WFS) shown in earlier works to be a promising choice for the accurate small field compensation (extreme adaptive optics) due to its better sensitivity for low frequency wavefront distortions.

Two novel methods to deal with the P-WFS nonlinearity effects are presented in this thesis. The first is a theoretical model based and computationally intensive method based on directly inverting the P-WFS signal model. The second method is a heuristic, computationally efficient method combining the a priori information of the atmosphere, the P-WFS signal model and experimentally obtained interaction matrices describing the system behavior.

It is shown in simulations that the latter method, based on compensating the P-WFS loss of sensitivity, dramatically improves the system performance (compared to the conventional AO system control and wavefront reconstruction) in conditions where the measured wavefront aberrations are large (bad seeing and short sensing wavelengths).

Keywords Adaptive optics control, pyramid wavefront sensor, nonlinear control, sensitivity compensation

ISBN (printed) 978-951-22-9411-4	ISSN (printed) 0356-0872
ISBN (pdf) 978-951-22-9412-1	ISSN (pdf)
Language English	Number of pages 127

Publisher Helsinki University of Technology, Department of Automation and Systems Technology

Print distribution

[X] The dissertation can be read at http://lib.tkk.fi/Diss/

VÄITÖSKIRJAN TIIVISTELMÄ	TEKNILLINEN KORKEAKOULU PL 1000, 02015 TKK http://www.tkk.fi

Tekijä Visa Antero Korkiakoski

Väitöskirjan nimi

Adaptiivisten optiikkajärjestelmien suorituskyvyn parantaminen optimoiduilla säätömenetelmillä

Käsikirjoituksen päivämäärä 17.12.2007	Korjatun käsikirjoituksen päivämäärä 31.3.2008
Väitöstilaisuuden ajankohta 17.6.2008	
☒ Monografia	☐ Yhdistelmäväitöskirja (yhteenveto + erillisartikkelit)

Tiedekunta	Elektroniikan, telekommunikaation ja automaation tiedekunta
Laitos	Automaatio- ja systeemitekniikan laitos
Tutkimusala	Systeemitekniikka
Vastaväittäjä(t)	Professori David L Shealy, Professori Pasi Vahimaa
Työn valvoja	Professori Heikki Koivo
Työn ohjaaja	PhD Miska Le Louarn

Tiivistelmä

Väitöskirjassa tutkitaan säätönäkökulmaa adaptiiviseen optiikkaan (AO), tekniikkaan jolla kompensoidaan nopeasti muuttuvia valoon vaikuttavia häiriöitä sen kuljettua läpi turbulentin ilmakehän. Erityisesti käsitellään kahta tähtitieteellistä sovellusta: osittaista laajojen kenttien korjaamista (tarvitaan kartoituksiin) ja hyvin tarkasti tehtävää pienien kenttien korjaamista (tarvitaan himmeiden kiertolaisten kuten eksoplaneettojen valokuvaamiseen).

Tyypillisten nykyisten ja tulevien AO-järjestelmien suorituskykyä on analysoitu numeerisilla simulaatioilla, ja menetelmiä niiden suorituskyvyn parantamiseksi on tutkittu. Väitöskirjan ensimmäisessä osassa laajojen kenttien korjaamisen on osoitettu olevan optimaalisesti saavutettavissa perinteisillä säätömenetelmillä. Jälkimmäinen osa keskittyy epälineaarisuusongelmiin pyramidiaaltorintamasensorissa (PARS), joka on aiemmissa töissä osoittautunut olevan lupaava valinta tarkkaan pienten kenttien kompensointiin (äärimmäinen adaptiivinen optiikka), sillä se on herkkä matalataajuuksisille aaltorintamahäiriöille.

Kaksi uudenlaista menetelmää käsitellä PARS:n epälineaarisuusominaisuuksia on esitetty tässä väitöskirjassa. Ensimmäinen on teoreettinen, mallipohjainen ja laskennallisesti vaativa menetelmä, joka perustuu suoraan inversioon PARS:n signaalimallista. Jälkimmäinen on heuristinen, laskennallisesti tehokas tapa yhdistää a priori informaatio ilmakehästä, PARS:n signaalimalli ja kokeellisesti saatu systeemin toimintaa kuvaava interaktiomatriisi.

Työssä on osoitettu simuloimalla, että tämä jälkimmäinen, PARS:n herkkyyden häviämistä kompensoiva menetelmä, dramaattisesti parantaa järjestelmän toimintaa (verrattuna perinteiseen AO-järjestelmän säätöön ja aaltorintamarekonstruktioon) olosuhteissa, joissa mitattavat häiriöt ovat suuria (huono seeing ja lyhyet mittausaallonpituudet).

Asiasanat Adaptiivinen optiikka, pyramidiaaltorintamasensori, epälineaarinen säätö, sensitiivisyyden kompensointi

ISBN (painettu) 978-951-22-9411-4	ISSN (painettu) 0356-0872
ISBN (pdf) 978-951-22-9412-1	ISSN (pdf)
Kieli Englanti	Sivumäärä 127

Julkaisija Teknillinen korkeakoulu, Automaatio- ja systeemitekniikan laitos

Painetun väitöskirjan jakelu

☒ Luettavissa verkossa osoitteessa http://lib.tkk.fi/Diss/

Preface

This thesis has been carried out in the adaptive optics group at the European Southern Observatory.

Several people have helped me to accomplish this work, but two of them have been of an unique importance: my instructor Miska Le Louarn and an "unofficial" instructor Christophe Vérinaud. I started working with them in 2003 while doing my master's thesis — so they have introduced me to the field and can be considered responsible for practically everything that I know about adaptive optics. Besides, especially Miska Le Louarn has been patient and always available to discuss any of my troubles, and the expertise of Christophe Vérinaud, in particular at the second stage of my thesis dealing with extreme adaptive optics, has been invaluable. Without their extensive support it would have been impossible to carry out this work.

Also a few other people deserve my special gratitude: my former colleague Fernando Quiros-Pacheco, who had many fruitful discussions with me; Rodolphe Conan, whose earlier work at ESO turned out to be very beneficial to me; my colleagues Riccardo Muradore and Richard Clare, who gave constructive suggestions to polish up my manuscript; and — last but not least — Kai Zenger and Heikki Koivo from the Control Engineering Laboratory, who kept me informed about the university issues and supported me remotely from Helsinki.

In addition, I am thankful to the whole adaptive optics group and all the friends I made during my stay in Munich for being a supportive and friendly environment. In such atmoshpere it has been a real pleasure to spend these years!

Garching bei München, Dec 16, 2007

Visa Korkiakoski

Contents

1 Introduction **1**

2 Adaptive optics background **5**
2.1 A summary of adaptive optics 5
2.1.1 History 5
2.1.2 Concepts 6
2.2 Mathematical background 13
2.2.1 Atmospheric effects 13
2.2.2 Image formation 14
2.3 Deformable mirrors 17
2.4 Wavefront sensors 18
2.4.1 Shack-Hartmann sensor 19
2.4.2 Pyramid sensor 20
2.4.3 Pyramid compared with Shack-Hartmann 22
2.5 Adaptive optics simulations 26
2.5.1 Overview 26
2.5.2 OCTOPUS properties 27

3 Adaptive optics control **32**
3.1 Modal compensation 32
3.2 Wavefront reconstruction 36
3.2.1 Truncated singular value decomposition 37
3.2.2 Other approaches 38
3.3 Dynamic control 38
3.3.1 AO system dynamic behavior 39
3.3.2 Optimal modal gain integrator 40
3.3.3 Predictive control 43
3.3.4 State-space formalism 44

4 Simulations of ground layer adaptive optics **46**
4.1 Introduction to GLAO 46
4.1.1 Implementation 46
4.1.2 Laser guide stars 47
4.1.3 Previous work on GLAO 50
4.2 Analytical estimation 51
4.3 Simulations with OCTOPUS 52
4.4 Results 55

4.4.1 Comparison of analytic and numeric GLAO estimates 55
4.4.2 Examples of noisy GLAO cases 60
4.4.3 Effect of the subaperture size, telescope diameter, and outer scale 65
4.5 Conclusions of GLAO simulations 68

5 Optimization of the control of the pyramid sensor for extreme AO 71
5.1 Properties of P-WFS 72
5.1.1 Pyramid sensor in more detail 72
5.1.2 Problems with large phase variations 74
5.2 Model based reconstruction 78
5.2.1 Practical implementation 78
5.2.2 Properties of the Jacobian 80
5.2.3 Application in the AO loop 81
5.3 Simulations of model based control 82
5.3.1 Scope 82
5.3.2 Results 84
5.3.3 Discussion 86
5.4 Sensitivity compensation 87
5.4.1 Overview of the method 87
5.4.2 PSD estimation from closed-loop data 88
5.4.3 Off-line estimation of SCCs with a wave-optics model 90
5.4.4 Update of command matrix with modal sensitivity compensation 91
5.4.5 Optimal control 92
5.5 Simulation of sensitivity compensation 93
5.5.1 Algorithm operation 94
5.5.2 Performance 97
5.6 Conclusions of P-WFS control 99
5.6.1 Success of sensitivity compensation 99
5.6.2 Practical issues 100

6 Future work and conclusions 102
6.1 Future work 102
6.2 Conclusions 105

A Pyramid signal 107

B Pyramid signal linearization 109

C Stellar magnitudes 112

Symbols and Abbreviations

Symbol		Page
α	The amount which a mode is pushed	90
$\boldsymbol{\phi}$	Modal coefficient vector of turbulence	41
$\boldsymbol{\phi}'$	Modal coefficient vector of turbulence in system eigenspace	41
$\boldsymbol{\theta}$	Parameter vector of a predictive controller	43
$\boldsymbol{\varphi}$	A series of modal reconstructions and outputs for a predictive controller	43
ϵ	Estimated residual error	43
$\hat{\phi}$	A statistical realization of residual phase	90
$\hat{\Psi}_0(u, v)$	Complex amplitudes at image plane	14
$\hat{\xi}_i$	Statistically averaged Sensitivity Compensation Coefficient for the ith mode	91
λ_{img}	Imaging wavelength	52
λ_{WFS}	Sensing wavelength	52
$\mathbf{a}$	Vector describing actuator positions when a phase value of given point of the phase grid is modified	82
$\mathbf{c}$	Modal coefficient vector	36
$\mathbf{c}(k)$	Modal coefficient vector at given time instant	92
$\mathbf{c}_1$	Reconstruction vector, conventional	81
$\mathbf{c}_2$	Reconstruction vector, Jacobian	82
$\mathbf{C}_n$	Covariance matrix of noise	38
$\mathbf{C}_\phi$	Covariance matrix of the phase	38
$\mathbf{e}$	Modal coefficient vector of the residual phase	41
$\mathbf{e}'$	Modal coefficient vector of the residual phase in system eigenspace	41
$\mathbf{m}_i^0$	Pyramid sensor measurement without atmospheric residual	90
$\mathbf{m}_i^\phi$	Pyramid sensor measurement with atmospheric residual	90
$\mathbf{n}$	Noise vector	38
$\mathbf{s}$	Measurement vector	36
$\mathbf{s}(k)$	Measurement at given time instant	92
$\mathbf{v}$	Deformable mirror actuator commands	36
$\mathbf{y}(k)$	Modal command vector obtained from a controller	40
$\mathbf{N}'$	Z-transformed noise vector in system eigenspace	41
$\mathbf{N}$	Z-transformed noise vector	41
$\mathcal{W}$	Window function	89
$\mathscr{F}\{\cdot\}$	Fourier transform	51

$\mathscr{F}^{-1}\{\cdot\}$	Inverse Fourier transform	90
ϕ	Phase	32
ϕ'	Modal coefficient of turbulence in system eigenspace	42
$\Psi_0(x, y)$	Complex amplitudes at aperture	14
$\tilde{\phi}_{\mathrm{DM}}$	PSD of deformable mirror shape	89
$\tilde{\phi}_{\mathrm{LF}}$	PSD of the residual phase, defined for lower spatial frequencies	88
$\tilde{\phi}_{\mathrm{resi}}$	PSD of the residual phase	88
$\xi_i(\hat{\phi}(\mathbf{x}))$	Sensitivity Compensation Coefficient of mode i for a residual realization $\hat{\phi}(\mathbf{x})$	91
$A(\mathbf{f})$	Atmospheric transfer function	15
B	Modal interaction matrix	36
$B^{\dagger}$	Modal command matrix	36
$B_m^{\dagger}(k')$	Updated modal command matrix	92
B_z	Zonal interaction matrix	36
$B_z^{\dagger}$	Zonal command matrix	36
C	Scaling parameter proportional to seeing	88
c'	Compensated modal reconstruction coefficient	89
c_x^i	ith P-WFS measurement cross-term element of the x-part	109
c_y^i	ith P-WFS measurement cross-term element of the y-part	109
C_m	Decoupling matrix of the mirror modes	34
c_m	Modal reconstruction coefficient	89
C_N^2	Measure of the turbulence strength	13
c_x	X-part of the pyramid sensor cross-term	80
c_y	Y-part of the pyramid sensor cross-term	80
C_{cosxy}	Cosine of the phase convolved with $1/(xy)$	109
C_{cosx}	Cosine of the phase convolved with $\delta(y)/x$	109
C_{cosy}	Cosine of the phase convolved with $\delta(x)/y$	109
C_{sinxy}	Sine of the phase convolved with $1/(xy)$	109
C_{sinx}	Sine of the phase convolved with $\delta(y)/x$	109
C_{siny}	Sine of the phase convolved with $\delta(x)/y$	109
D	Telescope diameter	16
d	Subaperture grid spacing interval	18
D_ϕ	Atmospheric structure function	51
D_{mx}	X-part of the distance matrix	110
D_{my}	Y-part of the distance matrix	110
e'	Modal coefficient of the residual phase in system eigenspace	42
f	Influence function	17
g	A region of one phase element	82
G'	A loop gain matrix in system eigenspace	41
g'	A loop gain in system eigenspace	42
h_{av}	Average turbulence height	9
H_{cor}	Correction transfer function	42
H_{n}	Noise transfer function	42
H_{ol}	Open loop transfer function	41
h_{sys}	Transfer function of the system	41

$I(r)$	Intensity at the image plane	16
$I_\Psi(x,y)$	Sine of the phase multiplied by the aperture function	108
$J(\cdot)$	The Jacobian matrix of the P-WFS signal function	81
$J^{n,n}(\phi)$	Element of the Jacobian matrix of the P-WFS signal function	80
$J_x^{n,m}(\phi)$	Element of the Jacobian matrix (x-part) of the P-WFS signal function	80
$J_y^{n,m}(\phi)$	Element of the Jacobian matrix (y-part) of the P-WFS signal function	80
$J_{\text{full}}(0)$	The Jacobian matrix of the P-WFS signal function, no approximation	80
$J_{\text{m}}(0)$	The Jacobian matrix of the P-WFS signal function, approximated	80
L_0	Outer scale of turbulence	13
M	Number of modes	41
$M(\mathbf{x})$	Mirror mode shape	32
$M^z(\mathbf{x})$	Zernike mode shape	32
m_x^i	ith two-sided P-WFS measurement element of the x-part	109
m_y^i	ith two-sided P-WFS measurement element of the y-part	109
$m_j(\,\cdot\,)$	Element j of the pyramid sensor measurement	90
m_x	X-signal of the two-sided pyramid wavefront sensor	80
m_y	Y-signal of the two-sided pyramid wavefront sensor	80
N	Number of measurements	90
N_{it}	Number of Jacobian iterations	81
N_a	Number of actuators	36
n_{ph}	Number of photons per subaperture and exposure time	24
p_{obs}	Central obstruction ratio	16
R	Resolution of the discretized phase	78
r_0	Fried parameter r_0	13
R_s	CCD resolution at P-WFS detector plane	81
$R_\Psi(x,y)$	Cosine of the phase multiplied by the aperture function	108
S_x^i	ith four-sided P-WFS measurement element of the x-part	78
S_y^i	ith four-sided P-WFS measurement element of the y-part	78
S_x	X-signal of the four-sided pyramid wavefront sensor	72
S_y	Y-signal of the four-sided pyramid wavefront sensor	72
T	WFS integration time	39
$T(\mathbf{f})$	Telescope transfer function	15
T_{pyr}	Transmittance function of a pyramid sensor	107
$T_{n,m}$	Transmittance function of a pyramid sensor in different quadrants	107
u	spatial frequency, 1st coordinate	14
v	spatial frequency, 2nd coordinate	14
W_ϕ	Power spectrum of phase	51
x	Position, X-coordinate	17
y	A modal command obtained from a controller	43
y	Position, Y-coordinate	17
Z	Mode-to-actuator matrix	36

z	focal length	14
Abbreviation		**Page**
AMA	Amplitude Mask algorithm	73
AO	Adaptive Optics	1
C-WFS	Curvature Wavefront Sensor	18
CAOS	Code for Adaptive Optics Systems	26
CC	Control Computer	39
CIBOLA	Covariance, Incorporating Basic Option for Linear, Analysis	26
DAC	Digital to Analog Converter	39
DM	Deformable Mirror	1
E-ELT	European Extremely Large Telescope	6
ELT	Extremely Large Telescope	6
EPICS	Exo-Planets Imaging Camera and Spectrograph	25
ESO	European Southern Observatory	2
FA	Focus Anisoplanatism	48
FFT	Fast Fourier Transform	27
FFTW	Fastest Fourier Transform in the West	27
FOV	Field of View	68
FT	Fourier transform	15
FWHM	Full Width at Half Maximum	16
GLAO	Ground Layer Adaptive Optics	1
GS	Guide Star	9
GTC	Gran Telescopio Canarias	6
GUI	Graphical User Interface	26
HET	Hobby-Eberly Telescope	6
HOT	High Order Testbench	20
HVA	High Voltage Amplifier	39
IDL	Interactive Data Language	26
JR	Jacobian reconstruction	71
K-L	Karhunen-Lóeve	33
LBT	Large Binocular Telescope	6
LGS	Laser Guide Star	47
LMS	Least Mean Squares	36
LQG	Linear-Quadratic-Gaussian	44
LZT	Large Zenith Telescope	6
MAD	Multiconjucate Adaptive optics Demonstrator	50
MAP	Maximum a posteriori	38
MCAO	Multi Conjugate Adaptive Optics	9
MIMO	Multiple Inputs, Multiple Outputs	41
MMT	Multiple/Magnum Mirror Telescope	6
MPI	Message Passing Interface	27
MVM	Matrix-Vector-Multiplication	31
NAOS	Nasmyth Adaptive Optics System	40
NGS	Natural Guide Star	47
OCTOPUS	Optimized Cluster Tool for adaptive Optics Parallel Unlimited Simulations	3

OMGI	Optimal Modal Gain Integrator	40
OMI	OCTOPUS Matlab Interface	27
OPD	Optical Path Difference	8
OWL	Overwhelmingly Large Telescope	26
P-WFS	Pyramid Wavefront Sensor	2
PAOLA	Performance of Adaptive Optics for Large Apertures	26
PMA	Phase Mask algorithm	73
PSD	Power Spectral Density	85
PSF	Point Spread Function	14
rms	Root mean square	13
RTC	Real Time Computer	6
SALT	Southern African Large Telescope	6
SCAO	Single Conjugate Adaptive Optics	9
SCC	Sensitivity Compensation Coefficient	87
SH-WFS	Shack-Hartman Wavefront Sensor	2
SVD	Singular Value Decomposition	37
T-SVD	Truncated Singular Value Decomposition	37
TMT	Thirty Meter Telescope	6
VLT	Very Large Telescope	6
VWGLAO	Very Wide Ground Layer Adaptive Optics	46
WCOG	Weighted Center Of Gravity	19
WFS	Wavefront Sensor	1
XAO	Extreme Adaptive Optics	2

Chapter 1

Introduction

Adaptive optics (AO) is a technology used to compensate in real time the aberrations that occur when light propagates through an inhomogeneous medium. Currently its most important applications are in astronomy and in military applications (Roddier, 1999a), although also medical uses are becoming more common (Chen et al., 2007).

Designing and building an AO system requires expertise from many fields besides astronomy — optics, electrical and mechanical engineering, computer science and control theory. The idea of AO was first mentioned in 1950s (Babcock, 1953). However, it was not until 1970s before sufficiently sophisticated technologies became available at military fields (Tyson, 1991). The first successful AO systems were applied in the major astronomical telescopes at the beginning of the 1990s (Rousset and Beuzit, 1999).

The celestial light coming from a very distant object forms a plane wavefront. When it propagates through the atmosphere, differences in the refractive index of air cause the shape of the wavefront to change. The device measuring these deformations is called a wavefront sensor (WFS).

Currently the main AO solutions are based on a closed-loop operation: the celestial light is reflected from a deformable mirror (DM) and one part of this residual light is directed to a scientific camera, one part to the WFS. The sensor measures the wavefront distortions and the measurements are fed to a control system that computes new commands to be sent to the mirror. The mirror then adapts to further reduce the residual distortions. This process thus iteratively compensates the atmospheric effects.

The first generation AO systems have been designed to use a single DM and single WFS. They are able to compensate the field near the imaged object (up to a few arcseconds at near infrared), but not much further. In addition, the AO correction in the first astronomical applications is done using a low number of degrees of freedom. As a consequence, the stellar halo (light originating from the star) is not completely compensated — and the imaging of faint companions is difficult. Thus, although the scientific results of AO have been remarkable, its use is restricted only to a limited set of observations.

To enhance the possibilities of ground-based astronomy, several new AO concepts have been proposed and studied. For instance, to enable wide field surveys, so-called ground layer adaptive optics (GLAO) has been proposed to correct a very wide field (Rigaut, 2002). Most of the atmospheric turbulence is located in the lowest layers

of the atmosphere. Therefore, it is possible to achieve a partial correction over a wider field, if only this ground layer is compensated. This requires a compromise — the larger the compensated field, the worse is the image resolution.

However, in some cases — for instance, when imaging the faint companions of distant stars — it is necessary to obtain the best possible image quality. This requires a dense sampling of measured and corrected wavefront. Applications intended for this purpose are often classified as extreme adaptive optics (XAO). For an 8 meter telescope it means a wavefront measurement resolution of at least 40×40 — the wavefront is measured with an accuracy of 40×40 elements, each corresponding to an area of 20×20 cm^2.

At the European Southern Observatory (ESO), two second generation (for 2011–2012) instrument projects based on these AO concepts are currently being designed: MUSE, an instrument dedicated to large extragalactic structures will use GLAO (Henault et al., 2004), while SPHERE (exoplanets direct imaging) will use XAO (Beuzit et al., 2006). MCAO (multi-conjugate AO) and MOAO (multi-object AO) are two other wide field AO concepts, but there are currently no plans at ESO for VLT instruments based on these concepts.

This thesis concentrates on the control aspects of the two AO concepts: GLAO and XAO. Although the concepts share also a lot of common ideas and the same linear control strategies have been applied in both cases (Le Roux et al., 2004; Looze, 2006), notable differences exist.

Since the goals of these concepts are so different, different control strategies are required. For instance, the GLAO control can not be unambiguously optimized to minimize the residual variance — one must also pay attention to the correction uniformity. When considering XAO, the properties of the wavefront sensor become crucially important: the sensors enabling best sensitivity tend to be nonlinear at high wavefront distortions. Thus, additional control strategies might be required to control these nonlinearity properties.

The first wavefront sensors were derived from the classical devices used in optical testing (Rousset, 1999). One of the most common sensors is the Shack-Hartmann WFS (SH-WFS) that measures the local derivative of the wavefront.

The SH-WFS, unfortunately, has some fundamental properties making its use in the XAO applications, especially with the next generation large telescopes, less optimal. For instance, to reach a good spatial resolution with SH-WFS, the incoming wavefront must be split into several independent images. This is shown to decrease the measurement accuracy, especially at the lower spatial frequencies (Vérinaud, 2004; Guyon, 2005; Chew et al., 2006). And this, consequently, would mean an inferior performance when imaging objects near a bright on-axis star.

Thus, other novel approaches for wavefront sensing have been presented. These include, for instance, a pyramid WFS (P-WFS) (Ragazzoni, 1996) and focal plane wavefront sensing (Guyon, 2005).

At the moment P-WFS is the most popular alternative to the SH-WFS. Its better sensitivity compared to SH-WFS has been the most important motivation of developing the new sensor. All later descriptive studies (Ragazzoni and Farinato, 1999), numerical analyzes (Esposito et al., 2000b; Esposito and Riccardi, 2001; Clare and Lane, 2004; Chew et al., 2006; Vérinaud, 2004; Vérinaud et al., 2005) and

practical experiments (Esposito et al., 2000a,b; Burvall et al., 2006; Ghedina et al., 2003; Feldt et al., 2006) have supported the theory indicating P-WFS advantages over SH-WFS.

One disadvantage of the P-WFS is its nonlinearity. If the measured wavefront distortions are too high, the sensor saturates. So far, only few studies concerning this issue have been published. Thus, one of the major aims of this thesis is to seek possibilities to compensate the P-WFS nonlinearity effects.

The work for the thesis is carried out using only numerical methods. The aim is mainly to demonstrate the feasibility of general control and reconstruction approaches. Although the work is not dedicated for any specific instrument, the simulation parameters are typically chosen to describe the current facilities available at ESO. However, the ultimate goal of the thesis is to give guidelines and ideas for the next generation instruments seeing their first light in 10–20 years.

The major tool for our numerical analysis is the Monte Carlo simulation tool developed at ESO: OCTOPUS (Optimized Cluster Tool for adaptive Optics Parallel Unlimited Simulations). It has been gradually implemented since 2002 (Le Louarn et al., 2004a) and significant improvements were carried out to accomplish the work required in this thesis.

Next the content of the thesis is briefly summarized.

Chapter 2 gives a short introduction to adaptive optics for astronomy. The basic ideas for GLAO and XAO are illustrated. Also the mathematics of the light propagation through the atmosphere and image formation is briefly summarized. The differences of the popular wavefront sensors, SH-WFS and P-WFS, are described in more detail. Also ESO's simulation tool, OCTOPUS, is described at length.

In Chapter 3 the standard approaches for adaptive optics control and wavefront reconstruction are discussed. The most emphasis is given to the well-known approaches used widely in the implemented AO systems: truncated singular value decomposition, optimal modal gain integrator and modal predictive control. However, some even more sophisticated, well known, methods do exist and their potential is briefly discussed.

Chapter 4 discusses GLAO in more detail. The concept is described and a short summary of the earlier work on GLAO is given. Then we illustrate the GLAO performance in selected difficult cases and compare the numerical Monte Carlo results with analytic estimates. Based on this, conclusions for the necessity of more advanced control methods for GLAO are drawn.

Chapter 5 is devoted to the control of P-WFS. At first, a novel reconstruction method for the P-WFS is illustrated. That is an iterative, model-based approach and difficult to implement in real time systems. However, important conclusions from its performance can be made. Then, partially based on these conclusions, a more practical reconstruction/control approach is presented. Its feasibility is also demonstrated in extensive end-to-end AO simulations.

The conclusions are given in Chapter 6.

The main contributions of this thesis can be summarized as follows:

- The parallel adaptive optics simulation software at ESO has been significantly developed. At first, codes involving simulations having operations in Fourier space (e.g., a spatial filter for SH-WFS) have been written and optimized

enabling comparisons between SH-WFS and P-WFS with large systems. This work has been applied, for instance, in (Vérinaud et al., 2005).

- The whole functionality involving operations in modal base has been added to the simulation tool. This code had been used throughout the thesis.

- Extensive study on GLAO has been carried out. The results verify that ESO's simulation tool is compatible with what has been known: fast analytic codes give comparable results to the numerical Monte Carlo simulations and GLAO is very robust in closed-loop operation. In addition, this study highlights the GLAO performance with ELTs. These results are published in a SPIE conference (Korkiakoski et al., 2006).

- A novel model-based wavefront reconstruction method for nonmodulated P-WFS is presented. It is based on computing successive linearizations of the signal and representing them as Jacobian matrices. This method, when used iteratively, can be used to compensate the sensor nonlinearities that a simple linear approach is not able to handle. Thus, the achieved reconstruction is the ultimate limit of the P-WFS — when no prior information about the wavefront is used. It is then shown in simulations that in typical closed-loop operation this nonlinearity compensation gives only a negligible advantage compared to the linear approximation of the sensor. Nevertheless, the Jacobian reconstruction performs better compared to conventional approaches suggesting there is a more practical way to improve wavefront reconstruction. The concept of the Jacobian reconstruction is published in (Korkiakoski et al., 2007b).

- Another novel reconstruction method for P-WFS, published in (Korkiakoski et al., 2008), is presented. It was motivated by the previous study and the observation that in difficult conditions the reconstructions of certain modes become underestimated (i.e., seen with a reduced sensitivity). The method is based on compensating this loss of sensitivity and requires an internal model of the used sensor and an on-line estimation of the present seeing conditions. It is shown in simulations that the method outperforms dramatically the conventional approach, when a nonmodulated P-WFS is studied in difficult conditions (bad seeing, short sensing wavelength). In addition, the method can be applied as such for any sensor whose model is known.

Chapter 2

Adaptive optics background

This chapter describes the major concepts and definitions of adaptive optics, concentrating on the applications in astronomy.

At first, the history and most common concepts of AO are described in Section 2.1. Then, the necessary mathematical background — effects of the atmospheric turbulence and image formation — are discussed in Section 2.2.

The most important aspects of the AO are then discussed at length in their own sections: deformable mirror technology in Section 2.3 and wavefront sensors in Section 2.4.

Finally, in Section 2.5, we discuss the AO simulations. The most common simulation tools are listed and ESO's OCTOPUS is described in more detail.

2.1 A summary of adaptive optics

2.1.1 History

After the invention of telescopes by Galileo Galilei in the early 1600s, optics developed steadily. By the 20th century the astronomical imaging devices had reached the point where the turbulent atmosphere was the ultimate limit of the image quality. Enlarging the telescope sizes beyond 20 cm did not increase the image resolution.

However, building larger and larger telescopes was necessary to collect more light to image dimmer objects. This evolution was marked by a steady increase of the apertures, and the major optical telescopes reached the size of over 4 meters by the 1950s.

To further increase the telescope sizes, a technology called *active optics* was developed. The conventional approach was building the structures so stiff that no variations in the telescope mirror were present. However, for larger sizes this became impractical. Instead, mechanics were used to dynamically adjust the primary mirror to compensate variations caused by temperature changes, wind, and so on. This enabled making the mirrors and the telescope structures much lighter and thus building them more inexpensively. However, the mirror shape update rate in active optics, about 1 Hz, was far too low to compensate the atmospheric turbulence itself.

Nevertheless, adaptive optics — a technology to compensate the turbulence itself — was first proposed the 1950s (Babcock, 1953), but the extremely challenging

technological requirements prevented its practical implementation for many decades. It was not before 1970s when military applications, for instance the imaging of artificial satellites and the concentration of laser beams to remote objects, triggered serious research in AO. By the end of 1970s several AO systems were widely used for defense applications. Meanwhile, astronomers were concentrating on post-processing techniques to improve the image quality (Roddier, 1999c).

However, inspired by the military success, astronomers became interested in applying AO to astronomy. Unfortunately, some aspects of their requirements were much harder, since most of the astronomical objects are much dimmer than the artificial satellites. Therefore, it took still another decade before the first purely scientific AO applications saw their first light.

Since the middle of the 1990s AO has been in regular use in most of the major astronomical sites worldwide, and the field is constantly growing as more and more sophisticated technologies are developed.

Currently, the largest optical telescopes have a diameter of about 10 m. This has been achieved by compiling the mirror from several smaller pieces — the available technology enables manufacturing single mirrors of having a diameter only 8 meters. The list of the largest optical telescopes is shown in Table 2.1. Several of these have at least one adaptive optics system currently installed, for instance, MACAO and NACO at Very Large Telescope (VLT) (Paufique et al., 2006; Clenet et al., 2004), Altair at Gemini (Stoesz et al., 2004b) and Keck AO (van Dam et al., 2004). Also other smaller telescopes, for instance the Shane 3-meter Telescope at Lick Observatory, have advanced AO instruments available (Bauman et al., 2002).

In the future, several radically larger telescopes have been planned. These are usually referred as Extremely Large telescopes (ELT). These include, for instance, the Thirty Meter Telescope (TMT) of a few American institutes (Nelson and Sanders, 2006) and the European ELT (E-ELT) of ESO (Gilmozzi and Spyromilio, 2007).

2.1.2 Concepts

The traditional AO is designed to compensate the field near the imaged target. A typical classical AO system consists of the following components: a deformable mirror (DM), wavefront sensor (WFS), real time computer (RTC). Those are illustrated in figure 2.1.

A distorted wavefront comes into the system through the telescope aperture. It is reflected from a deformable mirror to a beam splitter that divides the beam to a WFS and a scientific camera. The measurements from WFS are fed to a RTC that computes the required instructions for the DM. The mirror is deformed using actuators, each of them having its own control voltage.

The cycle from the WFS measurements to the mirror commands becomes typically an iterative process called closed-loop.

Figure 2.2 illustrates the effect of a typical first generation AO system in an 8 meter telescope. Without the AO correction, a short-exposure image of a point source breaks into a random pattern of small fragments, called *speckles* (see the left image in figure 2.2).

Table 2.1: A list of major optical telescopes

Name	Site	Size	Built
LBT[a]	Mount Graham, Arizona	2×8.4 m	2007
SALT[ab]	Karoo, South Africa	11.0 m	2005
GTC[ab]	Roque de los Muchachos, Canary Islands	10.4 m	2006
Keck 1[b]	Mauna Kea, Hawaii	10.0 m	1993
Keck 2[b]	Mauna Kea, Hawaii	10.0 m	1996
HET[b]	McDonald Observatory, Texas	9.2 m	1997
Subaru	Mauna Kea, Hawaii	8.3 m	1999
VLTs	Paranal, Chile	4×8.2 m	1998–2001
Gemini North	Mauna Kea, Hawaii	8.1 m	1999
Gemini South	Cerro Pachón, Chile	8.1 m	2001
MMT	Fred Lawrence Whipple, Arizona	6.5 m	1987/2002
Magellan 1	Las Campanas, Chile	6.5 m	2000
Magellan 2	Las Campanas, Chile	6.5 m	2002
BTA-6	Zelenchukskaya, Caucasus	6 m	1976
LZT	Maple Ridge, British Columbia	6 m	2003
Hale	Palomar, California	5 m	1948
William Herschel	Roque de los Muchachos, Canary Islands	4.2 m	1987
SOAR	Cerro Pachón, Chile	4.2 m	2002

[a]Not yet fully operational, [b]Mosaic telescope

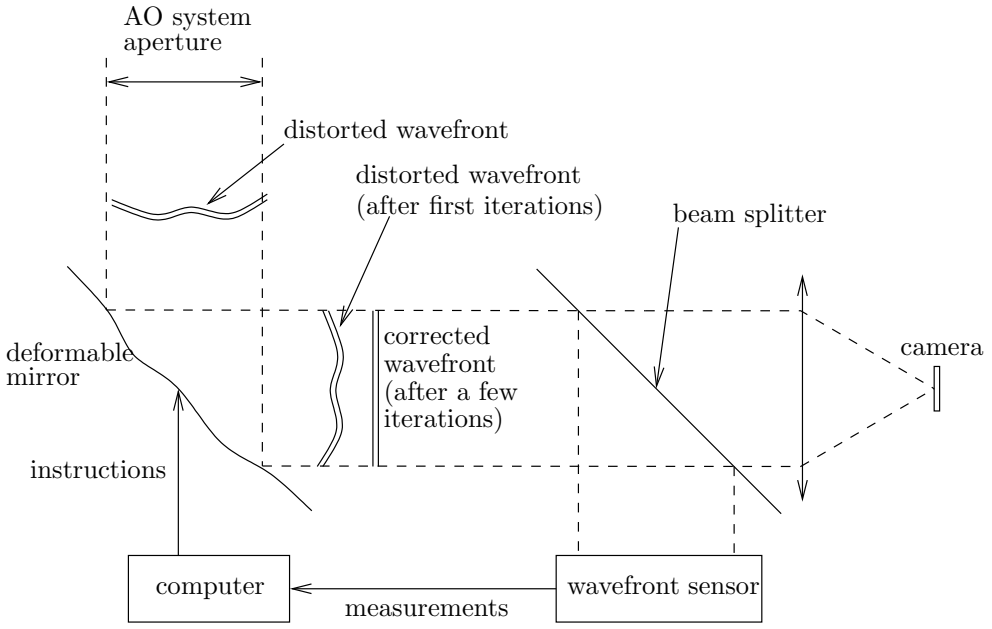

Figure 2.1: Concept of an AO system in closed-loop.

When the image is integrated longer, the speckle pattern becomes a blurred disk, whose width depends on the strength of the turbulence (see the middle image in figure 2.2). When real time AO correction is applied, the long exposure image has a much narrower disk, as shown in the right image in figure 2.2.

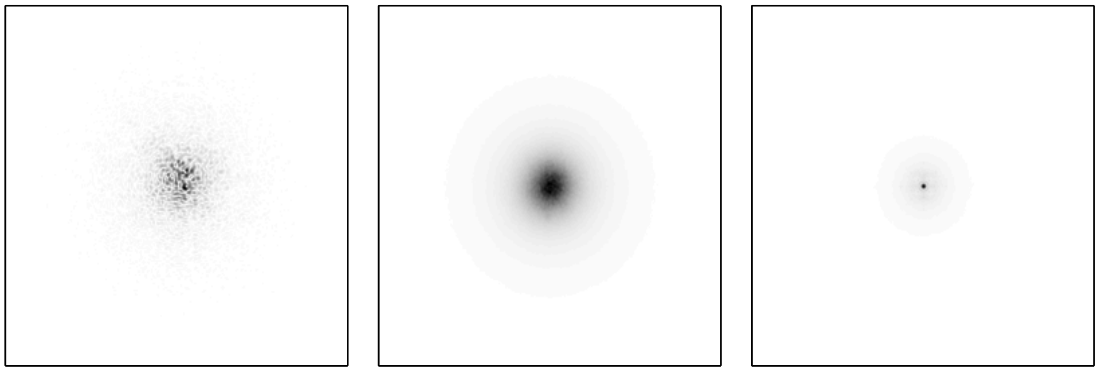

Figure 2.2: Simulation of atmospheric imaging with an 8 meter telescope, medium seeing (0.7" at 0.5 μm) and 1.6 μm imaging wavelength. Images are shown using a nonlinear scaling. Left: simulated short exposure image without AO correction. Middle: the long exposure image of the same star (10 s integration). Right: AO corrected long exposure image.

Obviously, the more AO corrects the blurring effect, the better is the image quality. In addition, also another beneficial effect is obtained. Since the light from the star is concentrated much better on a narrower area, the blurring effects of the speckles are less severe. This enables shorter exposure times to reach the same flux on star — and thus the telescope can be used more efficiently.

The image quality in astronomy is determined by the width of the spot of a distant point source (e.g., a star). This changes a lot depending on the atmospheric turbulence and is called *seeing*. The image quality also depends on the used wavelength (λ): the phase in radians is proportional to $2\pi/\lambda \cdot \mathrm{OPD}$, where the optical path difference (OPD) describes the shape of the wavefront in meters. Thus, at longer wavelengths there are smaller phase variations.

In astronomy, the size of the seeing spot is usually expressed in arcseconds for the wavelength of the visible light (0.5 μm). At high mountains in ideal conditions the seeing reaches 0.4–0.7". In bad conditions or at lower altitudes it climbs up to 2.5–4".

The first AO systems at large (4–10 m telescopes) were, in the ideal conditions, able to reduce the seeing spot down to the ultimate (diffraction limited) size determined purely by the telescope diameter (Roddier and Rigaut, 1999; Rousset and Beuzit, 1999). This required a medium seeing and a suitable imaging wavelength (1.6–2.2 μm). The spot size at this wavelength was reduced roughly from 0.6" to below 0.2".

However, these achievements required a bright reference object to measure the incoming wavefront appropriately. Such objects are relatively rare on sky and this leads to restricted *sky-coverage* — typically only about 1% of the sky is available

for traditional AO. This issue is expected to improve with the use of artificial laser beacons discussed later in Section 4.1.2.

In addition, the first generation AO systems were able to correct only a small part of the imaged field. This happens since the AO correction is done only in one direction. Light coming further from this direction (from other stars), experiences a different optical path (see figure 2.3).

Depending on the type of use, AO is divided into sub-categories. Classical AO is often referred as single conjugate AO (SCAO). Newer techniques involving a wide field of view AO correction are multi-conjugate AO (MCAO) and ground layer AO (GLAO). Systems designed to achieve a very good AO correction near the imaged star are classified as extreme AO (XAO).

MCAO and GLAO

In SCAO the compensation is done according to the wavefront from the reference star (called also *guide star*, GS). Therefore, as mentioned, one cannot properly image the objects having too large angular distance to the GS. This causes the field becoming non-uniformly compensated and is called *angular anisoplanatism* (see figure 2.3).

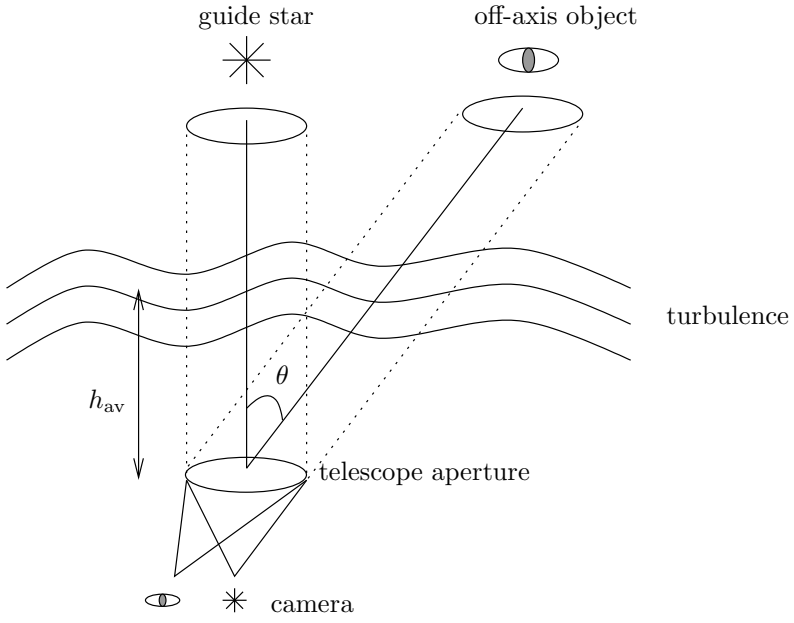

Figure 2.3: Illustration of angular anisoplanatism.

Light coming from an off-axis object experiences a different OPD compared to the reference star. This difference causes anisoplanicity error that depends on the angle θ and turbulence strength and profile. The angle θ_0 that lets the root mean square of the anisoplanicity error be 1 radian, is defined as *isoplanatic angle*. For a guide star in zenith it is shown to be (Roddier, 1999a)

$$\theta_0 = 0.314 \frac{r_0}{h_{\mathrm{av}}}, \tag{2.1}$$

where r_0 is the Fried parameter describing the strength of the turbulence (see Section 2.2) and h_{av} is a weighted average of the heights of the turbulent atmospheric layers.

Many astronomical observations, such as galaxy surveys for instance, require a wide field with good uniform image quality. Thus, currently AO can be used only with a fraction of the astronomical observations and bad seeing can be a significant nuisance for the ground based non-AO observations.

To achieve a correction over a wider field, MCAO and GLAO systems are designed to measure the turbulence along several directions. In this way it is possible to increase the uniformly corrected field at the expense of the maximal image resolution.

Both in MCAO and GLAO, several WFSs (except the layer-oriented approach (Nicolle, 2006) not considered in this thesis) are used to obtain knowledge of the turbulence over a large volume instead of the single direction of the reference source. In MCAO several DMs are then used to compensate over a medium field of view (up to 1–2'). In GLAO only one DM is used and a significantly larger corrected field is obtained (up to 4–8').

MCAO is demonstrated in figure 2.4. The images are taken at the VLT using ESO's Multi-conjugate Adaptive optics Demonstrator (MAD) (Marchetti et al., 2007). The large image is mosaic of images covering the central parts of Omega Centauri, the most luminous globular cluster as seen from Earth (total width 2 arcmins). The images were taken with CAMCAO (using an imaging wavelength of 2.166 μm) for a total exposure time of 5 minutes (the original pixel scale is 0.028 arcsec). The stars in the 2' field of view have a spot size between 0.08 and 0.10 arcsec.

The guide stars used for the MCAO correction are identified with a cross. The box shows a 14 arcsec area that is then observed while applying different or no AO corrections, as shown in the bottom images. This demonstration illustrates that SCAO has very little effect in sharpening the star images in this region (it helps only near the GS) while MCAO is expected to be able to reveal several new stars.

In this thesis, however, only GLAO is considered in more detail. Since it corrects a significantly larger field compared to MCAO, also the image quality of GLAO is worse. MCAO, on the other hand, is able to produce — in good conditions — diffraction limited images on a relatively small field.

The main goal of GLAO is to concentrate the star light to achieve a reduced spot size. Although the improvement of the image resolution is not dramatic, GLAO is expected to significantly increase the telescope utilization rate — observations at worse seeing become possible and shorter exposure times can be used. This can improve the efficiency of an instrument like MUSE by almost a factor of 2.

Extreme AO

Another regime of AO, namely imaging the immediate proximity of a star, is also interesting for some astronomical observations: the detection of faint companions around their host stars. Traditional AO is often insufficient for this purpose — the first generation AO systems are designed to barely reach the diffraction limit of the telescopes.

XAO, on the other hand, provides a much better turbulence compensation. The wavefront — from the direction of interest — is corrected well enough to almost reach the ideal quality of the space telescopes. This means that besides the diffraction

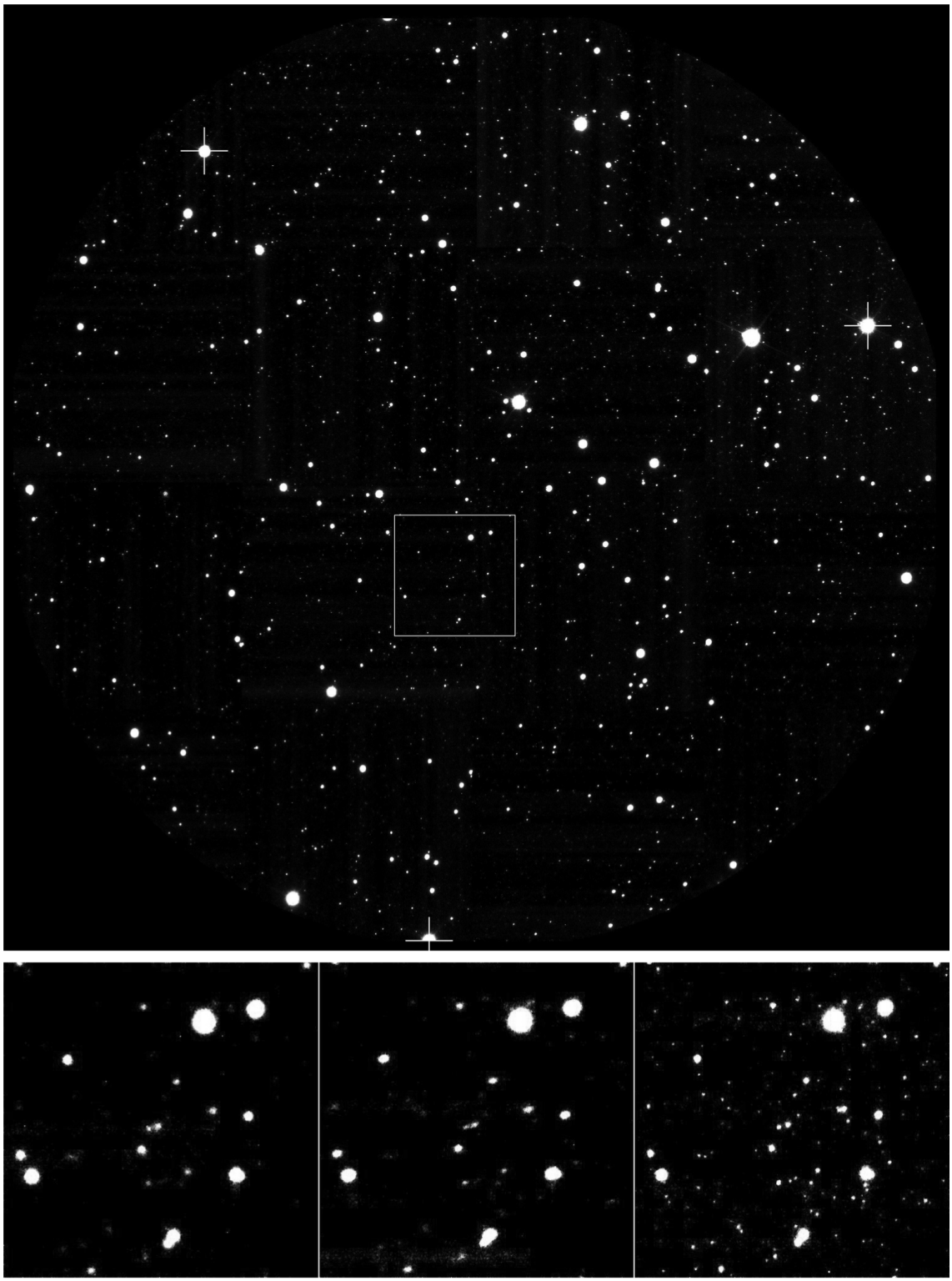

Figure 2.4: Demonstration of MCAO. The images are from ESO's press release 30.3.2007. See the details in text. The smaller pictures from left to right: without AO, SCAO and MCAO.

limited resolution, most of the star's *halo* (stellar light forming a pattern around the imaged star) is concentrated on the diffraction spot — and is not polluting the exoplanet detection.

This means that the measurement and correction must be done with an extremely good resolution: measurement resolution at least 40×40 with an 8 meter telescope (wavefront sampled with 40×40 elements, each corresponding to an area of 20×20 cm^2). This can be compared to a typical resolution of 14×14 in the first generation AO systems. However, the system components in XAO are identical to the conventional SCAO — no additional WFSs or DMs are needed as in MCAO or GLAO.

On the other hand, in XAO it is necessary to take care of the WFS properties. In high resolution imaging, the differences in the used sensor type can be significant. This is illustrated, for instance, in figure 2.5, where the AO corrected images of a P-WFS and SH-WFS are compared in an XAO case (a very good AO compensation, about 10 diffraction rigs are visible). It can be seen that the AO corrected basin in the right image is partially filled, because the Shack-Hartmann sensor is more susceptible to aliasing.

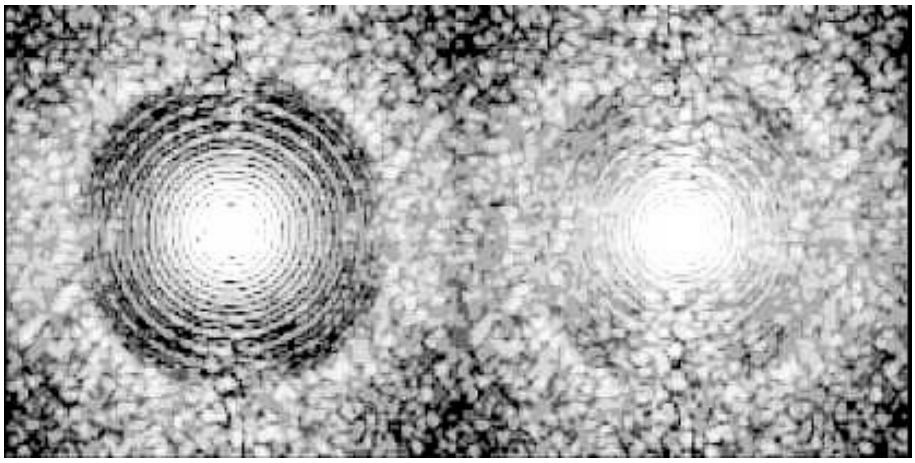

Figure 2.5: Illustration of WFS differences with XAO. Two simulated AO corrected images of stars are shown. Left: pyramid WFS. Right: traditional Shack-Hartmann WFS. Images are from (Vérinaud et al., 2004).

In addition to careful WFS optimization, typical XAO applications need coronagraphs to detect exoplanets. A coronagraph is a device damping the light originating from a central star thus enabling a better imaging of its companions. Although a preliminary implementation of such was done for the simulation tool used in this thesis (Korkiakoski, 2004; Korkiakoski et al., 2004), the coronagraphic imaging is outside the scope of our main interests and we discuss it no further.

Current (and near-future) XAO systems include the Gemini Planet Imager (Macintosh et al., 2006) and the SPHERE instrument for the VTL (Beuzit et al., 2006). Those are designed to be used with spatially filtered SH-WFSs as explained later in Section 2.4.1.

However, as described in Section 2.4.3, the pyramid sensor has advantages com-

pared to the SH-WFS (e.g., less susceptible to aliasing, more sensitive to low frequency wavefront aberrations). This makes it a tempting choice for the next generation XAO systems — especially if its nonlinearity issues can be solved.

2.2 Mathematical background

This section describes the mathematical background used to describe the effects of the atmosphere and how AO can compensate them.

2.2.1 Atmospheric effects

At first, a good model of the atmospheric effects on astronomical imaging is required to evaluate the compensation. Such models have been constructed since the 1960s (Fried, 1965), and they have remained unchanged.

The speed of light in the atmosphere is affected by local temperature variations. Therefore, the phase of the light wave, $\phi(\mathbf{x})$, after going through the atmosphere is a function of the refractive index $n(z)$ at the altitude z

$$\phi(\mathbf{x}) = \int \frac{2\pi}{\lambda} n(z) \mathrm{d}z, \tag{2.2}$$

where integration is made along the light path, $\mathbf{x}$ describes position and λ is the wavelength. A more interesting measure is the variance of $\phi(\mathbf{x})$ fluctuations. It can be represented by a *structure function* (function of the distance $\boldsymbol{\xi}$ between two positions) as

$$D_\phi(\boldsymbol{\xi}) = \left\langle |\phi(\mathbf{x}) - \phi(\mathbf{x}+\boldsymbol{\xi})|^2 \right\rangle, \tag{2.3}$$

where the brackets $\langle\cdot\rangle$ represent an ensemble average.

A further formula can be written using the Kolmogorov-Obukhov law of turbulence. It states that the variance of the difference between two values of refractive index is given by

$$D_N(\boldsymbol{\rho}) = \left\langle |n(\mathbf{r}) - n(\mathbf{r}+\boldsymbol{\rho})|^2 \right\rangle = C_N^2 |\boldsymbol{\rho}|^{2/3}, \tag{2.4}$$

where C_N^2 is a measure of local inhomogenities of the atmosphere. Substituting equation (2.2) into equation (2.3) and using equation (2.4), $D_\phi(\boldsymbol{\xi})$ can be written as (Roddier, 1999a)

$$D_\phi(\boldsymbol{\xi}) = 6.88 \left(|\boldsymbol{\xi}|/r_0\right)^{5/3}, \tag{2.5}$$

where r_0 is called the Fried parameter. It has the value

$$r_0 = \left[0.423 \left(\frac{2\pi}{\lambda}\right)^2 (\cos\gamma)^{-1} \int C_N^2(z) \mathrm{d}z \right]^{-3/5}, \tag{2.6}$$

where γ is the angular distance of the light source from the zenith (given in radians). The Fried parameter r_0 is chosen such that it is a more intuitive measure for atmospheric distortions compared to C_N^2. For instance, the root mean square (rms) phase distortion calculated over a circular area having a diameter r_0 is 1 radian (Noll, 1976; Fried, 1965; Roddier, 1999a).

The power spectrum of a wavefront following the law in equation (2.5) is correspondingly called the Kolmogorov spectrum. Power spectrum in this context is defined as an average energy of the wavefront per spatial frequency,

$$\tilde{\phi}(\mathbf{f}) = \left\langle |\mathscr{F}\{\phi(\mathbf{x})\}|^2 \right\rangle, \tag{2.7}$$

where $\mathscr{F}\{\cdot\}$ denotes a Fourier transform and $\langle\cdot\rangle$ is a temporal average. The Kolmogorov spectrum can be written as (Noll, 1976)

$$\tilde{\phi}(\mathbf{f}) = \left(0.023/r_0^{5/3}\right) |\mathbf{f}|^{-11/3}. \tag{2.8}$$

As the Kolmogorov spectrum is not realistic at low frequencies (it approaches infinity), also more realistic models have been developed. In this thesis we use a von Karman spectrum that is found to be a better approximation. It has two additional parameters (*inner and outer scale*) to adjust the model to better describe the reality at high and low spatial frequencies.

Using a realistic inner scale in numerical simulations would require very high resolution phase matrices since structures of the order of centimetres should be modelled accurately. That would be unnecessary since the interesting scales in astronomical AO applications are at least an order of magnitude larger. Thus, the inner scale can be neglected and the von Karman spectrum used in this thesis be defined as

$$\tilde{\phi}(\mathbf{f}) = \left(0.023/r_0^{5/3}\right) \left(|\mathbf{f}|^2 + L_0^{-2}\right)^{-11/6}, \tag{2.9}$$

where L_0 is the outer scale of the turbulence. When L_0 approaches infinity, this expression approaches the Kolmogorov spectrum.

To estimate how big spatial deformations a DM needs to make for the required AO correction to be achieved, equation (2.5) can be used. However, to deduce the required system frame rate, one needs to make more assumptions.

For instance, the rate of the temporal evolution of the atmosphere has to be modeled. Practice has shown that the atmosphere can be approximated as a set of separate turbulent layers. These layers are moved by wind much faster than their shape is changed (like clouds). This is called the Taylor approximation (Roddier, 1999a).

It has been shown (Fried, 1990; Roddier, 1999a) that to keep the mean square phase error less than 1 radian, the total delay of the AO correction loop must be under

$$\tau_0 = 0.314\frac{r_0}{\bar{v}}, \tag{2.10}$$

where $\bar{v}$ is a weighted average of the wind speeds of the turbulent atmospheric layers. This delay is also called the Greenwood time.

2.2.2 Image formation

The atmospheric model discussed above tells how big the phase variations faced by an AO system are. However, to estimate more directly the quality of the image drawn from that phase, more theory is needed.

Using the Fraunhofer diffraction theory, the image of a point-like object can be computed at infinite distance — or equivalently at the focal plane of a lens having a focal length z. The theory says that the electromagnetic field (represented by a complex number having a phase and an amplitude) at the plane where the image is created (*image plane*) is a Fourier transform of the field at the system aperture (*pupil plane*),

$$\hat{\Psi}_0(u,v) = \iint_{\text{aperture}} \Psi_0(x,y) \exp\left[-2\pi i\,(ux+vy)\right] \mathrm{d}x\mathrm{d}y, \tag{2.11}$$

where $\Psi_0(x,y)$ is a complex function representing the electromagnetic field at the pupil plane and $(u,\, v)$ are connected to the position at the image plane (X,Y) by relations

$$u = \frac{X}{\lambda z}, \quad v = \frac{Y}{\lambda z}, \tag{2.12}$$

where λ is the wavelength of the light and z is the distance of the image plane from the aperture (the focal length of the lens). Since the field at the image plance is formed by a Fourier transform, the coordinates $(u,\, v)$ are called *spatial frequencies*. Intensity at the image plane is the square of the absolute value of $\hat{\Psi}_0(u,v)$. It is also called the *point spread function* (PSF) as it describes how light from a single point is imaged.

If the imaged object is too large to be considered as a point, it is called an *extended source*. Its image is a convolution of the PSF and the imaged source. In Fourier space the image can then be represented as a product of the source FT and the FT of PSF called also the *optical transfer function*. It can be written as

$$G(\mathbf{f}) = T(\mathbf{f})A(\mathbf{f}), \tag{2.13}$$

where $T(\mathbf{f})$ is the Fourier transform of a PSF from undistorted phase (called *telescope transfer function*) and $A(\mathbf{f})$ describes the atmospheric distortions (called *atmospheric transfer function*).

If it is assumed that the atmospheric perturbations obey Gaussian statistics, defined as

$$\left\langle e^{\phi(\boldsymbol{\xi})-\phi(\boldsymbol{\xi}+\boldsymbol{\rho})} \right\rangle \approx e^{-\frac{1}{2}\left\langle |\phi(\boldsymbol{\xi})-\phi(\boldsymbol{\xi}+\boldsymbol{\rho})|^2 \right\rangle}, \tag{2.14}$$

it can be written with the help of equation (2.5) that

$$A(\mathbf{f}) = \exp\left[-3.44(\lambda|\mathbf{f}|/r_0)^{5/3}\right] \tag{2.15}$$

in the uncompensated case. When AO is used, the transfer function becomes

$$A(\mathbf{f}) = \exp\left[-\frac{1}{2}D_\phi(\lambda\mathbf{f})\right], \tag{2.16}$$

where $D_\phi(\lambda\mathbf{f})$ describes the partial AO correction made by AO. Typically, an AO system compensates efficiently only low frequencies and therefore $D_\phi(\lambda\mathbf{f})$ behaves near zero similarly to the pure atmospheric transfer function shown in equation (2.5)

and approaches zero. At infinity, however, instead of growing endlessly, it saturates to a specific value. This gives (Roddier, 1999a)

$$A(\infty) = \exp(-\sigma^2), \tag{2.17}$$

where σ^2 is the variance of remaining uncorrelated small scale wavefront distortions. The better the compensation, the smaller is σ^2.

A traditional measure for image quality in optics is the Strehl ratio (R). It is the ratio between intensity maxima of a distorted and undistorted image of a point source. When AO compensation is made well and the telescope diameter is much bigger than r_0, it holds relatively well that

$$R = \frac{I(0,0)}{I_0(0,0)} = \frac{\int G(\mathbf{f})\mathrm{d}\mathbf{f}}{\int T(\mathbf{f})\mathrm{d}\mathbf{f}} \approx \exp\left(-\sigma^2\right).$$

On the other hand, if no phase distortions are present, a perfect image with a unity Strehl ratio is obtained. It is completely characterized by the *Airy pattern* (Hecht, 1998),

$$I_0(r) = \frac{1}{\left(1-p_{\mathrm{obs}}^2\right)^2}\left[\frac{2J_1(r)}{r} - \frac{2p_{\mathrm{obs}}J_1(p_{\mathrm{obs}}r)}{r}\right]^2, \tag{2.18}$$

where p_{obs} is the obstruction ratio ($0 \leq p_{\mathrm{obs}} < 1$), $J_1(\cdot)$ is the first order Bessel function and

$$r = \frac{\pi D}{\lambda}\theta, \tag{2.19}$$

where θ is the angular distance at the image plane from the optical axis and D is the telescope diameter. The function in equation (2.18) forms in the field center a clear spot (called *Airy disk*) surrounded by *Airy rings*.

If the AO system corrects the aberrations sufficiently, it is said that the resolution is *diffraction limited*. In such case the spot width of a point source is very close to the width of the Airy disk. Typically, to reach the diffraction limit, a Strehl ratio bigger than 0.20 is required.

The exact definition of the spot width is most often chosen to be the *Full Width at Half Maximum* (FWHM). It is the diameter of the area having an intensity higher than half of the spot maximum intensity.

The width of the Airy disk can be shown to be approximately, for an unobstructed aperture,

$$\mathrm{FWHM}_0 = \frac{\lambda}{D}, \tag{2.20}$$

which means that the ultimate diffraction limited image resolution depends only on the telescope diameter and imaging wavelength. If the imaging is done without AO correction (seeing limited case), the corresponding image resolution is approximately

$$\mathrm{FWHM}_s = \frac{\lambda}{r_0}, \tag{2.21}$$

which means that image resolution is inversely proportional to the Fried parameter r_0.

Astronomical seeing, characterized by the spot size of a point source, can be also statistically described by using the value of r_0. At the sites of the most important optical telescopes the seeing (at 0.5 μm) varies typically between about 5 and 20 cm, corresponding the spot sizes (at the same wavelength) about 2" and 0.5".

2.3 Deformable mirrors

A deformable mirror is the component in an AO system creating an optical path difference to compensate wavefront distortions at the system aperture. In theory, it would be possible to create a suitable OPD without a DM by modifying the refractive index of a transparent substance. Those devices however, although having been developed, have not gained popularity in astronomical applications because of chromacity issues and limited dynamical range.

Besides of the DMs, in practice also additional compensation devices are used in many AO systems to help with some DM limitations. Most important is the so-called *tip-tilt mirror*. It is a simple steering mirror capable of correcting (at least slowly evolving) tip-tilt part of the wavefront aberrations (see Section 3.1 for the definition of tip and tilt). It is used before the actual DM to lower the maximum phase difference (*stroke*) the DM is required to correct. This is useful because the wavefront having Kolmogorov statistics has significant tip and tilt components.

DMs can be classified by the type of the mirror surface and the function of the actuators.

One of the most popular solutions is to build the mirror from flexible material and reshape it with separate actuators. Another possibility is a *bimorph mirror*. Such mirrors consist of two piezoelectric wafers having an array of electrodes connected between the wafers. When a voltage is applied to the electrode, the wafer contracts locally and causes a deformation to the mirror.

The most popular way to construct an actuator is to use ferroelectric materials. Typically, several disks consisting of suitable material are piled on each other to build the so-called *stacked disk* actuator. Also monolithic actuators (only one disk) would be possible, but they do not produce a sufficient stroke. When a voltage (typically $0 - 500$ V) is applied on an actuator, the piezoelectric effect causes the actuator to enlarge. Typically, available strokes are of the order 50 μm. DMs consisting of stacked arrays are the most popular design option at the moment.

Also non-ferroelectric actuators have been developed. One possible design works with so-called *membrane mirror*. It means that the mirror is a membrane inside a partial vacuum. Reflected light comes through a transparent electrode (being set to a constant voltage) and actuators are moved by applying them a small voltage difference. Membrane mirrors have no hysteresis or inertia, but they experience drawbacks in having ghost reflections and a limited spectral range (Séchaud, 1999).

As discussed later, the DMs are often used to approximate shapes of specific modes. This, unfortunately, is never fully possible. If N actuators are used and each pushed by amplitude a_i, a continuous face sheet mirror takes approximately a shape as

$$D_m(x, y) = \sum_{i=1}^{N} a_i f_i(x, y), \tag{2.22}$$

where $f_i(x, y)$ is called the *influence function* of the ith actuator.

Since the actuators are connected through the mirror, moving one actuator drags usually behind its neighbors. This means that the actuators are *coupled* and in such case an influence function $f_i(x, y)$ covers also positions of other actuators. Typically, moving an actuator drags its neighbors about 15% of the original position change.

In addition, the DMs — especially the stacked actuator DMs — have a significant dynamical limitations. Typically, the phase lag is less than 5% at 1 kHz (depending on the frame rate) and the actuator hysteresis with a stacked array is less than 5% from the full stroke (Séchaud, 1999). This is discussed later in Section 3.3.1 in the context of AO system overall dynamics.

It can also be pointed out that in many cases it is sufficient to approximate the capabilities of a DM by its actuator spacing. If the actuators are in a grid having a constant interval, d, the mirror is then able to compensate (according to the Nyquist sampling) the spatial frequencies lower than $1/(2d)$. As the incoming wavefront obeying the Kolmogorov spectrum typically has most of its energy at low spatial frequencies, having a dense actuator grid is not necessary when only the low order modes need to be corrected by AO.

2.4 Wavefront sensors

The task of a wavefront sensor is to measure the shape of the incoming wavefront at the sampling the DM is able to correct. Several types of WFSs have been proposed and studied, but none of them has been yet shown to be always superior compared to the others.

A first technique, one could consider obvious, is to derive the wavefront from the intensity image directly detected at the focal plane. Such wavefront sensing has been studied by several authors (Fienup, 1982; Kendrick et al., 1994; Rousset, 1999) and the concept is called *focal plane technique*. Theoretically, such an approach, applied with phase diversity techniques, would give excellent sensitivity and other interesting properties (Guyon, 2005).

In practice, however, the focal plane techniques have proved — at least so far — to be impractical for AO purposes. For instance, the inversion from the intensity images to wavefront is not unique and also computationally very demanding.

Thus, all major WFSs currently use indirect methods to observe the wavefront. Either a gradient, Laplacian or a similar measure is detected and the wavefront is constructed from those measurements.

As mentioned, perhaps the most popular wavefront sensor currently in the AO applications is the Shack-Hartmann sensor. The SH-WFS is directly derived from its predecessors in optical testing and is discussed in more detail in Section 2.4.1. Also the pyramid sensor is discussed later at length in Section 2.4.2.

SH-WFS and P-WFS produce a measurement approximating the phase gradient. A sensor measuring the Laplacian of the phase is called curvature WFS (C-WFS). It operates by recording two defocused images of the beam (Rousset, 1999) and has been successfully applied in astronomical AO applications, for instance in SINFONI (Eisenhauer et al., 2003). However, the sensor has some unfortunate properties that make it less attracting for the future AO applications. For instance, the measure-

ment of a second derivative is prone to noise; especially at low spatial frequencies C-WFS has even worse sensitivity than SH-WFS (Guyon, 2005). Thus, C-WFS is out of the scope of this thesis.

2.4.1 Shack-Hartmann sensor

The operation of the sensor is illustrated in figure 2.6. The incoming wavefront is imaged using an array of lenslets. Each subaperture creates its own small image at the focal plane. If no phase aberrations are present, the image pattern is a grid of spots having constant intervals.

If the phase at one subaperture has a local tip-tilt aberration, the spot at the image plane experiences a shift of (dx, dy). The shift is directly proportional to the average derivative of the local phase.

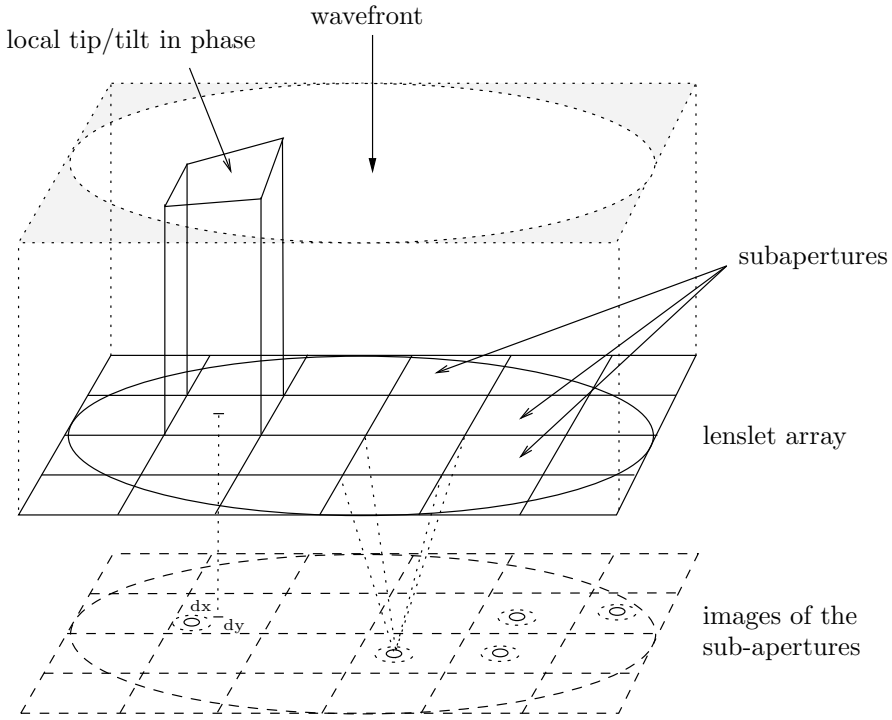

Figure 2.6: Sketch of a Shack-Hartman wavefront sensor.

Thus, the SH-WFS measures the local slopes in the wavefront and can be therefore classified as a slope-sensor.

The properties of the sensor are well known and it is easy to manufacture. When properly manufactured and calibrated, the SH-WFS is linear over a large dynamic range. The sensor requires, however, several parameters to be carefully optimized by the manufacturer: number of subapertures, CCD pixel resolution at each subaperture, subaperture field-of-view and so on.

For instance, the easiest and less noise-sensitive option would be using 4 pixels at subaperture (quad-cells). This approach, however, reduces the sensor linearity and thus the most common solution is to use 6–8 CCD pixels. The latter approach

also enables using an advanced weighted center of gravity (WCOG) algorithm, to compensate the noise (Nicolle et al., 2004; Thomas et al., 2006; Fusco et al., 2006).

Issues

The SH-WFS has a few well known problems. One is its susceptibility to aliasing. It means that some of the high spatial frequency components in the wavefront are incorrectly seen as lower frequencies. When taking samples from a continuous signal with an interval T, aliasing will happen if the signal is not band limited at the Nyquist frequency $1/(2T)$ (Hayes, 1996).

The aliasing can, to some extent, be avoided by using a *spatial filter* (Poyneer and Macintosh, 2004). It is an optical device built before the lenslet array to filter out the non-seen high spatial frequencies from the residual wavefront. At first, the light is focused into an image plane, where the filter is installed. Only the central part in the image plane is transparent (only the lower spatial frequencies pass). After passing the filter, the wavefront is relayed again to a pupil plane and fed to the SH-WFS lenslet array.

Unfortunately, the exact size of the spatial filter cannot be easily determined. It has been found that a filter size close to the theoretical limit λ/d removing all the non-seen frequencies severely degrades the AO closed-loop stability (Korkiakoski et al., 2004). In bad seeing conditions the filter size must be increased to achieve the loop stability at the expense of increased aliasing. For instance, a filter size 1.5 λ/d has been found to be optimum in an XAO regime closed-loop experiment (Fusco et al., 2005).

In addition, the SH-WFS is less sensitive to detect certain wavefront variations, when compared to, for instance, the P-WFS. This is discussed in more detail in Section 2.4.3.

2.4.2 Pyramid sensor

The pyramid sensor was initially proposed by (Ragazzoni, 1996) and can thus be considered as a relatively new concept. It was presented for AO purposes as a more convenient sensor — the sensor is more flexible for guide star brightness (sampling is not restricted by subapertures) and the seeing conditions (its sensitivity can be modified).

P-WFS was then analyzed by several analytic (Vérinaud, 2004) and numerical (Esposito et al., 2000b; Esposito and Riccardi, 2001; Vérinaud et al., 2005; Clare and Lane, 2004) studies. It was shown that the sensor is potentially superior to SH-WFS due to its better sensitivity and could be suited especially for XAO purposes.

These analytic and numerical results have been verified in laboratory experiments (Esposito et al., 2000a,b; Burvall et al., 2006). Also a layer-oriented P-WFS for multi-conjugate AO (implemented for MAD) has been successfully tested in laboratory (Vernet-Viard et al., 2005; Arcidiacono et al., 2006). Currently two pyramid sensors have been operated on-sky: the P-WFS for AdOpt@TNG at Telescopio Nazionale Galileo (Ghedina et al., 2003) and PYRAMIR at Calar Alto 3.5 m telescope (Feldt et al., 2006).

However, all the practical experiments so far have been done using low-resolution systems giving only partial information as to how the WFSs with XAO would work. Laboratory tests for the XAO regime are planned to be carried out in the near future, for instance at the High Order Testbench (HOT) at ESO (Vernet et al., 2006).

The principle of the P-WFS is illustrated in figure 2.7. The incoming wavefront is reflected through a steering mirror and focused on a pyramid prism. The prism divides the beam into four sub-beams. Finally, an optical relay projects four pupil images on a detector. The sensor signal is then composed from those CCD measurements.

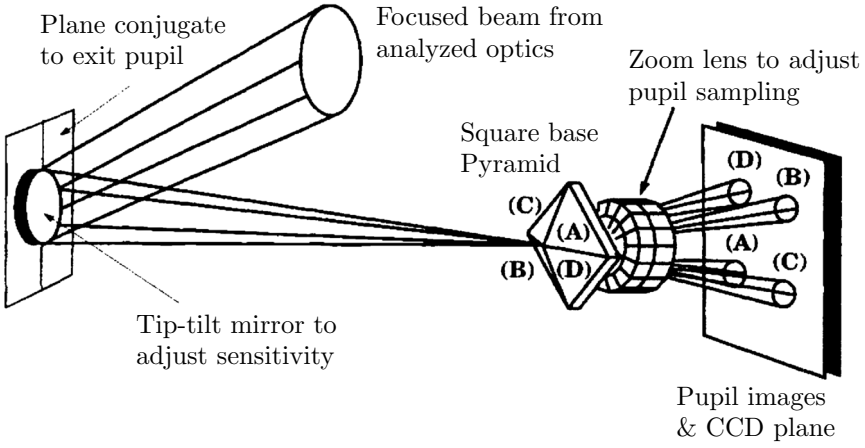

Figure 2.7: Illustration of a pyramid wavefront sensor (Esposito et al., 2000b).

The signal composition is done by combining the intensities as,

$$S_x(x,y) = \left[I_A(x,y) - I_C(x,y) + I_D(x,y) - I_B(x,y)\right]/I_t,$$
$$S_y(x,y) = \left[I_A(x,y) - I_D(x,y) + I_C(x,y) - I_B(x,y)\right]/I_t,$$

where the intensity patterns are illustrated in figure 2.7, (x,y) describes the location at each sub-image and I_t is a normalization constant explained later in Section 5.1. In practice, the signal is discretized such that (x,y) shows the pupil location corresponding to the four CCD pixels in the detector. The signal values $S_x(x,y)$ and $S_y(x,y)$ are then usually organized into a single measurement vector.

It has been shown, using geometrical reasoning, that the signal, $[S_x(\mathbf{r})\ S_y(\mathbf{r})]^T$, is approximately proportional to the phase gradient, if the phase distortions are small (Riccardi et al., 1998; Feeney, 2001).

The exact relation between the signal and the phase slopes, as well as the validity of the approximation, is modified by the steering mirror. The steering tip-tilt mirror causes a shift in the focal plane and its aim is to circulate the beam focus around the pyramid tip. One circulation is done during the WFS integration time to average the prism diffraction effects. This is called *modulation*. The original proposal in (Ragazzoni, 1996) was to rotate the prism itself to achieve modulation. However, tip-tilt mirrors were found to be more practical.

Modulation is done to increase the dynamical range of the sensor. It is known that without the modulation the P-WFS saturates at high wavefront distortions.

However, building the modulation is technically demanding and therefore it has been discussed in several works whether it is actually necessary. For instance, (Ragazzoni et al., 2002) has proposed that a diffusing plate placed in an intermediate pupil plane would remove the need for the dynamic modulation.

The necessarity of the modulation is also discussed in length by (Costa, 2005; Costa et al., 2004, 2003), but no complete answer has been obtained. In this thesis we concentrate mostly on the nonmodulated P-WFS.

Modifications

In addition of the ordinary four-sided pyramid prism, also a "roof-pyramid" (or a two-sided pyramid) has been proposed in (Phillion and Baker, 2006). At first, the beam (the incoming wavefront) is divided into two by a beam splitter. Then each sub-beam is directed to a roof-prism splitting the beam again. As a result, four sub-beams are obtained — they correspond to the beams of the conventional P-WFS, except that their interference effects are fundamentally less significant. Also more variations of the pyramid sensors have been considered, for instance having a varying number of sides (Clare and Lane, 2003).

The measurement signals of the traditional and four-sided P-WFS are illustrated in figure 2.8. A local piston is introduced to an area corresponding to a single "subaperture" (in a system having a measurement resolution of 40×40). At each sub-pupil this area covers a single CCD pixel. The measurement for this phase is then simulated using an analytic wave-optics model neglecting the sub-beam interferences. Both the model of a classical four-sided and the novel two-sided P-WFS are used.

It is seen that the signal of the classical P-WFS is changed throughout the pupil, although the major changes are along the x- or y-axis. The two-sided P-WFS, on the other hand, has the signal variations only along the corresponding axes. It can be also pointed out that a SH-WFS would not be able to detect this phase at all since it consists only of a local piston at a subaperture.

The performance of this two-sided pyramid sensor is shown in preliminary simulations to be better compared to the traditional P-WFS or SH-WFS (Phillion and Baker, 2006). This effect is studied also in this thesis (see Chapter 5) and similar results are obtained. However, the concept requires additional optics and is not yet implemented for any closed-loop AO application.

It is also suggested that the whole pyramid prism of glass could be replaced by a micro-optic lenslet array (Johnson et al., 2006). This approach, however, is very new and its feasibility is not yet properly evaluated.

2.4.3 Pyramid compared with Shack-Hartmann

P-WFS and SH-WFS have been compared by several authors. Next the most important results are briefly described.

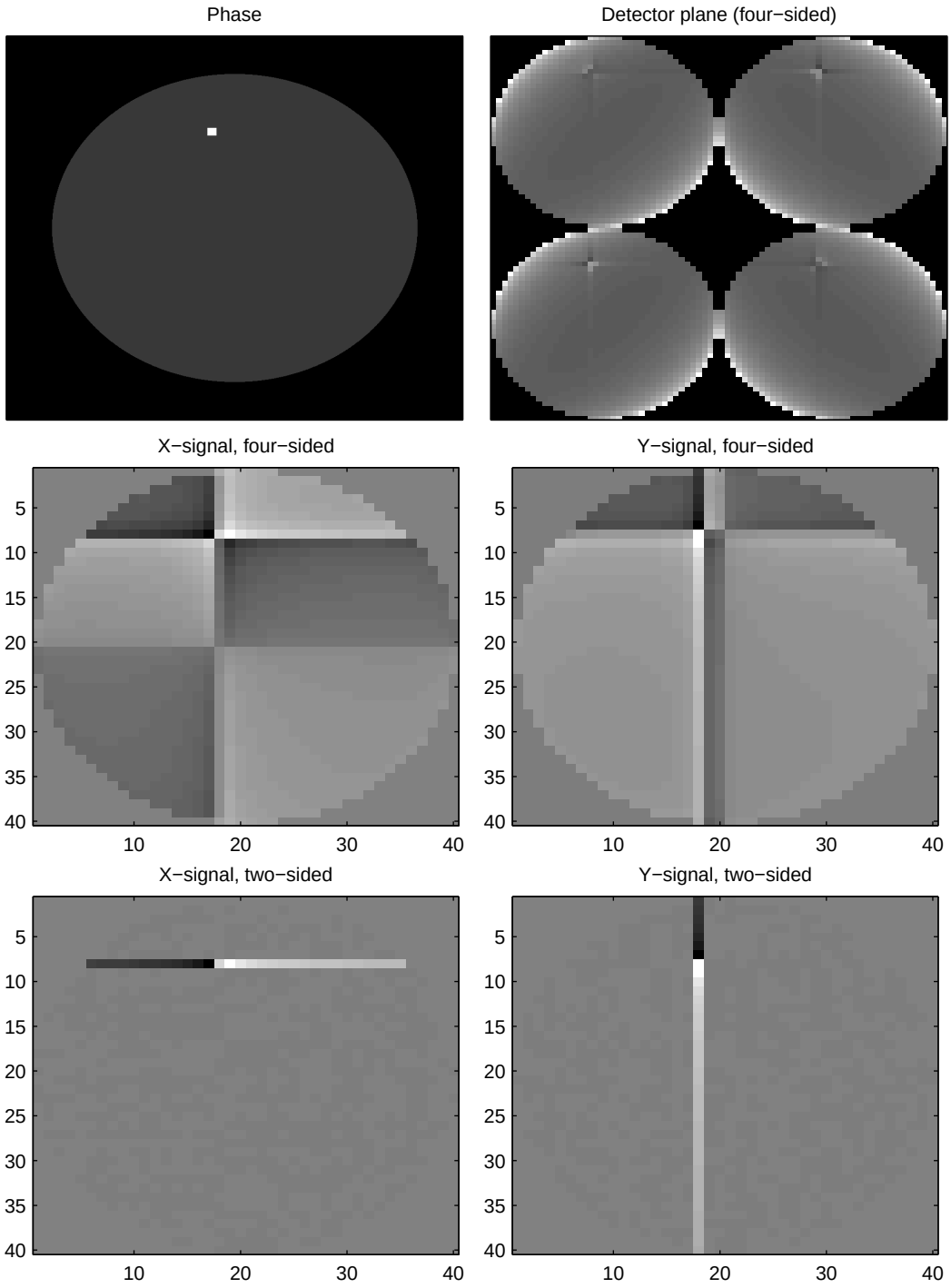

Figure 2.8: Illustration of P-WFS signal differences between a classical four-sided and two-sided P-WFS. Measurement resolution is 40×40. Each image is shown using an independent nonlinear scaling. Upper row: the measured phase and the intensities at the detector plane (for the four-sided P-WFS). Middle row: signals of the conventional four-sided P-WFS. Lower row: signals of the two-sided P-WFS.

Photon noise

Accurate measurement of the incoming wavefront is the most critical part of an AO system. The fainter the reference stars the WFS can use, the wider the observation range of possible scientific sources.

The measurement noise of WFSs consists of two major effects. *Photon noise* is due to the quantum effects of the limited number of photons detected by the sensor. *Read-out noise* is caused by the electronics when reading the measurement.

Photons arrive at the detector according to the Poisson statistics and although only one is enough to cause a detectable response, a good measurement requires many of them. In a case of high photon flux, the read-out-noise is often negligible since stronger currents are involved. In addition, the measuring electronics are often the same in P-WFS and SH-WFS and the new generation of detectors have very low noise (L3CCD for instance have less than 1 electron read-out noise per frame). Therefore, analyzing only the effect of the observed photon number is mostly enough when comparing the different sensors.

Thus, estimating how the photon noise affects the sensor measurements has been the first approach of evaluating the WFS feasibility. This can be done simply by considering how the WFS reacts to random noise.

In the literature the noise of the SH-WFS is usually represented as a variance of the wavefront and the units are converted to radians square. For a SH-WFS being dominated by the photon noise, the noise variance can be written as (Rousset, 1999)

$$\sigma_s^2 = \frac{\pi^2}{2}\frac{1}{n_{\mathrm{ph}}}\left(\frac{\theta_b d}{\lambda}\right)^2 \ (\mathrm{rad}^2), \tag{2.23}$$

where n_{ph} is the number of photons per subaperture and exposure time, θ_b is the angular size of the source image (the measurement spot size) and d is subaperture diameter.

A similar evaluation for the P-WFS is more complicated, since the measurements are dependent on the whole wavefront instead of local subapertures. However, the error on the P-WFS measurements due to the photon noise has also been shown to be proportional to the inverse of the photon number, $\sigma_s^2 \propto 1/n_{\mathrm{ph}}$ (Feeney, 2001; Vérinaud, 2004).

Since both SH-WFS and P-WFS measurements have a similar $1/n_{\mathrm{ph}}$ dependency on the photon noise, the sensors must be compared based on their signal-to-noise ratio. This is characterized by the sensitivity that defined and discussed in the next subsection.

If the WFS is limited by read-out noise, equation (2.23) needs to be modified. In addition, the sky background photon noise affects the measurements. These issues, however, are outside the scope of this thesis.

Sensitivity

The other approach to compare the WFSs takes into account also how the sensor is able to measure specific wavefronts. This is referred to the sensor sensitivity.

The sensitivity is defined in this thesis (as well as often in AO literature) as the ratio between the standard deviations of the measurement and wavefront. Typically

it is computed for a specific spatial frequency of the measured phase or an applied mirror mode. Having a small sensitivity can be problematic since it means that the measurement noise becomes more significant. (Alternative definition in (Guyon, 2005) declares sensitivity directly as the sensor's susceptibility to noise.)

When considering the fundamental properties of the WFSs, the sensitivity can be formalized analytically in Fourier space. It is shown in (Vérinaud, 2004) that the sensitivity of SH-WFS is directly proportional to the spatial frequency. With P-WFS, the sensitivity is affected by the amount of modulation. Below the ratio of modulation angle (α) and sensing wavelength (λ), the sensitivity is proportional to λ/α and after it stays at a constant value (see the left plot in figure 2.9).

Similar results obtained using a different formalism are shown in (Guyon, 2005; Guyon et al., 2006) and also the approach used in (Chew et al., 2006) confirms the advantage of the P-WFS. This is especially important for XAO applications. It means that at low spatial frequencies the halo is damped more effectively using P-WFS.

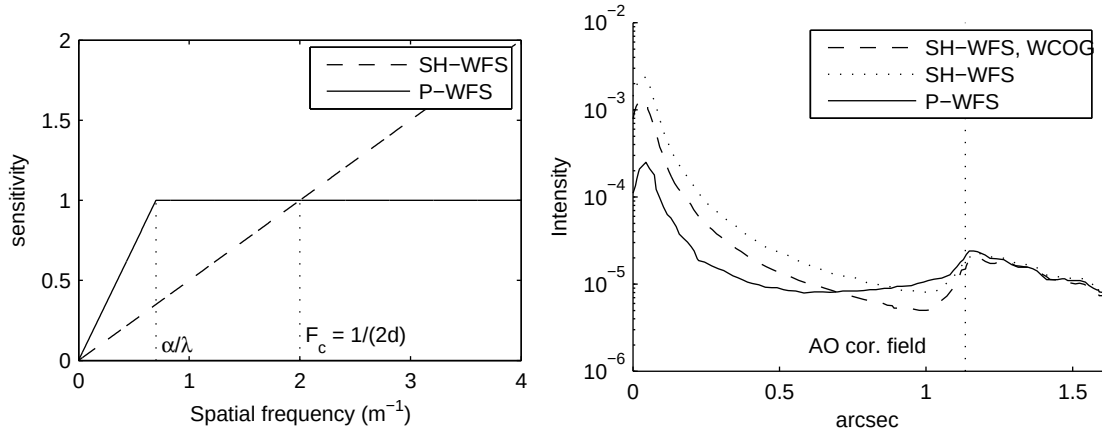

Figure 2.9: Left: Fourier SNR curves for SH-WFS and P-WFS. Subaperture size $d = 0.25$ m. Sensing wavelength per modulation angle, $\lambda_{\text{img}}/\alpha = 1.4$ (Vérinaud, 2004). Right: circularly averaged residual halo from AO simulations (seeing 0.85", 20 photons per subaperture, Strehl ratio at 2.2 μm about 0.95). (Vérinaud et al., 2005).

The analytic approaches mentioned before, however, do not consider the closed-loop characteristics of the AO loop. Thus, it must be verified through numerical simulations that the temporal error caused by the time lag or other, non-modeled, WFS effects are not too extensive.

Such simulations have indeed been made, and they verify the expected gain of the P-WFS over SH-WF (Vérinaud et al., 2005, 2004). An example is shown on the right in figure 2.9. It shows the halos of a dim (magnitude 12) star, resulting from a simulation with a P-WFS and two SH-WFS simulations (with and without WCOG). The SH-WFS was optimized by using the spatial filter. It is seen that the P-WFS gives a halo more than two times smaller at the lower spatial frequencies. This helps to detect the objects near the star.

Thus, the P-WFS has been chosen as the baseline of the proposed instrument (Exo-Planets Imaging Camera and Spectrograph, EPICS) to image exoplanets with the forthcoming ELTs (Vérinaud et al., 2006).

However, especially when using the P-WFS without modulation, problems arise due to the limited dynamical range of the sensor.

It has been proposed that during the bootstrap phase various methods can be used to reach the steady state easier and faster (e.g., using a smaller resolution (Ragazzoni and Farinato, 1999) or a nonlinear control (Wulff and Looze, 2006)). These suggestions assume that after the loop is closed, the better sensitivity of the P-WFS will help to keep the system at the regime where it outperforms the SH-WFS.

Nevertheless, it will be shown in this thesis in Chapter 5 that without new control methods the AO loop with P-WFS cannot successfully be operated in conditions having high residual wavefront distortions.

2.5 Adaptive optics simulations

Most of the work in this thesis is based on the parallel simulation software developed at ESO. The tool, named as OCTOPUS (Optimized Cluster Tool for adaptive Optics Parallel Unlimited Simulations) is described in more detail in this section. At first, however, we give a short summary of the most important AO simulation tools.

2.5.1 Overview

During the last decade, several tools have been developed to simulate adaptive optics. They can be categorized roughly into two types: numerical Monte Carlo simulators and analytic codes. The former can take into account second-order effects like misalignments, actuator hysteresis and dynamics. However, exploring several AO parameters fast becomes impossible due to the extensive computational demands.

The analytic AO simulation codes have been designed to give rough PSF estimates very fast for a wide range of parameters. They are based on the known formulas of atmospheric statistics and often neglect several second-order effects that are difficult to incorporate into analytic models. The differences of the simulation schemes are discussed further for instance in (Le Louarn et al., 2005b).

The most important AO simulation tools are listed in Table 2.2. The table also shows the coding language(s) and the existence of GUIs. Due to these differences in the design, the tools are suited for complementary purposes. For instance, the scripting languages like Matlab or IDL are easy to write, but their computational capacity can be worse compared to the codes using the native platform of the computers.

Unlike any of the other codes, OCTOPUS has been designed exclusively for the Monte Carlo simulation of large AO systems. In the beginning its major aim was to simulate the 100 meter OWL (Overwhelmingly Large Telescope), (Le Louarn et al., 2004b), but after its re-design the tool has been used for the 42 meter E-ELT, (Le Louarn et al., 2006).

In its current computer cluster, OCTOPUS can be used for MCAO simulations with over 100×100 SH-WFS subapertures and multiple turbulent phase screens

Table 2.2: A list of most important AO simulation tools

Tool	Author	Type	Implementation	GUI
CIBOLA	B. Ellerbroek	Analytic	Matlab	In Linux
PAOLA	L. Jolissaint	Analytic	IDL	No
yao	F. Rigaut	Numeric	yorick & C	Yes
CAOS	M. Carbillet et al.	Numeric	IDL	Yes
Arroyo	M. Britton	Numeric	C++	No
OCTOPUS	M. Le Louarn et al.	Numeric	C, C++, MPI	No

having a size over 8192×8192 pixels.

The actual implementation of OCTOPUS has been described in more detail in (Le Louarn et al., 2004a) and some of its technical properties are further illustrated in (Korkiakoski, 2004). (Note that the tool was named OCTOPUS later.) In the following the most important features are pointed out.

2.5.2 OCTOPUS properties

Coding philosophy

The major parts of OCTOPUS have been coded using parallelized C. The parallelization is done using an open source implementation of the MPI (Message Passing Interface), (Pacheco, 1997). In addition, several freely available libraries are used, for instance FFTW, (Frigo and Johnson, 2005) for the fast Fourier transform (FFT) operations and ScaLAPACK, (Choi et al., 1996) for parallel matrix operations.

OCTOPUS has been developed on ESO's AO simulation farm — and currently all major simulations are run on it. The farm is a cluster consisting of tens of desktop PCs. The size of the cluster has been annually updated, with currently 76 PCs. The properties of the cluster are shown in Table 2.3.

However, OCTOPUS is not restricted to this cluster. The advantage of the chosen programming philosophy is the flexibility and computing power of C. At the moment virtually all platforms support C, and its characteristics as a low level language enable aggressive compiler optimizations. Thus, the design of OCTOPUS makes it possible, in principle, to run it in the future on a typical supercomputer.

The inevitable disadvantage of OCTOPUS is its complexity. Coding with MPI requires all the communication operations being explicitly written. Thus, even simple matrix multiplications or FFTs require a significant amount of coding (typically at least tens of lines).

As a partial solution to circumvent the complexity problem, a Matlab interface has been created for OCTOPUS in 2006. By using the OMI (OCTOPUS Matlab Interface), a part of the C-code can be bypassed and implemented with easier Matlab code. This property has been used several times in this thesis to test experimental reconstruction and control techniques. Also other works, for instance (Correia et al., 2006; Muradore et al., 2006), have used the interface. Nevertheless, OMI effectively restricts the computational capacity of OCTOPUS.

Next the most important fields of AO simulations with OCTOPUS are briefly

Table 2.3: The properties of ESO AO simulation farm in 2007

Master	
Processors	2 × Pentium Xeon CPU 3.2 GHz
Cache	2048 KB
Memory	3 GB of RAM
Mass storage	1 × 450 GB disk, DLT drive
	2 × 230 GB disk, DLT drive
	2 × 1 TB disk, USB drive
Slaves (76 machines)	
Processor	46 × DELL GX280, Pentium 4 CPU 3.2 GHz
	30 × DELL GX620, Pentium D CPU 3.2 GHz
Cache	1024 KB
Memory	2 GB of RAM
Mass storage	60 GB
Networking	
Switch	Cisco 4506, 48 Gigabit Ethernet ports
Master	Gigabit Ethernet card (access to cluster)
	100 MB Ethernet card (access to outside world)
Slaves	on-board Gigabit Ethernet
System	
Linux FC3	
No cluster management software	

discussed.

Turbulence model and wavefront propagation

OCTOPUS has a layer model of the atmosphere similar to all other Monte Carlo AO simulators. Each layer is a random realization of the von Karman power spectrum. We call these layers phase screens.

As all the AO simulation tools listed in Table 2.2, OCTOPUS currently simulates only monochromatic cases.

At the moment two wavefront propagation methods are implemented: geometrical and Fresnel propagation. The first means a straightforward summing of the phase screens in the direction of the line of sight. The latter requires heavy computations according to a wave model. The model, called Fresnel diffraction in the literature, is a more accurate approximation of the electromagnetic wave propagation. Its numerical implementation is done using large FFTs (the whole phase screens should be used) for each simulated atmospheric layer. The wavefront propagation for AO simulations is discussed in more detail for instance by (Ellerbroek and Cochran, 2002).

Since the geometrical propagation is dramatically faster, it is usually preferred in AO simulations. The feasibility of this approach has been extensively discussed, for instance in the context of the SPHERE instrument (Fusco et al., 2006) that is a

first generation XAO system for an 8 m telescope. It has been found that the effects introduced by the Fresnel propagation (e.g., scintillation) are negligible compared to the residual phase effects.

Also this thesis uses only the geometrical propagation, which is justified, since most of the illustrated simulations are comparable to the SPHERE case.

OCTOPUS has two methods to simulate the temporal evolution of the turbulence. The first and faster method shifts the turbulent phase screens only an integer number of pixels. The exact cumulative transition is computed at each step and when it exceeds one or several pixels, the shifting operation is done. This, however, results in anomalies in the temporal power spectrum of the phase — at certain frequencies some unwanted peaks appear. In addition, in XAO regime having a very small residual error (Strehl ratio over 0.90 at 1.6 μm), the jerky phase screen movements are seen as an unnatural variation in the short exposure Strehl ratio.

An improved turbulence shifting was implemented in 2005. Instead of the pixel-wise shift of the phase screens, the shifting was implemented as modulation in the Fourier space. At first, the Fourier transform of each phase screen is computed. Then, for each time step, the Fourier transforms are modulated by the amount that corresponds to the exact shift needed to simulate the wind speeds. Finally, the correctly shifted phase screens are obtained by applying inverse Fourier transforms.

Besides enabling continuous movements of the phase screens at correct speeds, the method is also guaranteed to preserve the frequency content of the phase screens unmodified — unlike for instance the shifting methods based on interpolation.

The new FFT based method is computationally much heavier and is thus implemented by saving the propagated turbulence pieces (at the telescope aperture) in the disk before any AO simulation. If not otherwise mentioned, this turbulence model is used in all simulations in this thesis.

Deformable mirror

The current version of OCTOPUS simulates perfect linear deformable mirrors having no dynamics. Hysteresis or any actuator imperfections are not modeled in this work.

Only one type of sensor geometry is considered: the actuators are located in the corners of SH-WFS subapertures. The subaperture grid is evenly spaced and the subapertures are squares.

Computing the mirror shape is done by summing the actuator influence functions weighted by the actuator voltages.

Two types of influence functions are used: linear splines without cross-coupling or more realistic influence functions provided by Rigaut, as explained in (Le Louarn et al., 2005b), with about 15% cross-coupling. The linear splines are characterized by

$$f(x,y) = \left[1 - \left(\frac{x}{x_0}\right)\right]\left[1 - \left(\frac{y}{y_0}\right)\right] \tag{2.24}$$

and the Rigaut's influence functions by

$$f(x,y) = \left(1 - \left|\frac{x}{x_0}\right|^{3.805} + 3.74 \log\left(\left|\frac{x}{x_0}\right|\right)\left|\frac{x}{x_0}\right|^{2.451}\right) \times \left(1 - \left|\frac{y}{y_0}\right|^{3.805} + 3.74 \log\left(\left|\frac{y}{y_0}\right|\right)\left|\frac{y}{y_0}\right|^{2.451}\right), \quad (2.25)$$

where x_0 and y_0 define the function width (actuator spacing). The influence functions are illustrated in figure 2.10. The linear spline covers an area twice the subaperture diameter while Rigaut's function is slightly wider.

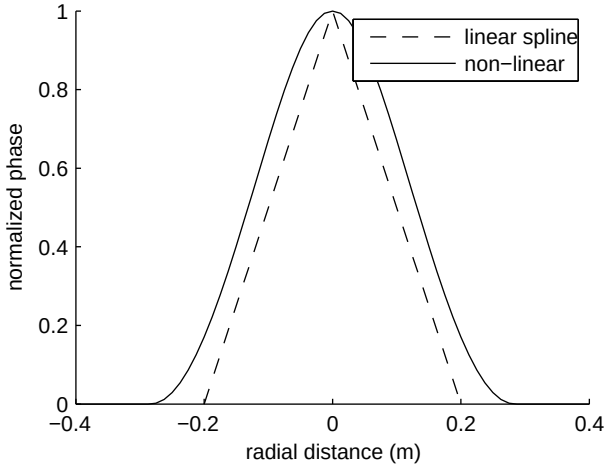

Figure 2.10: Radial cuts of two influence functions used in this thesis. These examples are from a system having an 8 meter telescope and 40×40 subaperture grid (0.20 m subaperture width). The actuators are at the corners of the subapertures.

As explained in (Le Louarn et al., 2005b), the linear spline influence functions have the advantage of producing perfect piston and tip-tilt. However, they contain sharp elements (high frequency components) that can possibly produce artifacts (spikes) in the simulated PSFs.

The more realistic Rigaut's influence functions have the advantage of representing fairly accurately the shape of a piezo-stack DM. However, when pushing all actuators, they produce a rippled surface unlike the real DM. This can also produce artifacts.

Nevertheless, in our simulations we have observed that the choice of the influence function between these two choices does not have a significant effect on the Strehl ratio.

Wavefront sensors

OCTOPUS has two wavefront sensors implemented: Shack-Hartmann and the pyramid WFS. As explained in (Le Louarn et al., 2004a), they both compute explicitly the intensity at the CCD detector using wave optics models applied to the residual

phase. The SH-WFS can be simulated easier since each subaperture can be considered separately. P-WFS, on the other hand, must use the whole phase information in the computation of each measurement element.

The P-WFS can be simulated using two algorithms (phase mask algorithm and amplitude mask algorithm) described later in Section 5.1.1. Both of them are implemented in OCTOPUS and the former is fully parallelized (a single measurement can be computed using several computers).

The modulation for P-WFS is simulated by discretizing the modulation steps in the same way as explained in (Esposito and Riccardi, 2001). A sufficient sampling is usually 8 points for a modulation of 1 λ/D, 16 for 2 λ/D and so on. Thus, simulations with large modulation angles — especially with big AO systems — take a lot of time. For instance, in the current cluster an end-to-end AO simulation (with about 1 s integration time at 1 kHz and a measurement resolution of 40×40) can take several days for modulation angles higher than 5 λ/D.

The situation can be improved in the future by optimizing the parallelization and adding more machines to the cluster.

Wavefront reconstruction

In OCTOPUS, the standard method of wavefront reconstruction is a matrix-vector multiplication (MVM) — the measurement vector is multiplied by a reconstruction matrix to obtain the actuator commands. Here other possibilities (like Fourier reconstruction (Poyneer and Véran, 2005) or fast reconstruction methods (Ellerbroek and Vogel, 2003)) are not considered.

The wavefront reconstruction in general is discussed in more detail in Section 3.2. OCTOPUS implements both the zonal and modal approaches. In addition, also both the truncated SVD (see Section 3.2.1) and the MAP method (see Section 3.2.2) are supported. However, unless otherwise mentioned, only the modal approach with truncated SVD is used in this work.

Chapter 3

Adaptive optics control

The previous chapter described the principles of adaptive optics in general and its most important concepts. This chapter is devoted purely to the wavefront reconstruction and dynamic control of AO in closed-loop operation.

The chapter is divided into three sections. Section 3.1 describes a few concepts commonly used in the context of AO compensation — the modal formulation and its advantages. Then, Section 3.2 discuses the issues involved in wavefront reconstruction and Section 3.3 describes the AO loop dynamic control.

3.1 Modal compensation

The general effects of the atmosphere, and how an image is formed, were discussed in Sections 2.2.1 and 2.2.2, respectively. This section briefly summarizes typical mathematics involved in AO compensation.

Generally, the higher is the required final image resolution, the more actuators are needed in the deformable mirror. In practice, to control a system having P actuators, at least as many measurements (M) are needed. The number of actuators determines the *degrees of freedom* of the system.

Typically, a DM having P degrees of freedom is considered to create a phase shape $\phi(\mathbf{x})$ of P *modes* $M_i(\mathbf{x})$,

$$\phi(\mathbf{x}) = \sum_{i=1}^{P} a_i M_i(\mathbf{x}), \tag{3.1}$$

where the coefficients a_i determine the amount of each mode in the shape. In the idealistic conditions the DM would thus compensate the first P modes present in the incoming wavefront, leaving the uncompensated phase to be

$$\hat{\phi}(\mathbf{x}) = \sum_{i=P+1}^{\infty} a_i M_i(\mathbf{x}). \tag{3.2}$$

Two modal bases are of significant importance in AO. The first basis uses the *Zernike* modes ($M^z(\mathbf{x})$). They have a fairly simple analytic expression and are orthogonal in the sense that $\int M_i^z(\mathbf{x}) M_j^z(\mathbf{x}) \mathrm{d}\mathbf{x} = \delta_{ij}$ (Noll, 1976).

The most important Zernikes are the first three modes. They are called *piston*, *tip* and *tilt*. These modes can be created using flat surfaces. Piston mode is a simple constant phase difference. Tip and tilt are linear surfaces in x- and y-direction respectively (they also contain the most energy in a typical wavefront distorted by the atmosphere). Further aberrations are defocus, astigmatism, coma, spherical and trefoil; they have nonlinear shapes. The names originate from the history of optics — the modes were used to describe some of the most common optical aberrations.

The Zernike modes are important since the atmospheric statistics derived from equation (2.5) can be nicely presented in terms of modal coefficients (Noll, 1976; Wang and Markey, 1978). The covariance between the coefficients a_i and a_k (i, k denoting modal indexes) is

$$\langle a_i, a_k \rangle = \left\langle \int M_i^z(\mathbf{x})\phi(\mathbf{x})\mathrm{d}\mathbf{x} \int M_k^z(\mathbf{x}')\phi(\mathbf{x}')\mathrm{d}\mathbf{x}' \right\rangle, \tag{3.3}$$

which reduces to (Noll, 1976)

$$\langle a_i, a_k \rangle = c_{ik} \left(D/r_0\right)^{5/3}, \tag{3.4}$$

where c_{ik} can be expressed analytically for the Zernike modes and D is telescope diameter.

It follows that the total variance of atmospheric phase having N first Zernike modes (except the piston) removed by an AO system is

$$\sigma_{N+2}^2 = \sum_{i=N+2}^{\infty} \left\langle a_i^2 \right\rangle = \sum_{j=N+2}^{\infty} c_{ii} \left(D/r_0\right)^{5/3}, \tag{3.5}$$

since the modes are orthogonal. The ratio of $\sigma_{N+2}^2/\sigma_1^2$ (compensated / uncompensated variance) decreases as a $N^{-0.87}$ for large N (Roddier, 1999b).

The second important mode base is so-called *Karhunen-Lóeve* (K-L) basis. It is characterized by being the only base giving a diagonal correlation matrix for atmospheric distortions. The matrix c_{ik} defined for the Zernikes is slightly non-diagonal. There is no analytic formulation of K-L modes, but they can be represented for instance as an infinite sum of Zernikes by diagonalizing the matrix c_{ik}.

Due to the statistical independence of the K-L coefficients representing phase distortions, correcting the K-L modes is the most effective way to compensate turbulence, if a fixed degree of freedom is given.

Compared to the decay rate of $N^{-0.87}$ when compensating Zernikes, a slightly faster rate of decrease is obtained when K-L modes are used (Roddier, 1999b). The first few K-L modes are, however, very similar to Zernikes. This can be seen for instance in figure 3.1, where a few examples of the K-L modes are shown (no central obstruction in this case).

Section 3.2 explains how the wavefront reconstruction is done in practice — whether a modal basis is used or not.

Modal base in OCTOPUS

In OCTOPUS, the chosen basis can be either Zernike polynomials or Karhunen-Loeve modes (in this thesis only K-Ls are considered). However, the deformable mirror is not able to produce exact K-Ls or Zernikes.

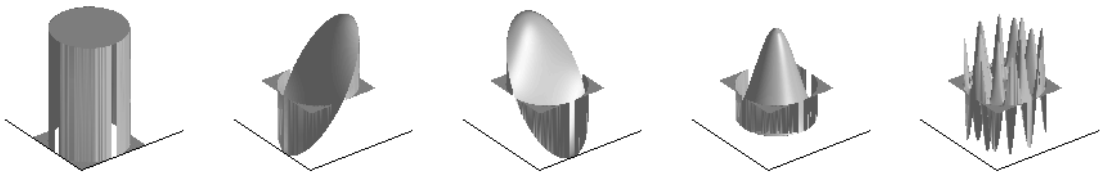

Figure 3.1: Examples of Karhunen-Lóeve modes. From left to right modes 1–4 and 50 are shown. The first four modes are very similar to the Zernikes piston, tip, tilt and defocus.

The actual mirror modes are calculated to best — in the least mean square (LMS) sense — approximate the given theoretical base. We also scale the modes such that each gets a maximum value of one. The exact shape of the modes slightly depends on the chosen influence functions. A few examples of the mirror mode radial cuts are shown in figure 3.2. It illustrates the differences from the corresponding K-L modes shown in figure 3.1. The correspondence is good: only small artifacts at the aperture borders and slight ripples on top of the piston can be seen.

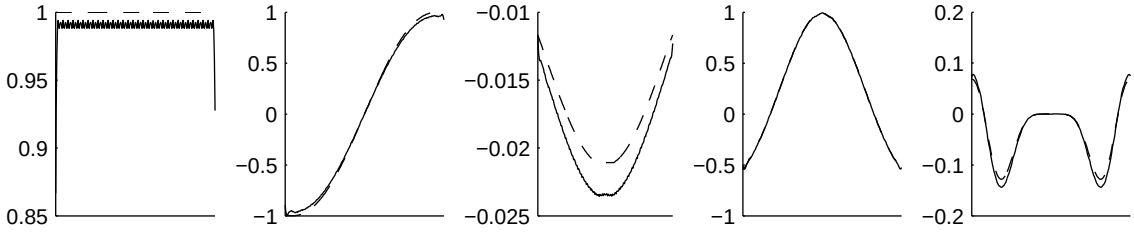

Figure 3.2: Radial plots of the Karhunen-Lóeve modes shown in figure 3.1 (dashed lines) and mirror modes approximating the K-L modes (solid lines). Rigaut's influence functions and an actuator grid of 32×32 are used. From left to right modes 1–4 and 50 are shown.

Especially with bigger systems the choice of a modal basis can have some problematic features. As the actuators are not able to create exactly the Zernikes or K-Ls, some of their theoretical properties are lost — most importantly the mirror modes can no longer be considered exactly orthogonal or linearly independent. Also the pixel discretization might produce small simulation artifacts. The high-order Zernikes and K-Ls especially have many high frequency components that cannot be produced with low resolution.

Therefore, a decoupling matrix of the modes must be considered when the orthogonality assumption is necessary. The matrix is defined as

$$C_m(i,j) = \int M_i(\mathbf{x}) M_j(\mathbf{x}) \mathrm{d}\mathbf{x}, \tag{3.6}$$

where the integrating corresponds to an inner product. This matrix quantifies the deviations from the orthogonality and can be used to find modal expressions

$[a_1 \ \dots \ a_n]^T$ of a phase $\phi(\mathbf{x})$ for an arbitrary set of modes,

$$\begin{bmatrix} a_1 \\ \vdots \\ a_n \end{bmatrix} = [C_m(i,j)]^\dagger \begin{bmatrix} \int M_1(\mathbf{x})\phi(\mathbf{x})\mathrm{d}\mathbf{x} \\ \vdots \\ \int M_n(\mathbf{x})\phi(\mathbf{x})\mathrm{d}\mathbf{x} \end{bmatrix}, \tag{3.7}$$

where $[\cdot]^\dagger$ denotes a pseudo-inverse.

As an example, figure 3.3 shows the decoupling matrix of the mirror modes for a case with 40×40 subapertures. The ratio of C_m diagonal energy and total energy is 0.955 when all the 1347 modes are considered. However, if 25% of the modes are truncated, the ratio becomes 0.993.

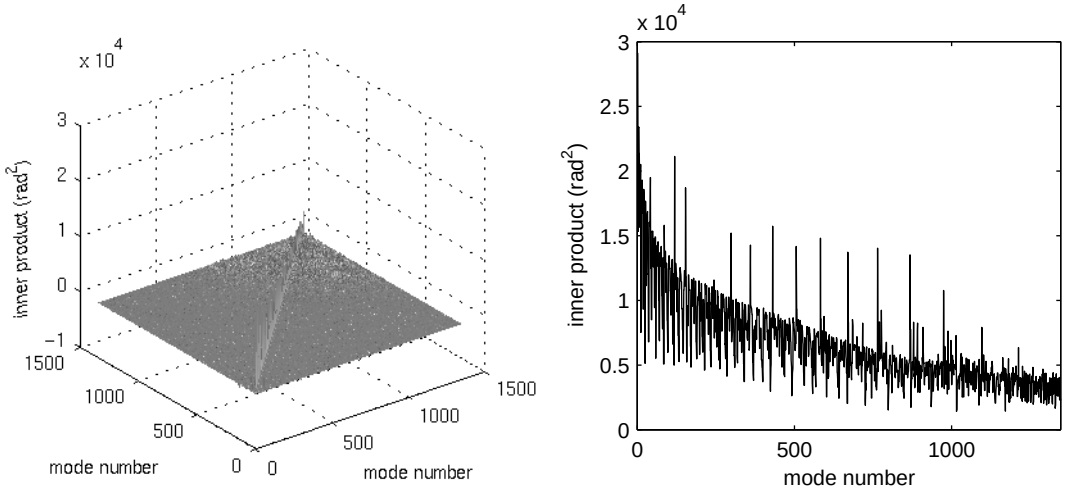

Figure 3.3: Left: the mode decoupling matrix of K-L modes for a system with 40×40 subapertures and no central obstruction (Rigaut's influence functions are used). Right: the diagonal of the decoupling matrix.

Thus, in some cases the orthogonality approximation is viable. Nevertheless, tasks requiring accuracy, such as computing a modal projection of a phase, must be done with the exact knowledge of the decoupling matrix.

The extent of the linear dependency of the modes can be also demonstrated for the case shown in figure 3.3. As seen in the left graph of the figure, the inner products of the higher modes get significant non-zero values also when $i \neq j$. Thus, the higher modes are more coupled than the low order modes. The condition number (ratio of greatest and smallest singular values) of the whole decoupling matrix is over 10^{15}. If the 100 last modes are removed, the condition number becomes 200 and removing 25% of the modes gives a condition number smaller than 7.

Thus, exact modal projections of a phase can be given only for a subset of all the mirror modes. Nonetheless, we show that successful modal approaches can be applied with the current basis (see Section 5.5.2). This is possible since we chose to control only the lowest mirror modes (25–35% of the highest modes should be removed).

3.2 Wavefront reconstruction

Regardless of the type of WFS or the modal base used, the approach to reconstruct the wavefront is usually the same. A linear relationship between measurements $\mathbf{s}$ (an N element vector) and the DM commands $\mathbf{v}$ (an N_a element vector) is assumed,

$$\mathbf{v} = B_z^\dagger \mathbf{s}, \tag{3.8}$$

where $B_z^\dagger$ is the so-called *command matrix*. The measurements are organized into a column vector $\mathbf{s}$, and the commands (the voltages for each actuator) are obtained in the *control vector* $\mathbf{v}$. Thus, the reconstruction problem simplifies to finding the best possible command matrix $B_z^\dagger$.

In general, two approaches exist to address the problem. The first is called the *zonal* approach. It begins by finding out (experimentally measuring) directly the *zonal interaction matrix* B_z. This is done by activating each actuator once and recording the corresponding measurements. These measurement vectors are then collected into the columns of the interaction matrix B_z. Thus, the matrix describes the linear relation between the applied commands $\mathbf{v}$ and the measurements $\mathbf{s}$,

$$\mathbf{s} = B_z \mathbf{v}. \tag{3.9}$$

Then, a pseudo-inverse of B_z is obtained to compute $B_z^\dagger$. A typical minimization criteria $||\mathbf{v} - B_z^\dagger \mathbf{s}||^2$ leads to a least mean squares (LMS) equation $\left(B_z^T B_z\right)\mathbf{v} = B_z^T \mathbf{s}$. It, however, does not have a unique solution since $B_z^T B_z$ is not invertible. This happens because the WFS is non-sensitive to a constant phase change over the aperture (piston mode). In addition, as explained in Section 3.1, the best way to compensate a wavefront, when given a limited number of free parameters, would be to compensate the first N K-L modes (in practice, it is more complicated since the mirror does not produce exact K-Ls). However, the zonal reconstruction ignores this and simply concentrates on the effects of a single actuator at a time.

The issues with the interaction matrix inversion lead to the second approach of wavefront reconstruction, and they are called the *modal methods*. In those, the interaction matrix is recorded by activating the mirror modes instead of single actuators.

This means that the obtained *modal interaction matrix* B having a dimension $N \times M$ describes the relation between the activated modes (ordered in an M element vector $\mathbf{c}$) and the measurements similarly to equation (3.9),

$$\mathbf{s} = B\mathbf{c}. \tag{3.10}$$

Here the zonal command vector $\mathbf{v}$ is replaced by the modal coefficients $\mathbf{c}$.

The inversion (or actually a pseudo-inversion) of B leads to the *modal command matrix* $B^\dagger$. When it is multiplied by the WFS measurement vector $\mathbf{s}$, the combination of mirror modes $M_i(\mathbf{x})$ best approximating the incoming phase is obtained. Typically, the mirror modes are chosen to be the approximation of the Zernike or K-L modes. The required actuator voltages are then computed by a multiplication with a mode-to-actuator matrix Z. Thus, in the modal approaches, the reconstruction matrix can be decomposed as

$$B_z^\dagger = ZB^\dagger, \tag{3.11}$$

where matrix Z is designed to map the modal coefficients into a vector containing the actuator voltages and $B^\dagger$ describes the relation between the measurements and the compensating mirror modes.

When inverting the modal interaction matrix B, the approach leads to a similar minimization equation $||\mathbf{c} - B^\dagger \mathbf{s}||^2$. This, however, gives the pseudo-inverse of B much easier (compared to zonal methods) since the non-detectable piston mode can be excluded from $\mathbf{c}$.

However, in most cases removing only the piston mode is not enough, since also some of the higher modes are badly seen. This is partly due to the sensor geometry restrictions. For instance, the SH-WFS is insensitive to the so-called *waffle mode*, where the actuators take positions opposite to each other (e.g., -1, 1, -1, 1, ...) (Makidon et al., 2005). In addition, the higher order modes contain larger spatial frequencies to which the sensor is less sensitive. In MCAO there are also more complicated unseen modes relating to the specific combinations of the several DMs. This leads to different strategies for how to obtain the command matrix from the interaction matrix.

3.2.1 Truncated singular value decomposition

The most straightforward approach for inverting the interaction matrix is to use a truncated SVD (singular value decomposition), often abbreviated as T-SVD.

By using the SVD the interaction matrix obtained through the calibration measurements is written as

$$B = U\Sigma V^T, \tag{3.12}$$

where U and V are unitary matrices and Σ is a diagonal matrix containing the singular values of the WFS interaction matrix. Thus, the command matrix can be consequently written as

$$B^\dagger = V\Sigma'^{-1}U^T, \tag{3.13}$$

where Σ'^{-1} is a diagonal matrix whose elements are $1/\Sigma_{ii}$ if $\Sigma_{ii} \neq 0$ and 0 otherwise. This corresponds to removing the effect of badly seen modes — the measurement of a mode having a zero eigenvalue has no effect on the AO control.

In practice, however, the eigenmode filtering is not that simple. Instead of removing the zero eigenvalues, an artificial limit for the truncation must be set. A common solution is to use a given fraction of the maximum eigenvalue, for instance 1/100 or 1/1000.

Another popular workaround used instead (or together) with T-SVD is to limit the number of controlled modes. In theory, an AO system is able to control as many modes as it has actuators. In practice, it is rarely the case. Typically at least 25–35% of the available mirror modes need to be truncated for the equation (3.10) to be easily invertible.

The presence of such ad hoc constants is of course undesirable and several methods have been presented to solve the best possible reconstructor. Next the most important ones are briefly discussed.

3.2.2 Other approaches

Besides the simple truncated SVD, Bayesian inference is also applied while computing the command matrix. This was proposed, for instance, by (Law and Lane, 1996).

The measurement always contains noise that comes from the limited number of arriving photons (photon noise) and detector read-out errors. This leads to updating equation (3.10) (or (3.9) in a zonal approach),

$$\mathbf{s} = B\mathbf{c} + \mathbf{n}, \tag{3.14}$$

where noise statistics is normally assumed Gaussian and the modal command vector $\mathbf{c}$ can be also replaced by its zonal version $\mathbf{v}$. The a posteriori probability of $\mathbf{c}$ is

$$P(\mathbf{c}|\mathbf{s}) = \frac{P(\mathbf{c})P(\mathbf{s}|\mathbf{c})}{P(\mathbf{s})}, \tag{3.15}$$

where *a priori* knowledge, $P(\mathbf{c})$, is known from the statistics of the atmospheric aberrations. When maximizing the logarithm of $P(\mathbf{c}|\mathbf{s})$, it follows that

$$\mathbf{c} = \underbrace{\left(B^T\mathbf{C}_n^{-1}B + \mathbf{C}_\phi^{-1}\right)^{-1} B^T\mathbf{C}_n^{-1}}_{B^\dagger}\mathbf{s}, \tag{3.16}$$

where $\mathbf{C}_n$ is the covariance of $\mathbf{n}$ and $\mathbf{C}_\phi$ is the covariance of $\mathbf{c}$.

The drawback of this Bayesian modeling is that the solution is valid only when the turbulence statistics are known. If the AO systems are run in a closed-loop — as they always are — equation (3.16) is no longer valid. In closed-loop the matrices $\mathbf{C}_n$ and $\mathbf{C}_\phi$ cannot be computed analytically.

However, maximum a posteriori (MAP) reconstruction based on the AO closed-loop variances calculated in (Véran et al., 1997) has been used in (Kasper, 2000). The differences of the reconstruction methods are also further discussed and their performances analyzed in (Kasper, 2000).

In addition, even more sophisticated methods have been proposed. For instance, a dynamic reconstructor based on the previous controller values has been developed in (Wild, 1996). In that approach also the effect of the system time lag can be taken into account.

Nevertheless, as discussed for instance in (Wiberg et al., 2005), the reconstruction problem can be fully separated from the dynamic control. This has also been a popular approach in the most recent works.

3.3 Dynamic control

After the wavefront reconstruction is made, a dynamic controller must be applied to effectively cancel the wavefront distortions in a closed-loop operation.

Several approaches have been used in the control design. In this section they are briefly summarized. At first, however, the dynamic behavior of an AO loop is illustrated.

3.3.1 AO system dynamic behavior

Figure 3.4 shows the components of an AO system. The incoming wavefront (turbulence) is reflected from the DM, i.e., the correction computed by the control system is subtracted from it. The resulting residual wavefront is then directed to the WFS.

Dynamics of the WFS is characterized by a discrete operation. The WFS integrates the incoming phase during a constant time interval T. This delay effectively determines the most significant temporal characteristics of the AO system.

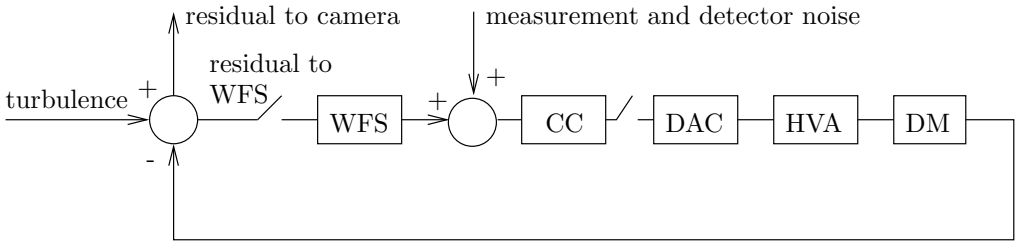

Figure 3.4: Block diagram of a typical AO loop (WFS: wavefront sensor, CC: control computer, DAC: digital to analog converter, HVA: high voltage amplifier and DM: deformable mirror).

After the frame delay T, the WFS measurements are fed into a control computer (CC), sometimes also called as the real time computer (RTC). It performs computations that typically last a significant fraction of T, but in a complicated system the delay can be even bigger. RTC also implements the control law designed by system engineers.

Commands from the RTC go into a digital to analog converter (DAC). It is typically implemented as a zero-order hold. DAC gives the voltages to a high voltage amplifier (HVA) and the amplified voltages are then moving the actuators in DM.

As discussed in Section 2.3, the DM can have significant dynamics (hysteresis and delay). It has been concluded that when using a piezo-stacked DM with sampling frequencies higher than a few hundred Hertz, the dynamics should be taken into account in the AO control (Le Roux et al., 2004). Other types of DMs typically have even stronger time lags.

It has also been shown by (Paschall and Anderson, 1993) that such effects can be taken into account using state-space formalism discussed later in Section 3.3.4. However, in this thesis our aim has been to study the first order effects in the AO loop and we have neglected the DM dynamics. This is a common approach also in many other AO control related works.

With the assumptions stated above, the system behavior can be fully characterized by the WFS integration delay T, computation delay τ and the used controller.

Also more complex models have been considered. For instance, the WFS integration in some cases can be only a part of the total frame (Looze et al., 2003). In addition, the requirement of low latency dictates that the WFS and DM should be handled segmentwise (i.e., measurement read-out and DM update are not single operations) (Fedrigo et al., 2006).

In this thesis, however, the focus is more on the compensation of the WFS

inaccuracies and on the general sensing concept. The exact modeling of the system dynamics is postponed to later stages.

Thus, besides neglecting the DM dynamics, a convenient assumption that τ is an integer number of T is made. Unless otherwise mentioned, it is simplified even further by assuming a single frame computation delay, that is $\tau = T$.

With these assumptions the AO loop can be regarded completely as a discrete-time system having a total time lag of two iterations. The corresponding open loop transfer function is

$$H(s) = z^{-2} CC\,(z)\,, \tag{3.17}$$

where $CC\,(z)$ is the transfer function of the controller, usually written as

$$CC(z) = \frac{\sum_{i=0}^{p} b_i z^{-i}}{1 + \sum_{i=1}^{l} a_i z^{-i}}, \tag{3.18}$$

where a_i and b_i are the parameters for a general linear controller.

When considering a modal approach, the AO loop can be illustrated as shown in figure 3.5. The residual wavefront, represented as a sum of modal coefficients, goes into the WFS. Then additional noise is added to the measurement $\mathbf{s}(k)$ (represented as a vector). A conversion to a modal space is a multiplication by a modal command matrix $B^{\dagger}$ and each modal coefficient is controlled by a separate controller. The outputs of the controller are then converted into an actuator positions by a linear operation.

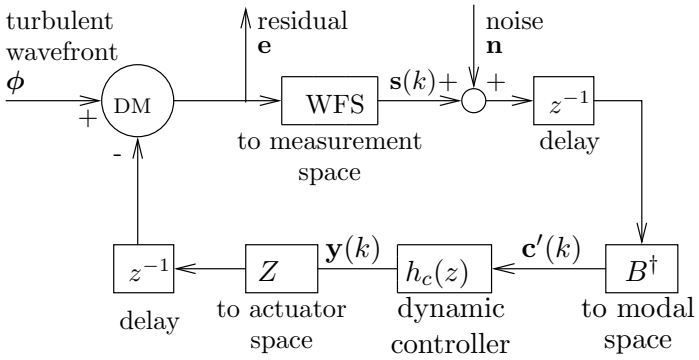

Figure 3.5: Illustration of a modal control scheme in a discrete case with a single frame computational delay.

Unless otherwise mentioned, this simplified AO loop model is used in the following parts of this thesis.

3.3.2 Optimal modal gain integrator

Dynamic control can be designed using traditional control engineering as for instance in (Wirth et al., 1998), or more specialized solutions can be applied to find the optimal control parameters.

One of the first attempts to design optimal control for an AO system was the optimal modal gain integrator (OMGI) proposed by (Gendron and Lena, 1994). The

idea was to minimize the residual variance by adjusting the loop gain of a simple integrator. The concept has then been used in practice in several systems, initially in ComeOnPlus (Gendron and Lena, 1995) and later for instance in Nasmyth Adaptive Optics System (NAOS) (Rousset et al., 2000).

Next the principles of OMGI are briefly described for a completely discrete AO system illustrated in figure 3.5.

The open loop transfer function of the AO loop of the ith mode (defined without the integrator loop gain) is

$$H_{\mathrm{ol}}(z) = \frac{z^{-d_1}}{z-1}, \tag{3.19}$$

where the constant d_1 is the computational delay, typically $d_1 = 1$.

Thus, following the diagram in figure 3.5, using notation

$$h_{\mathrm{sys}}(z) = h_c(z)\ z^{-d_1}, \tag{3.20}$$

where the controller is the simple integrator $h_c(z) = z/(z-1)$ and assuming the WFS can be interpreted as a multiplication by the interaction matrix B (linear mapping from modal phase representation to the measurements), the system can be characterized by a relation

$$\mathbf{e}(z) = \boldsymbol{\phi}(z) - H_{\mathrm{ol}}(z)\ GB^{\dagger}B\ \boldsymbol{\phi}(z) + h_{\mathrm{sys}}GB^{\dagger}\ \mathbf{N}(z), \tag{3.21}$$

where G is a matrix defining the loop gains of the simple integrator. If the controlled modes are not coupled, each mode has its own loop gain on G's diagonal. $\mathbf{e}(z)$ and $\boldsymbol{\phi}(z)$ are functions of M elements describing the Z-transforms of the residual phase and the incoming turbulence in modal space.

Equation (3.21) describes the system using the actual controlled mirror modes. However, especially when the controlled modes are not orthogonal in mirror space, the actual control should be done in the so-called *system eigenspace* diagonalizing the interaction matrix B. Otherwise equation (3.21) should be considered as a MIMO system (Multiple Inputs, Multiple Outputs) and the gain design using the conventional OMGI approach would be impossible.

Next the transformation to the system eigenspace is illustrated using the formalism similar to that used in (Quiros-Pacheco et al., 2004; Quiros-Pacheco, 2007).

At first, the system equation (3.21) is modified to find the correct transformation matrices for the coefficients $\mathbf{e}$, $\boldsymbol{\phi}$ and $\mathbf{N}$.

The matrices B and $B^{\dagger}$ can be represented using the SVD decomposition as

$$B = U\Sigma V^T, \tag{3.22}$$

$$B^{\dagger} = V\Sigma^{-1}U^T. \tag{3.23}$$

By multiplying the equation (3.21) by ΣV^T, it becomes

$$\begin{aligned}\Sigma V^T\mathbf{e}(z) = \Sigma V^T\boldsymbol{\phi}(z) &- \Sigma V^T H_{\mathrm{ol}}(z) GV\Sigma^{-1}U^T U\Sigma V^T\mathbf{e}(z)\\ &+ \Sigma V^T h_{\mathrm{sys}}(z) GV\Sigma^{-1}U^T\mathbf{N}(z).\end{aligned} \tag{3.24}$$

Now, with the notations

$$\mathbf{e}' = \Sigma V^T \mathbf{e}, \tag{3.25}$$

$$\boldsymbol{\phi}' = \Sigma V^T \boldsymbol{\phi}, \tag{3.26}$$

$$\mathbf{N}' = U^T \mathbf{N}, \tag{3.27}$$

$$H_{\mathrm{ol}}(z)G' = \Sigma V^T H_{\mathrm{ol}}(z) G V \Sigma^{-1}, \tag{3.28}$$

$$h_{\mathrm{sys}}(z)G' = \Sigma V^T h_{\mathrm{sys}}(z) G V \Sigma^{-1}, \tag{3.29}$$

equation (3.24) becomes

$$\mathbf{e}'(z) = \boldsymbol{\phi}'(z) - H_{\mathrm{ol}}(z)G'\mathbf{e}'(z) + h_{\mathrm{sys}}(z)G'\mathbf{N}'(z), \tag{3.30}$$

which is the system equation (3.21) in a different space. In this space the modal optimization is more convenient since the eigenmodes are not coupled.

Since the modes are not coupled, the residual variance of each mode (in the system eigenspace) can be written in the same form as done by (Gendron and Lena, 1994),

$$\langle e_i' \rangle = \int H_{\mathrm{cor}}(z = e^{-2\pi j T_s f}, g_i') |\phi_i'(f)|^2 \mathrm{d}f + \sigma_n \int H_{\mathrm{n}}(z = e^{-2\pi j T_s f}, g_i') \mathrm{d}f, \tag{3.31}$$

where T_s is the WFS sampling time, σ_n is an input noise variance and is assumed constant in each subaperture, $|\phi_i'(f)|^2$ is the temporal power spectrum of the ith modal component and the functions $H_{\mathrm{cor}}(\cdot)$ and $H_{\mathrm{n}}(\cdot)$ are called respectively *correction transfer function* and *noise transfer function*,

$$H_{\mathrm{cor}}(z = e^{-2\pi j T_s f}, g_i') = \left| \frac{1}{1 + g_i' H_{\mathrm{ol}}(z = e^{-2\pi j T_s f})} \right|^2, \tag{3.32}$$

$$H_{\mathrm{n}}(z = e^{-2\pi j T_s f}, g_i') = \left| \frac{h_{\mathrm{sys}}(z = e^{-2\pi j T_s f})}{1 + g_i' H_{\mathrm{ol}}(z = e^{-2\pi j T_s f})} \right|^2. \tag{3.33}$$

Here the g_i' are the diagonal elements of G'. The real gains (G) applied to the system are obtained from the transform

$$G = V \Sigma^{-1} G' \Sigma V^T. \tag{3.34}$$

The obtained gain matrix G is no longer diagonal unlike the gain matrix G' in the system eigenspace.

The advantage of the OMGI method is its low computational requirements. As no temporal filtering is done in the modal space, all the reconstruction and controller operations can be incorporated into a single command matrix. The temporal controller operations (a simple integrator) can be applied to the actuator commands alone.

This approach, however, prevents temporal operations in the modal space. As the actuator commands are strongly coupled (unlike the controlled modes), it is not possible to design an effective temporal controller working only in actuator space.

The lack of this limited temporal memory is a major disadvantage of the OMGI method. It has been shown for instance in (Le Roux et al., 2004) that OMGI cannot predict the temporal turbulence evolution in the same manner as more advanced minimum variance controllers. This naturally leads to an inferior performance.

3.3.3 Predictive control

A more advanced control algorithm for AO, a modal predictor, was presented in (Dessenne et al., 1998). The idea was to apply an optimized dynamical controller for each mirror mode separately. The optimization was done by minimizing the residual variance using a recursive least-squares algorithm.

Since the temporal controlling is done in the modal space, the computational requirements of the control and reconstruction are essentially doubled compared to a simple integrator or OMGI. This is characteristic to all more advanced control approaches involving two large transforms (most often matrix-vector multiplications) during one time step: at first from measurement to the modal space, then from modal space to the actuator space.

Next the main points of the algorithm are briefly illustrated.

As each mode is controlled separately, we omit the modal index in the following equations for simplicity. The control law in (Dessenne et al., 1998) is defined as

$$y(k) = \boldsymbol{\theta}(k)^T \boldsymbol{\varphi}(k), \tag{3.35}$$

where $y(k)$ is a modal mirror coefficient at time step k, $\boldsymbol{\theta}(k)$ and $\boldsymbol{\varphi}(k)$ are vectors of $p+q+1$ elements, and p and q define the orders of the controller. The former vector contains the control parameters and the latter a set of previous DM commands and reconstruction coefficients,

$$\begin{aligned} \boldsymbol{\theta}(k) &= \begin{bmatrix} b_1(k) & \cdots & b_{p-1}(k) & a_0(k) & \cdots & a_{q-1}(k) \end{bmatrix}^T \\ \boldsymbol{\varphi}(k) &= \begin{bmatrix} y(k-1) & \cdots & y(k-p+1) & c'(k-2) & \cdots & c'(k-q-1) \end{bmatrix}^T , \end{aligned} \tag{3.36}$$

where $b_1, \ldots, b_{p-1}$ and $a_0, \ldots, a_{q-1}$ are the controller parameters. The parameter vector $\boldsymbol{\theta}(k)$ is computed at each time step such that the estimated residual error,

$$\epsilon = \sum_{L \le j \le k} \left[y(j) - \boldsymbol{\theta}^T \boldsymbol{\varphi}(j) \right]^2 , \tag{3.37}$$

is minimized. Here L is the number of time steps used for the equation to minimize the residual variance.

This means solving a small least mean square problem at each time step. This can be done by computing $\boldsymbol{\theta} = (\Phi^T \Phi)^\dagger \Phi^T E$, where Φ and E are collections of earlier coefficients as

$$\Phi = \begin{bmatrix} \boldsymbol{\varphi}(k-L)^T \\ \vdots \\ \boldsymbol{\varphi}(k)^T \end{bmatrix} , \tag{3.38}$$

$$E = \begin{bmatrix} y(k-L)^T - \boldsymbol{\theta}(k-L)^T \boldsymbol{\varphi}(k-L) \\ \vdots \\ y(k)^T - \boldsymbol{\theta}(k)^T \boldsymbol{\varphi}(k) \end{bmatrix} . \tag{3.39}$$

It was found that a direct inversion of $\Phi^T \Phi$ in some cases is too unreliable. Especially the transient adjustment period at the beginning of the loop is problematic

since high wavefront distortions are usually involved. When working with a pyramid WFS unable to measure these high distortions, it is desirable to restrict the overly large controller parameters obtained from the LMS equation.

Thus, the inversion of $\Phi^T\Phi$ was made using a truncated SVD in the same way as when inverting the interaction matrices (see section 3.2.1). This approach was found very reliable, and it is shown later, how the modal predictor is applied with a pyramid sensor.

3.3.4 State-space formalism

Besides the control methods shown earlier, several more sophisticated solutions for AO control have been proposed. For instance, an explicit model of the atmospheric turbulence has been used in predictive control (Gavel and Wiberg, 2003; Wiberg et al., 2006).

Solutions have been also sought to ease the computation requirements of the large next generation AO systems. For instance, it has been proposed that certain modes could be controlled at different frame rates (Correia et al., 2006).

However, the most recent works have often preferred the state-space formalism. Next a short summary of this is given.

State-space formalism is successfully applied in AO control by several authors. The minimization of the residual variance can be formulated as a Linear-Quadratic-Gaussian (LQG) optimization problem and the existing effective algorithms in optimal control are exploited.

One of the first proposals for LQG formulation for an AO application was done by (Paschall and Anderson, 1993). They demonstrated by Monte Carlo simulations the use of the Kalman filter for a small AO system controlling 44 Zernike modes. They also demonstrated that the formalism makes it possible to take into account in the system model for instance the DM dynamics and the fact that a frame rate may not be an integer number of the WFS integration times.

A similar approach was then taken by (Looze et al., 2003) to control modally an AO system similar to MACAO (described in (Donaldson et al., 2000)). Unlike (Paschall and Anderson, 1993), they restricted the LQG problem to consider each controlled mode separately to save computation time. This approach is then otherwise similar to the predictor by (Dessenne et al., 1998) discussed in the previous section, except that it separates the problem of atmospheric identification and the applied control.

The LQG formalism is especially important in MCAO control. As discussed for instance in (Le Roux et al., 2004), in MCAO there exist so called non-seen modes. They are combinations of the used mirror modes that produce no response to the WFSs, but in other parts of the field can cause significant phase deformations. The LQG formalism — when used globally — is also useful in SCAO since the mode-by-mode control is not able to handle the small coupling between the mirror modes.

Nevertheless, it has been shown in (Looze, 2006) that in ideal conditions the optimal LQG control approaches the most commonly used simple integrator. The ideal conditions are defined as zero computation loop delay, no DM dynamics or isotropic first order temporal atmospheric aberrations.

Other simulation-based demonstrations of the state-space formalism for MCAO control include (Petit et al., 2004; Piatrou and Roggemann, 2005). In addition, works concentrating on XAO do exist (Le Roux, 2006; Le Roux and Carbillet, 2006). It has also been proposed in (Muradore et al., 2006) to use sub-space identification techniques (in MIMO case) to determine how the WFS sees the turbulence. The identified AO system model is then used together with an LQG controller to minimize the residual variance.

Although these methods have not been explicitly tested in the context of this work, they could potentially improve the performance of the results shown later in Chapter 5.

Chapter 4

Simulations of ground layer adaptive optics

This chapter concentrates on analyzing the performance of GLAO. The concept of correcting only the ground layer is described in more detail in Section 4.1 and Section 4.1.3 gives a short summary of the previous work on the subject. In Section 4.2 it is described how the analytic GLAO estimates are computed. Then, in Section 4.3, the simulations to study the robustness of GLAO control are explained. The results of these extensive simulations, mostly published in (Korkiakoski et al., 2006), are then shown in Section 4.4. The conclusions are presented in Section 4.5.

4.1 Introduction to GLAO

Ground Layer Adaptive Optics (GLAO) is a recent concept, proposed by (Rigaut et al., 2000; Rigaut, 2002), to compensate atmospheric turbulence to improve the observations by ground based telescopes. Unlike traditional AO, GLAO aims to compensate a relatively wide field of view (1'–10') at the expense of image quality.

This is possible since measurements have shown that most of the atmospheric turbulence occurs at low altitudes (first few hundred meters) (Racine and Ellerbroek, 1995; Le Louarn et al., 2000). By correcting the effect of only this "ground layer", it is possible to obtain a significant correction over an area of several arcmins.

While a typical GLAO system considers correcting the field up to 8', also much larger corrections have been studied. Such systems are sometimes referred as very wide GLAO (VWGLAO) (Stoesz, 2006).

4.1.1 Implementation

As mentioned, the correction of the ground layer is achieved by combining the information from several sources. This can be done using sophisticated laser tomography AO (Nicolle, 2006) or just averaging the wavefronts from several guide stars.

The turbulence in the upper layers causes mainly uncorrelated distortions to the corresponding wavefront measurements. Thus, when summing the measurements, the effect of the higher altitudes is canceled out in the averaging process — only the ground layer becomes measured. This is illustrated in figure 4.1.

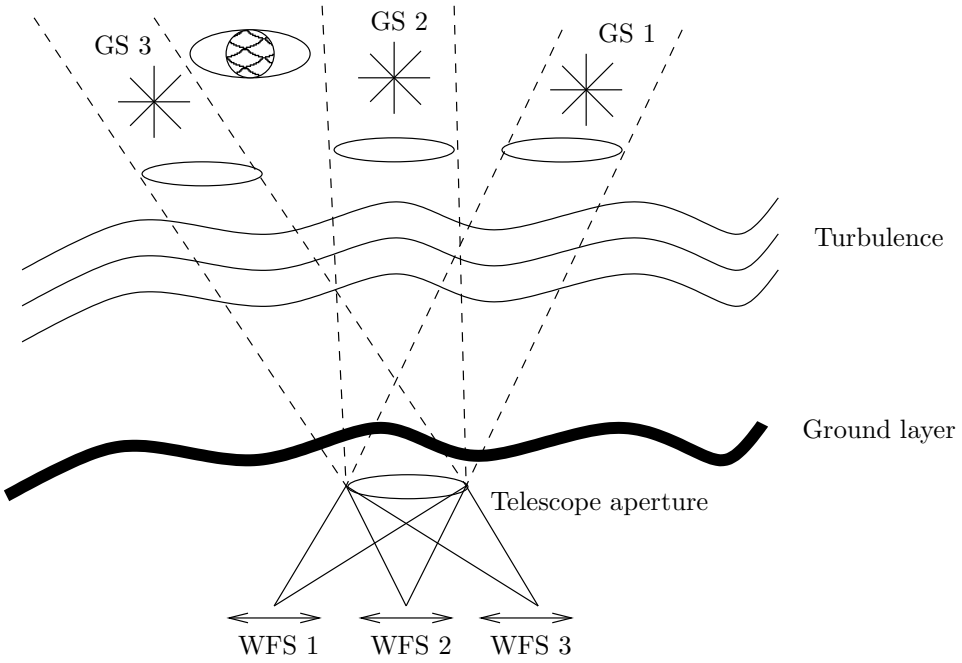

Figure 4.1: Illustration of a GLAO system.

The approach illustrated in figure 4.1 is called the *star oriented* method. Also another method, *layer oriented* approach, can be considered. In it, the wavefronts are detected using a single detector, and the averaging is accomplished directly in the WFS. These two approaches have been found out to be roughly equally good (Nicolle et al., 2005, 2006). In this work only the star oriented method is considered.

The optimum correction of a circular area in the sky is obtained by averaging the wavefronts coming from the borders of that area (Tokovinin et al., 2000). The exact number of the required guide stars, on the other hand, depends on the size of the telescope diameter and the chosen performance.

However, as mentioned before, suitable bright guide stars are scarce objects in the sky. Although the sky coverage of a GLAO system is better compared to SCAO, it can still be improved by using artificial beacons, *laser guide stars* (LGS). In addition, the LGSs can be positioned at arbitrary positions in the field to optimize the correction in the direction of the science targets.

In the following text, the guide stars are referred either as LGSs or natural guide stars (NGSs).

4.1.2 Laser guide stars

Laser guide stars are artificially created light sources on the sky (Sandler, 1999a,b). One or several laser beams are propagated to the direction where reference beacons are required. The light is back-scattered from the LGS and is then used to sense the wavefront.

Two techniques for implementing an LGS have been proposed. The first technology is based on Rayleigh backscatter from the atmosphere at 15–20 km and is known as *Rayleigh LGS*. A pulsed laser beam is shot from the telescope along the line of

sight towards the observed area. The beam is focused in the atmosphere typically at the height of 20 km (or lower) since air becomes too thin at higher altitudes. The observation of the backscatter must be synchronized with the pulses such that only the light scattered at the correct altitude is used for wavefront sensing.

At the moment the required laser technology already exists for producing good Rayleigh LGSs and such systems have been successfully demonstrated since the 1990s (Fugate, 1994). It has been shown that laser powers around 100 W at visible wavelengths produce a sufficient photon return for spots up to 20 km (Sandler, 1999b).

The second method is called *sodium LGS*. It takes advantage of the mesospheric sodium layer in the atmosphere at about 90 km. The principle is somewhat different from the Rayleigh LGS. The laser is focused into the sodium layer and its wavelength must be the same as the sodium absorption wavelength (589 nm). This technology enables the use of both a constant wave and pulsed laser beam.

However, sufficient sodium lasers have been available much shorter period of time than the Rayleigh lasers. They are more expensive and difficult to build because of the spectral restrictions — only a few current lasers have enough power at 589 nm. Nevertheless, successful operational sodium LGS systems (having a laser power of about 5–20 W) have been build for the Lick 3 m telescope (Max et al., 1997) and the Keck II telescope (Wizinowich et al., 2006).

Difficulties

When using LGSs, some fundamental problems (non-existent in classical AO) emerge. The two major effects are so-called *tip-tilt indetermination* and *cone effect* sometimes called also the *focus anisoplanatism* (FA) (Foy, 2000).

Tip-tilt indetermination is due to the fact that an LGS AO is unable to detect the global tip-tilt in the wavefront. As illustrated in figure 4.2, the light coming from a celestial object goes through the turbulent atmosphere only once, where the laser beams does it twice. This makes the global tip-tilt in the turbulence invisible for the LGS. The phenomenon — if not corrected — causes the imaged celestial star to wander around (jitter) at the image plane as the global tip-tilt evolves. That makes the long exposure image to blur.

Solutions and partial solutions to these problems do exist. The tip-tilt indetermination can be corrected using a natural guide star in addition to LGS (Ellerbroek and Rigaut, 2001). In this case, however, as only the tip-tilt is measured, the NGS can be much dimmer (all incoming photons can be concentrated to a single quad-cell spot) and located further away from the scientific target. Thus, a larger sky coverage compared to the pure NGS AO is obtained. An example of such LGS AO system is shown in figure 4.3. It has the tip-tilt sensor located next to WFS and its measurements are used to control the tip-tilt mirror.

Another problem is illustrated right in figure 4.2. The light coming from a LGS arrives to the WFS from a cone — not like the cylindrical beam coming from an infinitely remote celestial object. This means that the shaded areas of turbulence (illustrated in the figure) do not get sampled. As indicated by the figure, this problem is much worse with Rayleigh LGS compared to the sodium LGS.

The cone effect can be partially compensated by using several LGS beacons.

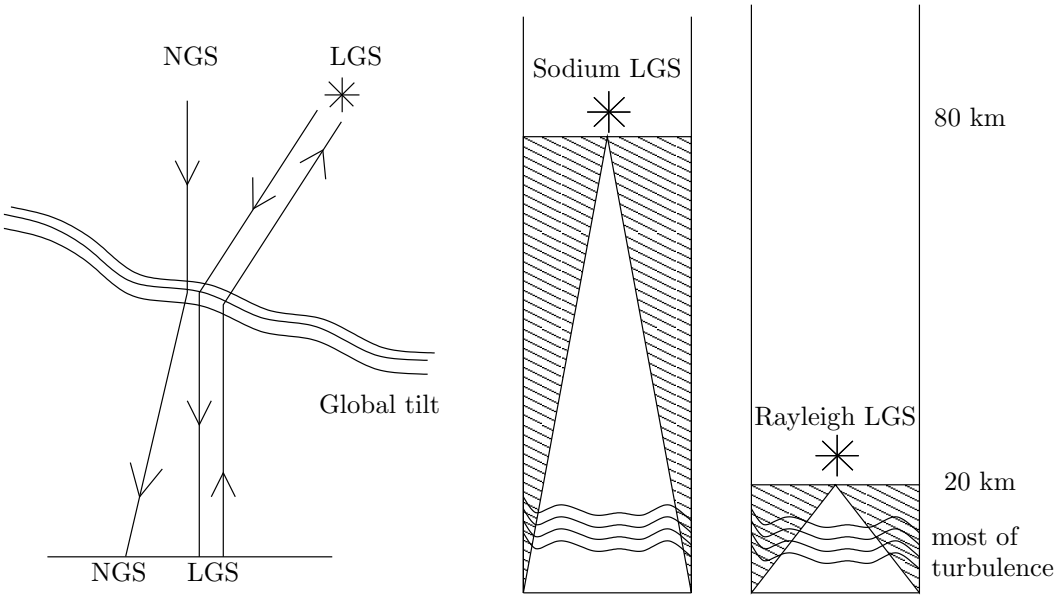

Figure 4.2: Left: illustration of tip-tilt correction problem. Right: illustration of focus anisoplanatism error for sodium and Rayleigh LGS.

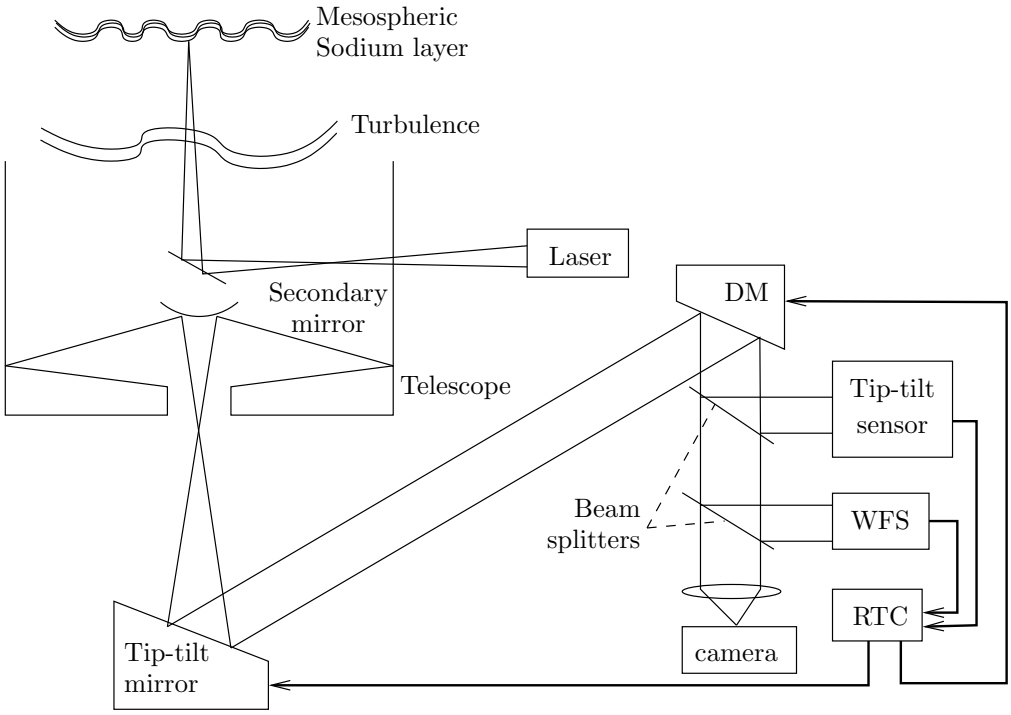

Figure 4.3: Schematic illustration of an LGS AO system.

These enable sampling a bigger proportion of the atmospheric volume, but at the cost of increased complexity and costs.

4.1.3 Previous work on GLAO

After initially proposed by (Rigaut, 2002), GLAO has been extensively studied by several groups through analytic models, Monte Carlo simulations, practical experiments and recently with real demonstrative instruments mounted on telescopes.

The analytic estimates of GLAO, useful for fast parameter exploration, are computed by extending the reasoning illustrated in Section 2.2. The atmosphere is modeled as a set of discrete layers, each obeying von Karman power law. The GLAO correction is modeled as a corresponding set of spatial filters — the damping of the turbulence energy originating from each layer is described by a multiplication by a filter (see Section 4.2). The formulation of the filter depends on the modeled error sources. For instance, to simplify the computations, a common approximation is to neglect several second order AO effect like WFS aliasing or servo lag.

The first analytic GLAO estimates in (Rigaut, 2002) indicated that GLAO can reduce the FWHM — at best — approximately to half of the width of the seeing disk.

Similar analytic GLAO estimates have later been published by several authors (Travouillon et al., 2004; Stoesz et al., 2004a; Tokovinin, 2004). It was shown that a good GLAO estimate requires a very accurate model of the C_n^2 profile. However, all the works still indicated a significant gain given by GLAO.

These analytical results have then been confirmed by numerical simulations. For instance, a summary of several analytical and Monte Carlo based simulation codes for a GLAO comparison was presented in (Andersen et al., 2006b,a). They considered five different codes from different groups. Both analytic tools (PAOLA, CIBOLA, IDL code by (Tokovinin, 2004)) and numerical Monte Carlo simulations (code by (Lloyd-Hart and Milton, 2003) and Durham AO code) were discussed and their results compared. It was concluded that the GLAO performance estimates of all the codes were in excellent agreement — although the Monte Carlo codes gave slightly more pessimistic results since they model more potential error sources. Numerical GLAO simulations made by OCTOPUS have also been published (Le Louarn and Hubin, 2006).

These performance predictions indicate, for instance, that the best seeing limited image quality (available only 20% of the time) can be achieved 60%–80% of the time with GLAO. In addition, the sky coverage of a LGS based GLAO can be almost 100%.

GLAO has also been demonstrated in practice. For instance, the open-loop experiments at Kuiper telescope at Arizona indicated that the widths of the seeing limited stellar images can indeed be reduced by up to a factor of 3 (imaging wavelength from visible up to near infrared, compensated field of view at least 2') (Baranec et al., 2007).

Also the Multiconjucate Adaptive optics Demonstrator (MAD) developed at ESO (Marchetti et al., 2003) has been used to demonstrate GLAO. The laboratory experiments with GLAO corresponded well to the expectations (Marchetti et al.,

2006) and the GLAO on-sky results were even better than expected (Marchetti et al., 2007).

Currently, several projects for real GLAO instruments are being implemented. These include, for instance, the GLAO implementation for the SOAR's SAM instrument (1 Rayleigh LGS) (Tokovinin et al., 2003, 2004) and GRAAL and GALACSI for the ESO's AO facility at VLT (4 sodium LGSs) (Ströbele et al., 2006).

4.2 Analytical estimation

In this section we briefly describe the analytical method to estimate the GLAO corrected PSFs. The approach is described in more detail for instance in (Tokovinin, 2004).

By using the Wiener-Khinchin theorem, the structure function as shown in equation (2.3) can be written as

$$D_\phi(\mathbf{r}) = \left\langle |\phi(\mathbf{x}) - \phi(\mathbf{x}+\mathbf{r})|^2 \right\rangle = 2\Big[\mathscr{F}\{W_\phi(\mathbf{f})\}_{\mathbf{r}=0} - \mathscr{F}\{W_\phi(\mathbf{f})\}\Big], \tag{4.1}$$

where $W_\phi(\mathbf{f})$ is the power spectrum of the phase and $\mathscr{F}\{\cdot\}$ is a Fourier transform.

If the atmospheric turbulence is modeled as a set of discrete layers, the structure function can be written as a sum

$$D_\phi(\mathbf{r}) = 0.423(2\pi/\lambda)^2 \sum_{i=1}^{N} J_i D_i(\mathbf{r}), \tag{4.2}$$

where $J_i = C_n^2 dh$ is the strength of the ith layer's turbulence and $D_i(\mathbf{r})$ is the normalized structure function of the ith layer. The normalized structure function is computed similarly to equation (4.1),

$$D_i(\mathbf{r}) = 2\Big[\mathscr{F}\{W_{\phi,i}(\mathbf{f})\}_{\mathbf{r}=0} - \mathscr{F}\{W_{\phi,i}(\mathbf{f})\}\Big], \tag{4.3}$$

where $W_{\phi,i}(\mathbf{f})$ is the normalized power spectrum of the turbulence of the ith layer. It can be represented as a product of the von Karman phase power spectrum and a filter $|G_i(\mathbf{f})|$ describing the GLAO correction at the ith layer,

$$W_{\phi,i}(\mathbf{f}) = 0.0229\left(|\mathbf{f}|^2 + L_0^{-2}\right)^{-11/6} |G_i(\mathbf{f})|^2, \tag{4.4}$$

where L_0 is the outer scale of the turbulence. In principle, L_0 could also depend on the layer index i, but in this study it is kept the same for all the layers.

In this study we have used two filters given by (Tokovinin, 2004). Both the filters neglect WFS aliasing, servo lag and measurement noise. Thus, they inevitably give over-optimistic GLAO estimates.

The first is called the optimum filter. It describes the correction obtained by averaging the wavefront (or equally averaging the slopes measured by a SH-WFS) from a circle having an angular distance of θ_0 from the field center and a height of h. It is given as

$$G_{\mathrm{opt}}(\mathbf{f}) = 1 - 2R(\mathbf{f})J_0(2\pi|\mathbf{f}|\theta_0 h)\cos\left(2\pi h\ \mathbf{f}\cdot\mathbf{a}\right) + R(\mathbf{f})^2 J_0(2\pi|\mathbf{f}|\theta_0 h)^2, \tag{4.5}$$

where $R(\mathbf{f})$ describes the DM smoothing being modeled as a simple cutoff beyond frequency $1/(2d)$ for actuator pitch d, $\mathbf{a}$ is the angle between the imaged object and the field center, and $J_0(\cdot)$ is the zero order Bessel function.

The second filter takes into account the effect of limited number of reference beacons (sodium LGS). To ease the computational requirements it uses a heuristic approximation: at the height of h the wavefront from a LGS at height H is reduced by a factor of $\gamma = 1 - h/H$ from the wavefront from a celestial object. Then the filter for K LGSs can be written as

$$|G_{\text{mult}}(\mathbf{f})|^2 = 1 - 2\gamma R(\mathbf{f}) A(|\mathbf{f}|) \sum_{k=1}^{K} w_k \cos\left[2\pi\mathbf{f}\cdot(\mathbf{a}_k - \mathbf{a})h\right] + \gamma^2 R(\mathbf{f})^2 \sum_{k=1}^{K}\sum_{k'=1}^{K} w_k w_{k'} \cos\left[2\pi\mathbf{f}\cdot(\mathbf{a}_k - \mathbf{a}_{k'})h\right], \quad (4.6)$$

where w_k are the LGS weights ($\sum w_k = 1$), $\mathbf{a}$ is the object location as in equation (4.5) and $\mathbf{a}_k$ are the guide star locations. $A(f)$ is an average function defined as

$$A(f) = \frac{J_1(\pi f D h/H)}{\pi f D h/H}. \quad (4.7)$$

The heuristics used here give better results the higher is the LGS and the lower is the turbulent layer. In our case with sodium LGSs at 90 km and turbulence profile shown below in Table 4.1, the use of equation (4.6) is well justified.

It should also be noted that when the GLAO PSFs are estimated this way, it has been implicitly assumed (through the filter definitions (4.5) and (4.6)) that the tip-tilt component of the wavefront is corrected. That, however, cannot be done using LGSs, but a NGS is needed. This requires a small addition into equation (4.3), but it has been shown (Tokovinin, 2004) to have only negligible impact on the total results in most cases.

After the structure function is known, the PSF is then computed using the optical transfer function given by equation (2.16).

4.3 Simulations with OCTOPUS

This section describes the results of the simulations, which were carried out to illustrate the performance of GLAO.

We restrict our study to a few specific configurations and consider only sodium LGSs at 90 km as they are the most probable option for the next generation LGS AO systems at ESO. The basic parameters and the used turbulence profile of the studied systems are shown in Table 4.1. We use the same turbulence profile (an average of the profiles measured at Paranal Observatory) in all the selected cases.

The simulations can be classified roughly into three categories. At first, we compare the GLAO simulations with OCTOPUS to the analytic estimates computed as shown in the previous section (see Section 4.4.1). This is done to ensure that the performance estimations of both methods agree. Secondly, we compute the GLAO estimates in selected difficult cases having asymmetric noise patterns and compare

Table 4.1: System parameters and turbulence profile in this study.

WFS type	Shack-Hartmann
λ_{WFS}	0.589 μm
Read noise	3 e^- rms
Sampling frequency	500 Hz
Controller	Simple integrator
λ_{img}	2.2 μm
total r_0 at 0.5 μm	0.11 m
Outer scale L_0	25 m
Radius of corrected area	4'
Guide stars	LGSs at 90 km
Number of layers	10
Number of iterations	10240
Phase screen dimension	8192 pixels
Subaperture dimension	16 pixels

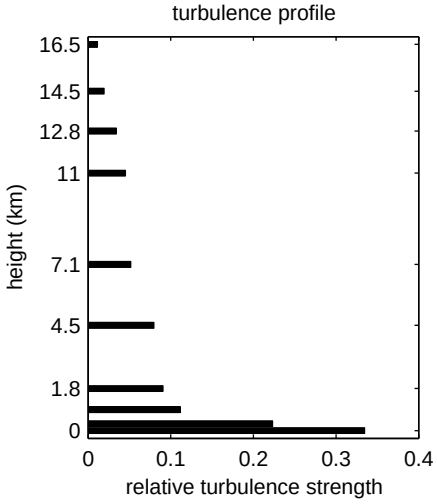

the performances of LSGs and NGSs (see Section 4.4.2). Thirdly, we estimate the GLAO performance at large telescopes (ELTs up to 32 meter) and study the impact of the subaperture size and the outer scale L_0 (see Section 4.4.3).

It can be pointed out that most of the Monte Carlo simulations were made using exactly the same assumptions as made for the analytic approach in Section 4.2. Only the WFS effects (noise and aliasing) and servo lag were modeled as additional error sources.

The tip-tilt indetermination problem was assumed to be totally absent in most cases. As it is later illustrated (Section 4.4.2), this makes our GLAO estimates slightly optimistic compared to reality. The cone effect of the LGSs is simulated by extrapolating the phase of each "slice" in the cone at given layer to the cylindrical area corresponding the size of telescope aperture.

The accomplished simulations are summarized in Table 4.2. In these simulations we studied several possible ways to position the guide stars. These different guide star patterns are shown in figure 4.4. The figure also illustrates the positions where we evaluated (in most cases) the PSFs in this study (5×5 grid in the first quadrant of the field). The asymmetric PSF grid was chosen to save simulation time — since the GS patterns are symmetric, the field evaluation is interesting only in one quadrant.

The GLAO performance is always evaluated by comparing the FWHM of the PSFs from GLAO corrected residuals and uncorrected atmospheric residuals. The uncorrected residuals are always obtained through numeric simulations and averaged over the field.

Table 4.2: The parameter configurations used in this study.

D^a	d^b	Guide stars	Pattern	Simulation
8 m	1 m	4, 8 LGS	I	optimum GLAO
8 m	1 m	8 LGS	II—III	another GLAO conf.
8, 32 m	1 m	4 LGS, 4 NGS	I	cone effect
8 m	1 m	4 LGS & 1,4 NGS	-	tip-tilt
8 m	1 m	4 LGS, 16 LGS	I	dim LGSs
8 m	1 m	4, 8 NGS	I[c]	asym. NGS brightness
4–32 m	0.5–2 m	4 LGS	I	subaperture size
4–32 m	1 m	4 LGS	I	telescope size
32 m	1 m	4, 8, 16 LGS	I	number of LGSs
32 m	1 m	4 LGS	I	effect of L_0

[a]Telescope diameter.
[b]Subaperture diameter.
[c]PSFs are evaluated over the whole field instead of the 1st quarter.

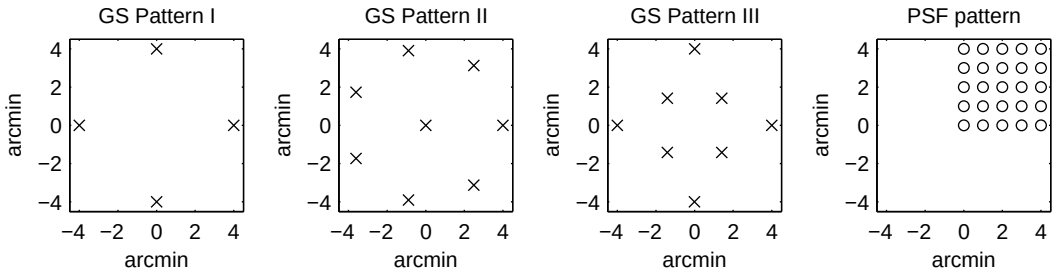

Figure 4.4: Positions of the guide stars (cross symbols) and the evaluated PSFs (circle symbols) in this study. Pattern I estimates the optimum filter (having the GSs evenly at the circle around the field). Pattern II has one GS at the field center. Pattern III has half of the stars moved inside the field.

4.4 Results

4.4.1 Comparison of analytic and numeric GLAO estimates

Simulation convergence

At first, the convergence behavior of our simulator is studied. To get reliable results in a reasonably short period of time, it is necessary to know the minimum values for at least two parameters: the number of required time steps and the dimension of the used phase screens. The former sets the time limit for simulations and the latter determines how much non-redundant turbulence information is stored in memory.

To get a first and quick approximation of the requirements we run the basic configuration (8 meter telescope with one meter subapertures and 4 LGS with pattern I) 10240 iterations. We monitored the long exposure FWHM as a function of iteration with two independent sets of phase screens. The results are shown in figure 4.5

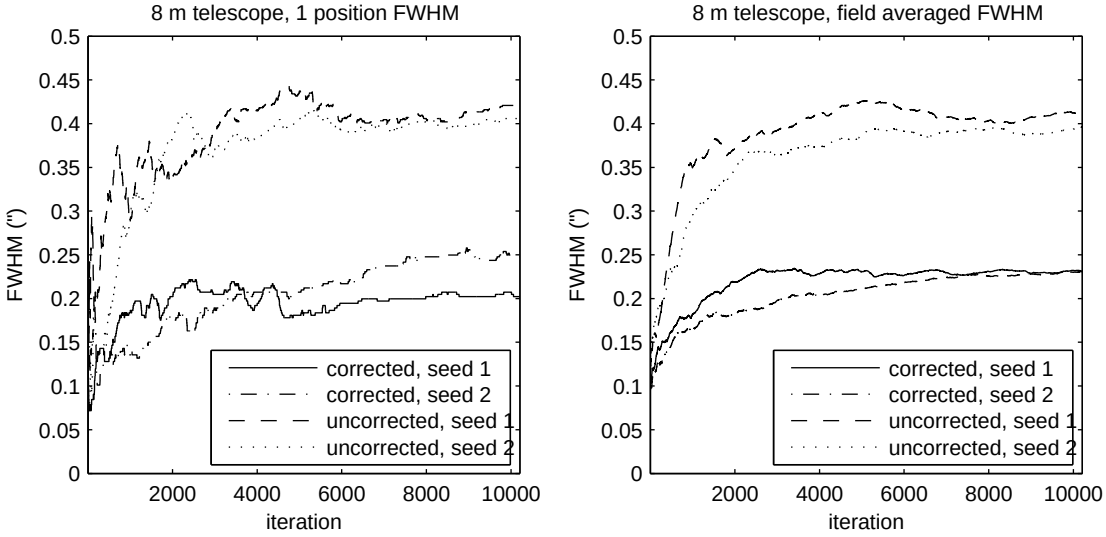

Figure 4.5: GLAO simulation convergence examples. Data are from a test with an 8 meter telescope, one meter subapertures, low noise, $\lambda_{\mathrm{img}} = 2.2$ μm and 4 LGSs (pattern I). Left: long exposure FWHM of a PSF at (0', 2'). Right: the averaged long exposure FWHM (25 PSFs as shown in figure 4.4) as a function of iteration. (Korkiakoski et al., 2006).

It can be seen that even after 10240 iterations the long exposure FWHM still has variations (of the order 0.05" while seeing is about 0.4") depending on the chosen random seed for the phase screen. However, the averaged FWHM is naturally significantly more stable.

Examples of the final PSFs are shown in figure 4.6. It can be seen that hardly any speckles are visible by eye in the PSF image (left). However, the contour plots are slightly fragmented instead of being perfect ellipses expected from analytic estimations — which is expected since the simulation did not fully converge as shown by figure 4.5. Nevertheless, the radial profiles of the simulated and analytic PSF

are very close to each other, differing only far from the field center. Thus, also the FWHMs of these two PSF estimates would be very close.

It is also notable that the PSF elongation with the chosen parameters is not very strong. Therefore, the spot elongation is not further analyzed in this study.

The shape of the GLAO corrected PSFs is very close to the pure seeing limited PSFs. This is characteristic of the large (4 arcmin) correction. When optimizing the correction to smaller fields, a diffraction peak occurs in the middle of the PSF (Le Louarn and Hubin, 2004; Le Louarn et al., 2005a).

As a conclusion, it can be said that our compromise for the accuracy parameters (iteration number 10240, phase screen size 8128) are leading to rather uniform simulation results. Some additional variance exists, but as the results will show later, the convergence is good enough.

Comparison to optimum filter

Next we demonstrate the difference between the analytical optimum filter and the multi-beacon filter (see equations (4.5) and (4.6)). We ran two simulations with an 8 meter telescope having one meter subapertures, and no significant noise was present.

First we used 4 and then 8 LGS at 90 km. They are located symmetrically at a circle (radius of 4') around the field center. This is the optimal way to locate the guide stars to reach a correction closest to that is provided by the optimum filter. In the following it is called an optimum filter approximation.

We computed the PSFs at 25 points in the first quadrant as shown left in figure 4.4. The PSF computation was done using three methods: simulation, analytically with the optimum filter and analytically with the multi-beacon filter. The results are shown in figure 4.7.

It is immediately seen that the results from simulations match rather well the analytic computations. The drop in FWHM at 4' in the left plot is because the LGSs at (0', 4') and (4', 0') are giving a better correction at these points. The simulation FWHM has, however, quite noticeable additional variations unlike the analytic estimate. This is mostly — as explained before — the result of limited simulation time rather than a real non-uniformity issue. It can be also seen that the average FWHM of the simulation PSFs is almost the same as the analytically anticipated one. This average is only about 0.01–0.02" worse compared to the FWHM given by the optimum filter.

From the analytic profile plots in figure 4.7 it can also be seen that already four LGS are enough to obtain a rather uniform correction within the area 4' from the field center. When using 8 LGS, the correction is almost the same as the optimum. If four LGSs (instead of eight) are used, the total FWHM increases about 0.02".

Figure 4.8 shows the averaged FWHM (and FWHM variance) as a function of the number of LGSs. The LGS pattern I (approximating the optimum filter) is used — only one particular case for 4 LGS with patterns II and III is shown. The simulations were made with two telescopes (8 and 32 meter) and one meter subapertures are used.

It can be seen that the average FWHM stays almost the same even if more LGSs are added. The 32 meter telescope gains slightly more from the additional

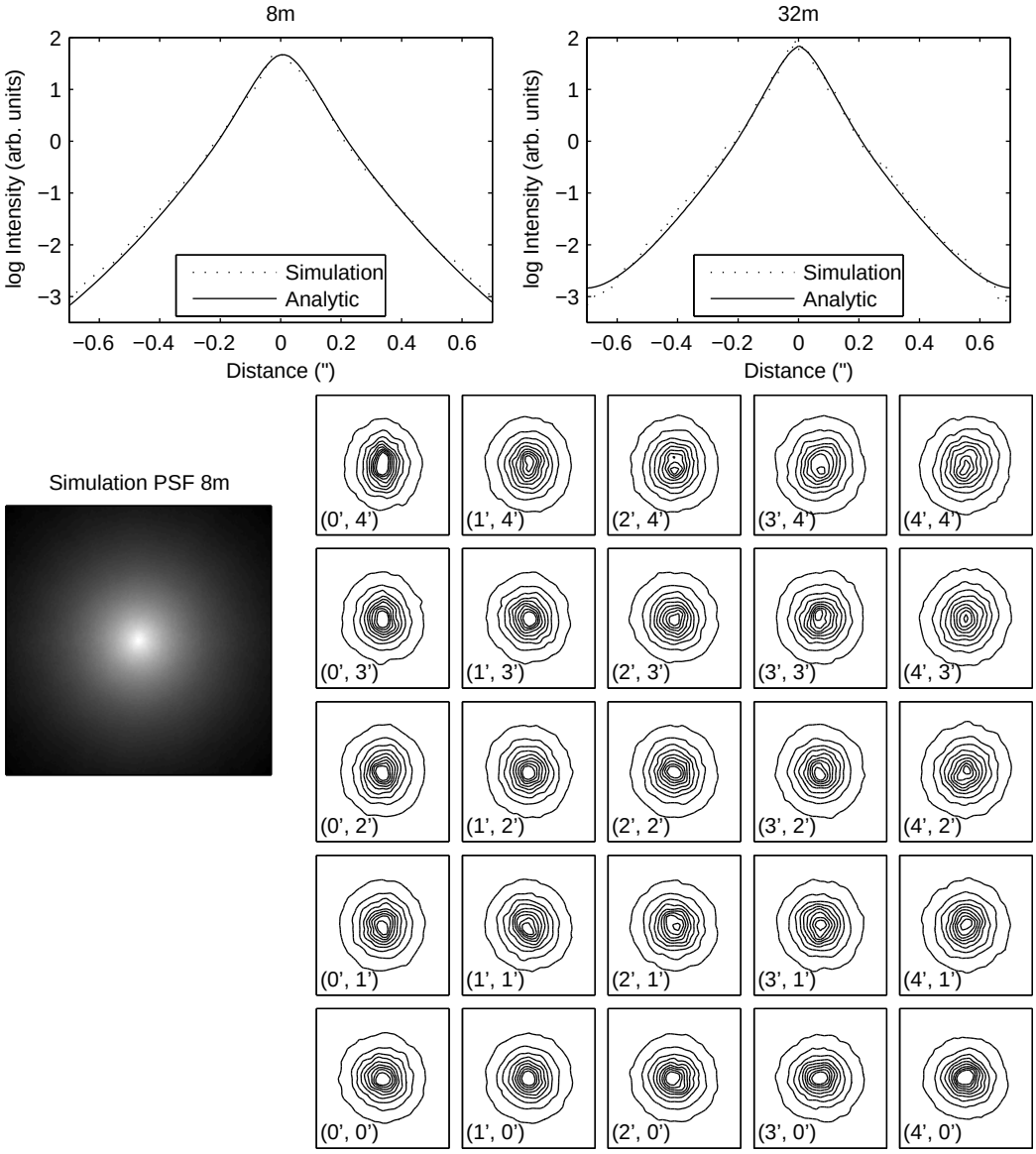

Figure 4.6: Examples of long exposure (10240 iterations) PSFs from GLAO simulations. We used an 8 meter telescope (and 32 meter in one case), one meter subapertures, low noise, $\lambda_{\mathrm{img}} = 2.2$ μm and 4 LGSs (pattern I). Upper row: Radial profiles of the simulated and analytically estimated on-axis PSF. Lower left: An image of an on-axis PSF (image width is 5.6"). Lower right: PSF contours, located as shown in figure 4.4 for pattern I. The width of each box is 1" and numbers in the boxes show the PSF center location. (Korkiakoski et al., 2006).

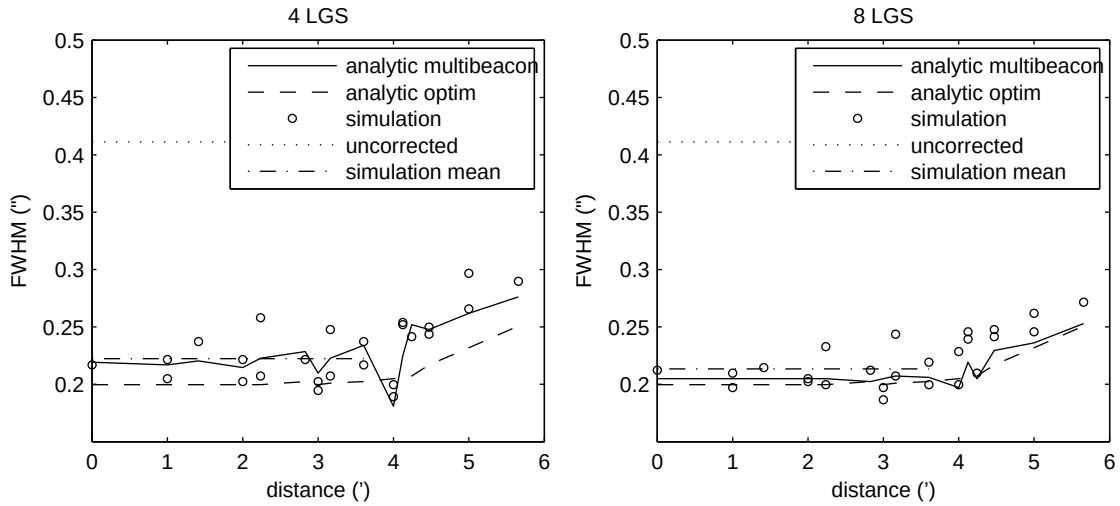

Figure 4.7: FWHM analytically computed and simulated for an 8 meter telescope having one meter subapertures. Imaging wavelength is $\lambda_{\mathrm{img}} = 2.2$ μm. FWHM is plotted as a function of distance from the field center. Mean of numeric results is from PSFs inside corrected area (4'). Left: 4 LGS used. Right: 8 LGS used. (Korkiakoski et al., 2006).

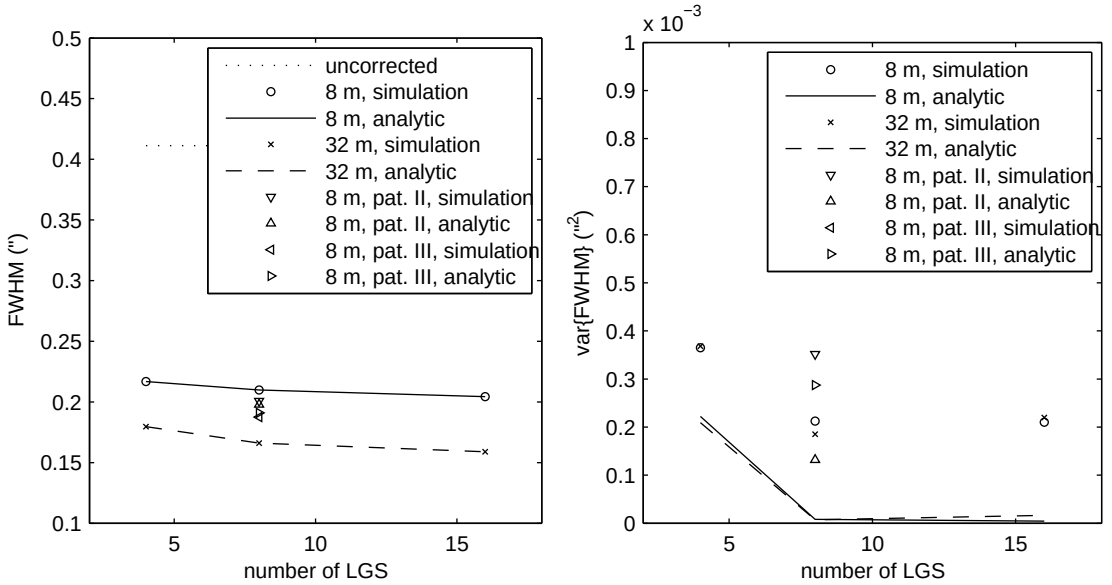

Figure 4.8: Effect of the LGS number. Simulations are made with an 8 and 32 m telescope having one meter subapertures, $\lambda_{\mathrm{img}} = 2.2$ μm and LGS pattern approximating the optimum filter. PSFs are evaluated as shown in figure 4.4 — except only the PSFs inside the 4' circle are used. The triangles show the variance when LGS pattern II and III were used (see Section 4.4.1). Left: averaged FWHM. Right: FWHM variance. (Korkiakoski et al., 2006).

LGSs. However, the variance of FWHM is significantly reduced when using 8 LGSs instead of 4 LGSs. Using 16 instead of 8 LGSs does not essentially improve either average FWHM or the correction uniformity. On the contrary, the FWHM variance (estimated from simulations) is even slightly bigger compared to the 8 LGS case (which is a simulation artifact).

Analytic and simulation results for the averaged FWHM agree completely. The FWHM variance however, is notably bigger for the simulated FWHM. The difference in FWHM variance can be explained by the simulation errors such as discussed before. As can be seen, the simulation inaccuracies create additional variance, but the general shape of the variance plots is similar to the analytic ones.

Thus, it can be concluded that at the investigated range (4–16) the number of LGSs is not a significant factor for the GLAO system performance. Having more than 8 LGSs did not essentially improve the results in any studied case.

Simulations with different LGS patterns

It was then further studied how changing the LGS pattern affects the uniformity of the correction. The effect of two LGS pattern (shown in figure 4.4) having distributions differing from the optimum filter approximation was tested. Using these patterns we made the same simulations (and analytic computations) as shown in figure 4.7 for the default LGS configuration (8 meter telescope, one meter subapertures). The results of these tests are also shown in figure 4.9.

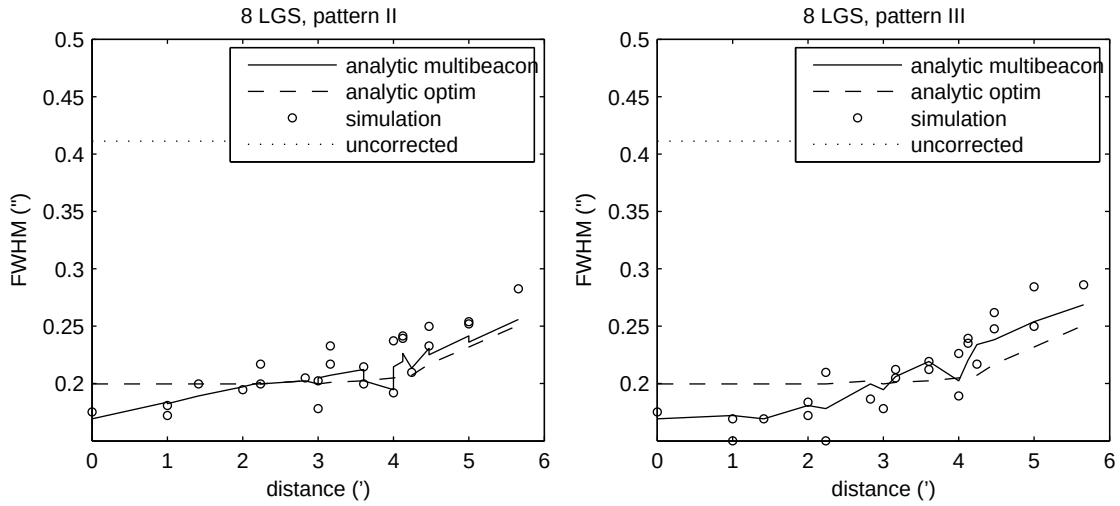

Figure 4.9: FWHM computed analytically and simulated for "non-standard" LGS patterns (II and III as shown in figure 4.4) (with an 8 meter telescope having one meter subapertures and $\lambda_{\mathrm{img}} = 2.2$ μm). The results are represented similarly as in figure 4.7. (Korkiakoski et al., 2006).

It can be seen that the correction is slightly less uniform compared to the LGS patterns approximating the optimum filter. If more than one LGSs are moved from the ring towards the field center (as in the pattern III), the correction uniformity

suffers more. This is observable both from the analytic computations and the simulation results.

The average and variance of the FWHM are shown in figure 4.8 with the triangle symbols. It can be seen that the average FWHM is slightly smaller compared to the pattern I with 8 LGSs (as more weight is put to the correction in the direction of zenith), but correction uniformity is worse. However, the uniformity when using pattern II is still better compared to the 4 LGS case and pattern III is only slightly worse than the 4 LGS case.

Thus, it can be concluded that the LGS pattern is not a major concern in GLAO. As long as the guide stars are rather symmetrically located around the field of interest, good and uniform correction is obtained.

4.4.2 Examples of noisy GLAO cases

Simulations with different photon noises

In this section we show the simulations we made to investigate the effect of WFS noise on GLAO. At first, we have made a test to study the general flux requirements for a standard LGS configuration (symmetric LGS brightness). Then, we have made some simulations to find out how the flux asymmetries affect the correction uniformity.

We made simulations with an 8 meter telescope having one meter subapertures. We used the pattern I shown in figure 4.4 having first 4 LGS and then 16 LGS. The photon flux from each star was varied between 2 and 200 photons per subaperture per frame. We also ran the simulations with two different controller parameters. The loop gain was first 0.2 and then 0.4. The results are shown in figure 4.10.

It can be seen that with the high flux the integrator gain does not affect the FWHM. Simulation gives always almost the same average FWHM compared to the analytic result. This is exactly as observed from the earlier simulations.

It is also seen that the flux can be very low until a significant loss in the performance is seen. Even with 50 photons per subaperture per frame (corresponds to a 12 magnitude star as explained in appendix C) the increase in FWHM is only about 0.01". With 10 photons (magnitude 13) the FWHM increase is 0.2"–0.04" and even with 5 photons (magnitude 16) noticeable correction can be made.

The controller optimization becomes necessary only at fluxes getting down to about 10 photons per frame. It can be seen that in those cases the correct choice of the loop gain (0.2 instead of 0.4) can improve the FWHM roughly 0.05". However, we considered only static loop gains — a modal approach would perhaps be more beneficial.

Nevertheless, the observed return flux of already implemented sodium LGS systems is about 50–150 photons/cm^2/s (Wizinowich et al., 2006) giving over 1000 photons per subaperture per frame (when scaled to the used configuration). This means that urgent consideration of more advanced controllers for the GLAO systems is probably not necessary. In the future, cheaper lasers could be considered, in which case such optimization could be useful.

It is also seen that the correction uniformity does not suffer from the dim guide stars. Figure 4.10 shows that the FWHM variance remains almost the same as the

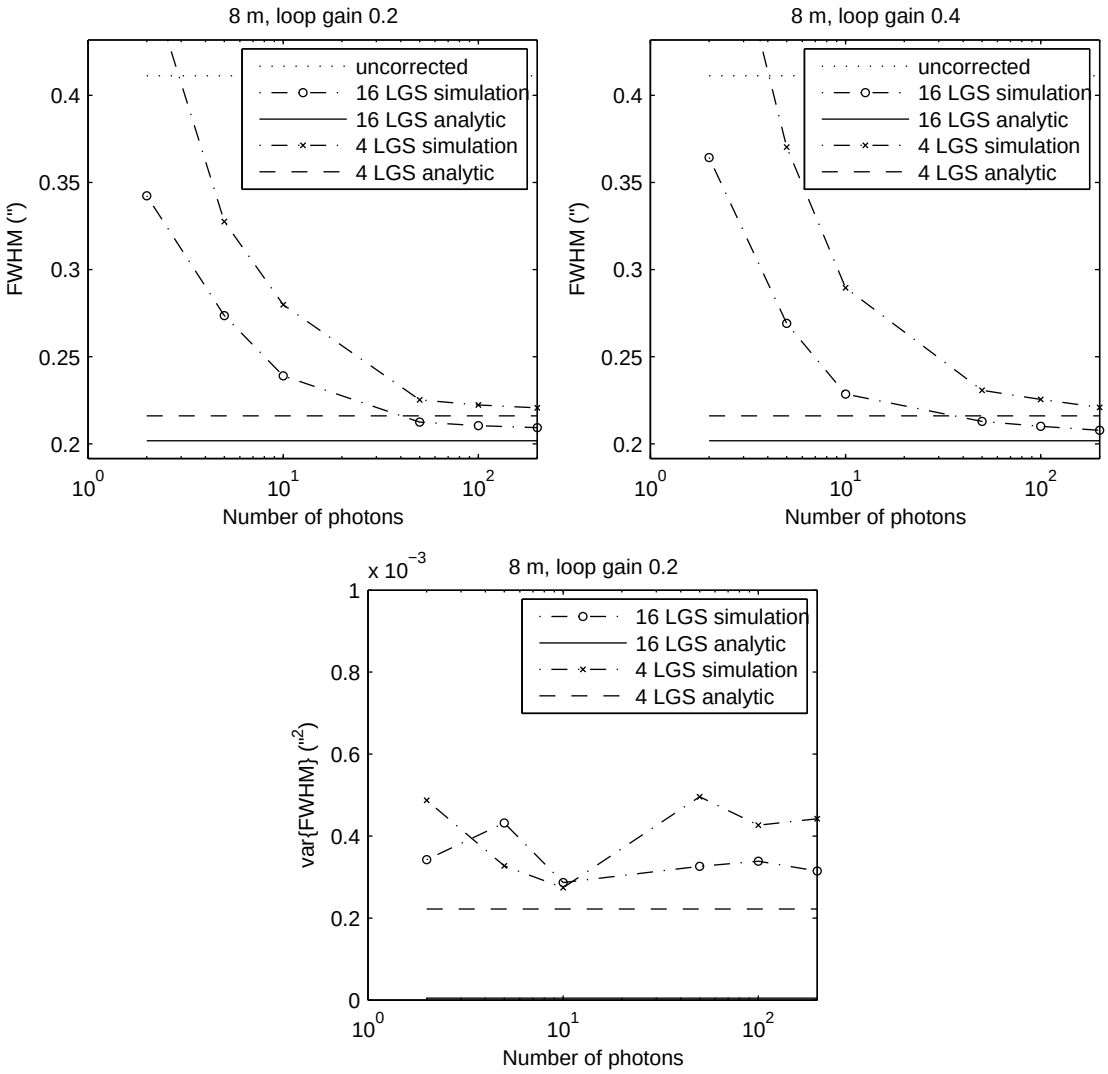

Figure 4.10: Average FWHM (and its variance) as a function of LGS flux (2, 5, 10, 50, 100 and 200 photons per subaperture per frame are used). The flux is given in terms of photons per subaperture per frame. The average is over the PSFs inside the 4' circle in the first quarter. Simulations are made with an 8 meter telescope having one meter subapertures, $\lambda_{\mathrm{img}} = 2.2$ μm and the used LGS patterns had the stars symmetrically at the circle around the 4' field. Upper left: results with loop gain 0.2. Upper right: results with loop gain 0.4. Down: variance is shown for loop gain 0.2. (Korkiakoski et al., 2006).

photon number is changed. Thus, the low fluxes from the guide stars only reduce the resolution, but do not decrease the correction uniformity.

Issues with LGS compared to NGS

We have also tested the difference between natural and laser guide stars (the cone effect and the tip-tilt problem of LGSs).

To illustrate the cone effect we ran two simulations for 4 meter and 32 meter telescopes with one meter subapertures. We used first 4 LGSs (as before) and then 4 NGSs. The resulting FWHM profiles are shown in figure 4.11. The test is rather academic since no such patterns of natural guide stars exist in the sky.

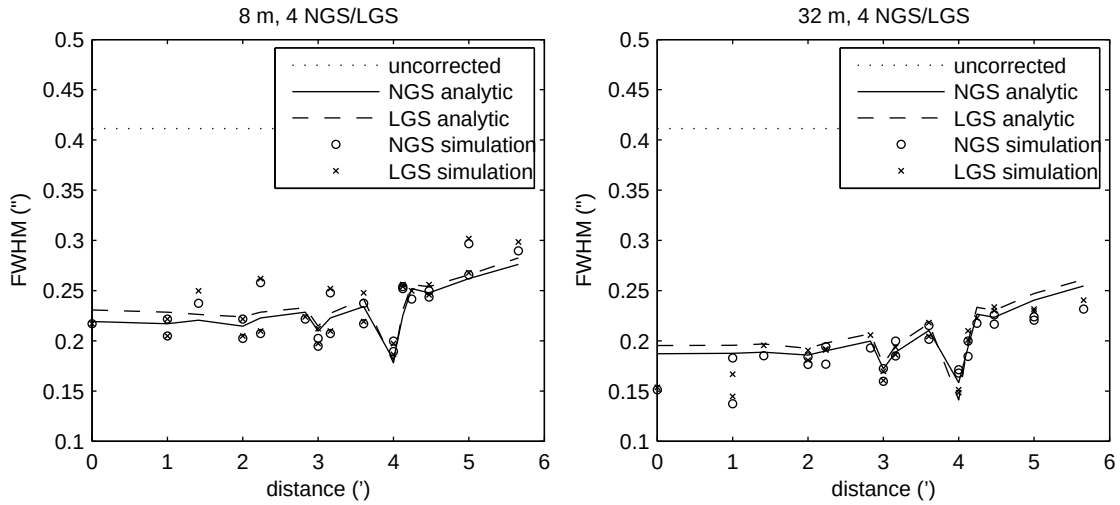

Figure 4.11: FWHM from a simulation with NGSs compared to corresponding simulation with LGSs at 90 km. Here are used 4 LGSs/NGSs, one meter subapertures, $\lambda_{\mathrm{img}} = 2.2$ μm and no significant noise. Left: an 8 meter telescope. Right: a 32 meter telescope. (Korkiakoski et al., 2006).

However, it can be seen that the cone effect has no practical influence on the performance of GLAO — at least with the LGSs as high as 90 km. The analytic profiles are almost identical (as already known (Tokovinin, 2004)) and the simulation results totally confirm this.

Next we show how much the results change if the tip-tilt is removed from the LGSs. We run two simulations with 4 LGSs as in pattern I in figure 4.4, but removed the tip-tilt signal from those stars. In the first case we had one tip-tilt NGS at on-axis, and in the second case we had four tip-tilt NGSs at (0', 2'), (0', -2'), (2', 0') and (-2', 0). The FWHM profiles of those simulations are shown in figure 4.12.

It can be seen that removing the tip-tilt signal from LGSs indeed deteriorates the GLAO performance a bit. The average FWHM stays about the same, but the correction uniformity suffers more — when one tip-tilt star is used, the results are somewhat worse than the pattern III (having 8 LGSs) is giving in similar conditions. Adding more tip-tilt stars essentially helps the problem.

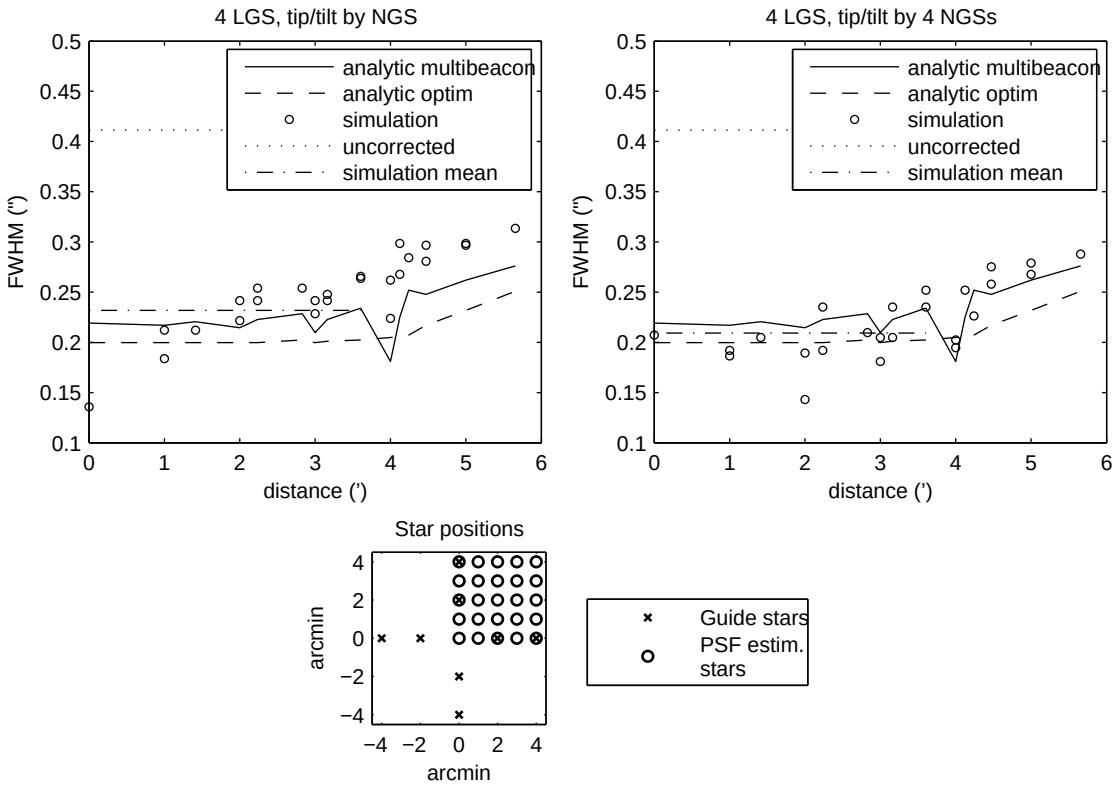

Figure 4.12: FWHM profiles from simulations with the tip-tilt signal removed from LGSs and observed separately by one or four NGSs. We used an 8 meter telescope having one meter subapertures, $\lambda_{\mathrm{img}} = 2.2\ \mu$m and no significant noise. The analytic estimate is made as before in figures 4.7 and 4.11. Left: the tip-tilt star is on-axis. Right: the resulting FWHM profile. Bottom: the locations of the GSs (inner GSs are the tip-tilt stars). (Korkiakoski et al., 2006)

Then we have also demonstrated how the FWHM depends on the brightness of the tip-tilt star. We used the configuration shown left in figure 4.12 (4 LGSs, one on-axis NGS) and varied the flux from the tip-tilt star. The results are shown in figure 4.13.

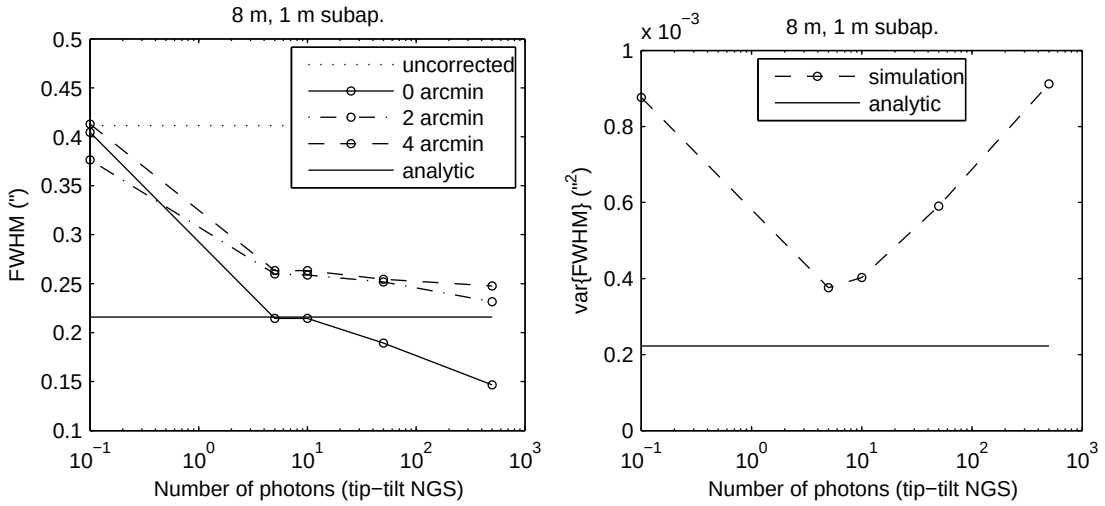

Figure 4.13: Effects of tip-tilt star brightness. The simulations are made with 4 LGSs (tip-tilt signal removed) and one on-axis NGS (8 meter telescope having one meter subapertures and $\lambda_{\text{img}} = 2.2$ μm). The analytic estimates are the same as in figures 4.7, 4.11 and 4.12. The tip-tilt star brightness is defined as photons per area of 8×8 m^2 per frame (at 500 Hz). The brightness of zero is shown as 10^{-1} to enable logarithmic plots. Left: FWHM average at different distances from the field center as a function of the tip-tilt star brightness. The analytic plot is averaged from all evaluated PSFs inside the 4' field. Right: FWHM variance (inside the 4' field) as a function of the tip-tilt star brightness.

It can be seen that if no tip-tilt star is used, the GLAO does no FWHM correction at all. Adding more photons, however, helps rapidly. Even 5 photons per 64 m^2 per frame at 500 Hz (corresponding to a 20 magnitude star) are enough to obtain almost the best possible FWHM (the sky background was neglected). At fluxes over 50 photons the on-axis PSF gets a FWHM better than the analytic averaged FWHM (as also seen in figure 4.12).

The brighter tip-tilt stars help to improve the average resolution, but also decrease the correction uniformity as the resolution in the field center increases faster. It even seems that an optimum brightness for the tip-tilt star exists, if the correction uniformity is important. In such case, a better controller needs to be designed to balance the effect of the tip-tilt star.

To summarize, the tip-tilt removal should not be totally neglected when estimating the GLAO performance. This section visualizes the errors our subsequent GLAO estimations are likely to contain.

Simulations with pure NGSs

Next we test how the results are affected if GLAO is made with only NGSs having asymmetric photon fluxes. We made simulations with an 8 meter telescope and one meter subapertures and two variations of pattern I shown in figure 4.4.

The optimum filter is approximated with 4 and 8 NGSs having the asymmetries shown in figure 4.14. The two first cases have one bright (200 photons per subaperture per frame) star at (4', 0') and the other (4 or 8) NGSs send much less photons (5 photons per subaperture per frame). The corresponding stellar magnitudes are 10 and 16. The last case has 4 bright NGSs over one half-plane, but the other NGSs are dim. Figure 4.14 shows the FWHM surfaces over the field and corresponding profiles projected to one dimension.

It can be seen that the photon ratio 5/200 clearly distorts the correction uniformity. In the two first asymmetries the correction is notably better near the bright NGSs. In the last case the whole half-plane with brighter NGSs is having better correction.

Then we have also taken the first and last asymmetry case and increased the flux of the dim NGSs from 5 to 100 photons (corresponding stellar magnitudes 16 to 12). The FWHM average and variance (over the PSFs inside the 4' circle) are plotted as a function of the brightness of the dim NGSs. The results are shown in figure 4.15).

It can be seen that the increase of the flux rapidly corrects the problems of anisoplanatism. As soon as each dim NGS is sending 50 photons/subaperture/frame (magnitude 12), the average FWHM almost reaches the optimum level. The correction uniformity, however, is much more problematic. When figure 4.15 is compared to figure 4.8, it is seen that a photon ratio of 50/200 gives about the same performance as the LGS pattern III. To reach the level of uniformity given by pattern I, a ratio of 100/200 photons is needed.

In addition, it can be pointed out that the different asymmetries I and III behave very similarly, with respect to the performance in terms of FWHM. The absolute difference between the plots is due to the different number of LGSs.

As a conclusion, it can be said that GLAO performance — in terms of FWHM variance over the corrected field — is somewhat sensitive to the variations in NGS intensities. As long as most of the NGSs remain bright enough (more than 50 photons/subaperture/frame — or magnitude less than 12), a good and uniform correction is maintained. However, if both bright and dim stars are present (magnitudes less than 12 and more than 13), more emphasis has to be placed on the control optimization.

4.4.3 Effect of the subaperture size, telescope diameter, and outer scale

In this section we show how GLAO performance is affected by the telescope diameter and subaperture size. We keep the parameters shown in Table 4.1 the same and test telescope diameters between 4 to 32 meters. Without the correction, the FWHM remains the same in all the tests, having a value of about 0.40–0.41". We simulate here only LGSs having high fluxes and the tip-tilt determination problem neglected.

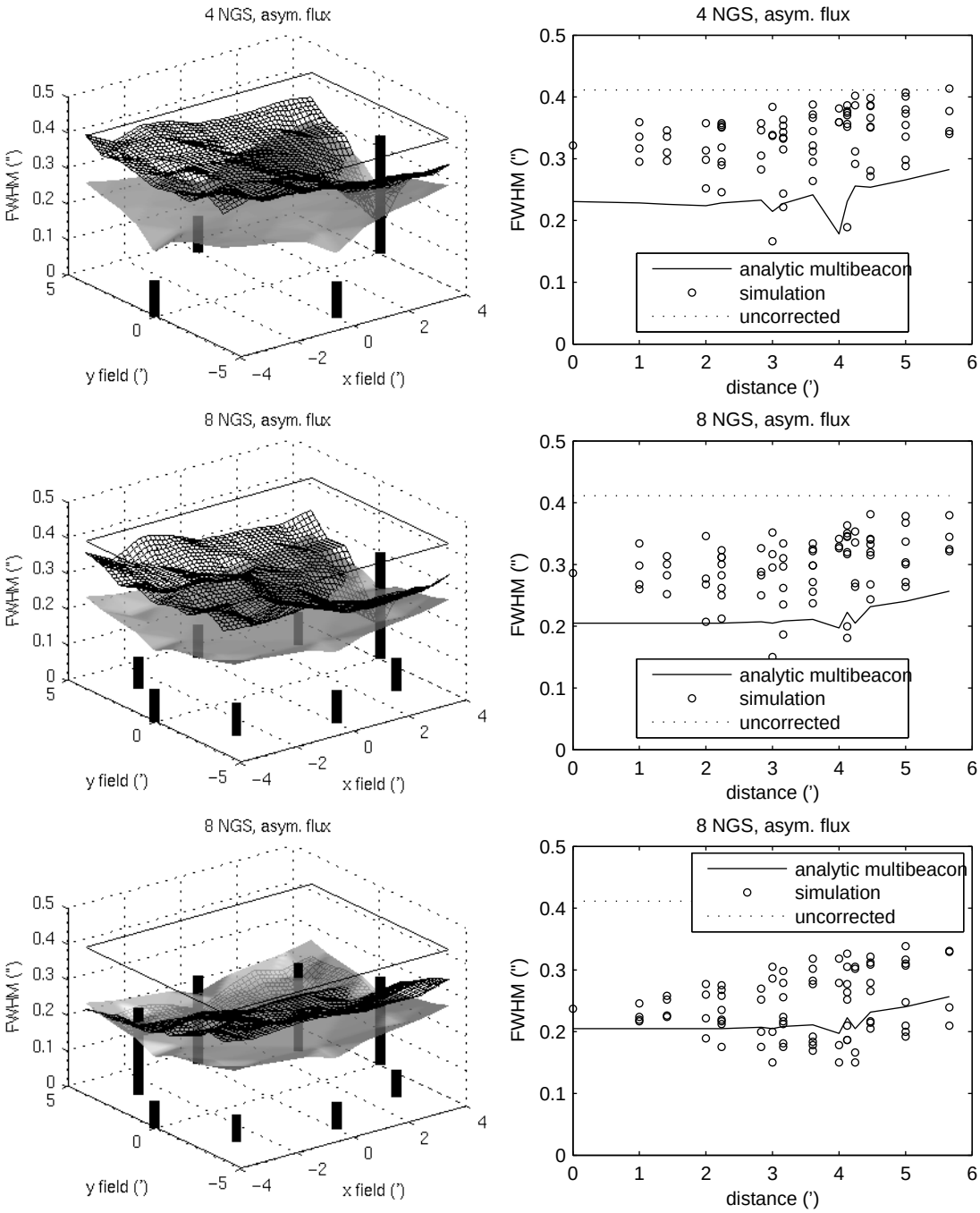

Figure 4.14: FWHM from simulations with asymmetric photon fluxes from the NGSs. The simulations were done with an 8 meter telescope having 1 meter subapertures, $\lambda_{\mathrm{img}} = 2.2$ μm and stars located as in the pattern I in figure 4.4. Upper and middle: NGS at (4',0) has 200 photons/subaperture/frame, other NGSs have 5 photons. (Referred as asym. I and II.) Lower: NGSs in "upper" half plane (shown by high vertical lines) have 200 photons, others have 5 photons. (Referred as asym. III.) (Korkiakoski et al., 2006).

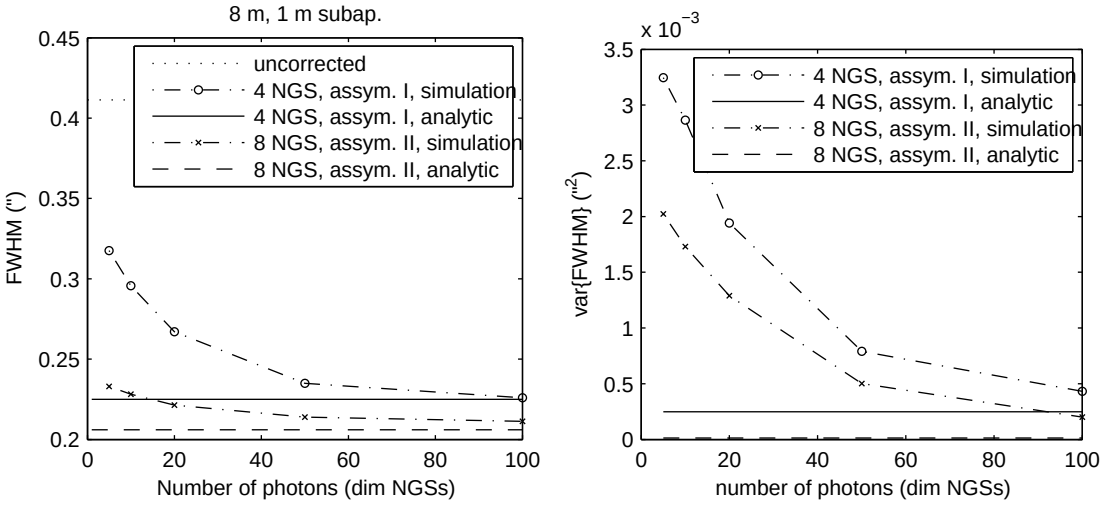

Figure 4.15: Average and variance (over the PSFs inside the 4' circle as seen in figure 4.14) of FWHM as a function of photon number per subaperture per frame. The photon number tells the flux from the dim stars, the bright stars have the same flux of 200 photons/subaperture/frame. The simulations are from the same systems as shown in figure 4.14 (asym. I and III). (Korkiakoski et al., 2006).

At first we chose three telescopes (4, 8 and 32 meter) and tested how the FWHM varies as a function of the subaperture size. Those results are shown left in figure 4.16. It can be seen that when using the four meter telescope, the FWHM is almost independent of the subaperture size. However, when the subaperture size grows over one meter, FWHM starts to slowly increase. Thus, it can be concluded that for seeing conditions shown in Table 4.1 the optimum subaperture size is one meter.

Then we have kept the subaperture size constant at one meter and varied the telescope size. We measured the FWHM from the same points as before and averaged the points having the same distance to the field center. Those results are shown right in figure 4.16.

It can be seen that a significant resolution improvement can be achieved when increasing the telescope diameter from 4 meter to 8 or 16 meter. Roughly speaking, FWHM is reduced from 0.25" to 0.20". However, after this, the larger telescopes do not improve the resolution significantly. To obtain a FWHM under 0.20" the diameter must be increased to 32 meter.

Nevertheless, as a conclusion it can be said that the optimum resolution with GLAO is easily available with low order systems. When using the 8 meter telescope with one meter subapertures, we control only 46 modes. Correspondingly the 16 meter telescope has 160 controllable modes. A significant resolution improvement for a GLAO system is not achieved by increasing the telescope size further than 16 meter.

With the bigger telescopes the outer scale L_0 has a significant effect on the performance. Therefore, we investigated the effect of L_0 with a 32 meter telescope. All the previous simulations are made with $L_0 = 25$ m, as shown in Table 4.1. To find out what a bigger L_0 would do, we made a simulation with L_0 set to 50 m.

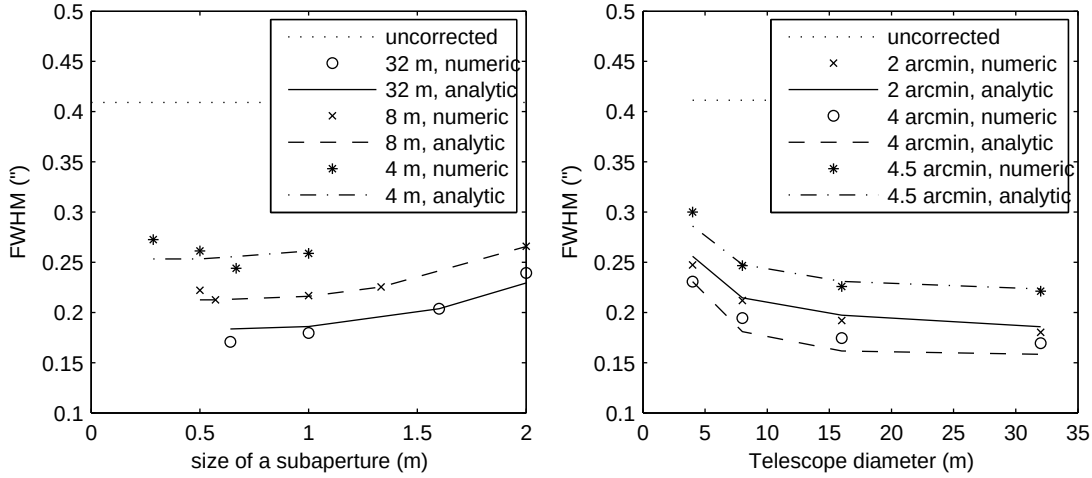

Figure 4.16: Left: FWHM (and seeing level) as a function of subaperture width. Three telescopes (4 m, 8 m and 32 m) are used with 4 LGSs as pattern I in figure 4.4. Imaging wavelength is $\lambda_{\text{img}} = 2.2$ μm. The FWHM average is computed from the PSFs inside the 4' circle. Right: FWHM (and seeing level) at three distances from the field center as a function of telescope diameter. Subaperture size was kept at one meter. Each FWHM is an average over the two matching PSF position shown in the grid in figure 4.4. (Korkiakoski et al., 2006).

It was found out that both the analytic estimates and the simulations predict the effect of L_0 in the same way. When increasing the L_0 from 25 m to 50 m, both seeing and GLAO FWHM experience an increase of about 0.05". This is illustrated left in figure 4.17.

The right plot in figure 4.17 shows the average FWHM as a function of L_0. It can be seen that the FWHM of both the uncorrected and GLAO corrected PSFs increase about 0.05" as L_0 increases from 25 to 50 meters.

4.5 Conclusions of GLAO simulations

In general, it can be noted that the performance estimates of the analytic results and the numeric simulations are in excellent agreement. This is consistent with the extensive study by (Andersen et al., 2006b).

However, as we neglected the tip-tilt indetermination effect, the results must be considered slightly too optimistic. With an 8 meter telescope one NGS is enough to eliminate the problems caused by the tip-tilt indetermination — deviations from the average FWHM are only 5–10%. If better uniformity is required, a few additional tip-tilt stars can be used to slightly decrease the deviations.

It is obvious that the GLAO systems are very robust. When the simulations are made without noise and many LGSs, even the simplest controller gives results almost equal to the optimum performance. This happens rather well even with LGS patterns significantly different from the optimal pattern (LGSs evenly at the circle around the field of interest).

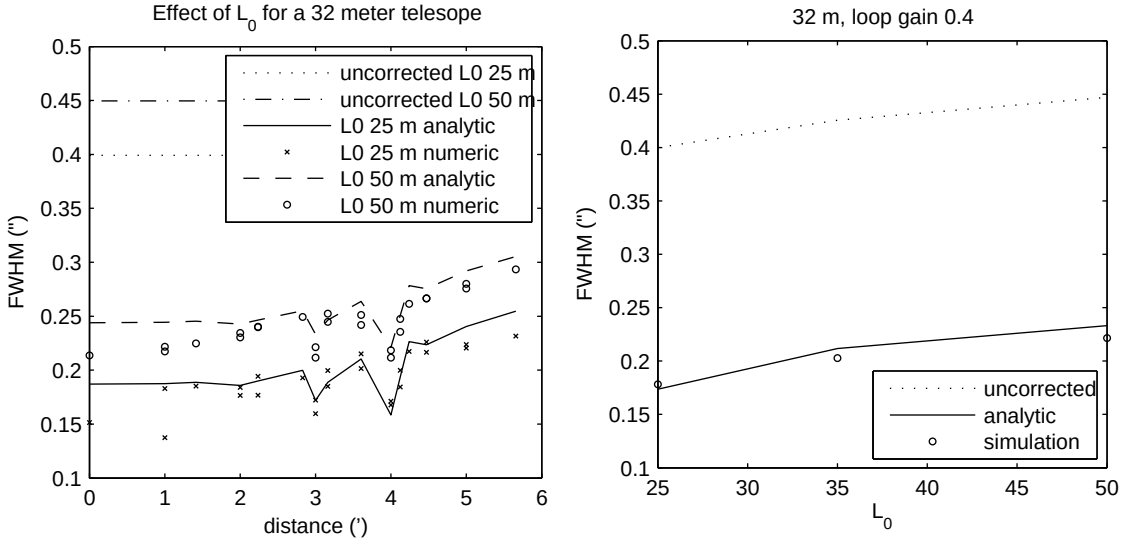

Figure 4.17: Right: FWHM (and seeing levels) as a function of distance from FOV center. The simulations are made with a 32 meter telescope having one meter subapertures and $\lambda_{\mathrm{img}} = 2.2$ μm. Two different values for L_0 are tested. Left: average FWHM as a function of L_0. The simulations are made with the same 32 m telescope.

In addition, the photon noise has to be high before the GLAO performance gets distorted. Our simulations (with an 8 meter telescope, one meter subapertures) indicate that a magnitude 12 LGS is bright enough for almost optimum correction. The magnitudes must be as high as 16 to significantly increase the GLAO corrected FWHM. Even with 2 photons (corresponding to stellar magnitude 17) the GLAO system having 8 LGSs is able to give a correction of 0.05" (almost 15% better resolution). The brightness requirements for the tip-tilt star are even less demanding — a magnitude 20 star produces sufficiently photons for good tip-tilt determination.

The asymmetric brightness of the guide stars (NGSs) might be an issue, although not a dramatic one. The flux ratios between dim and bright NGSs need to be around 20/200 (corresponding to stellar magnitudes 14 and 12) in order to cause substantial FWHM distortions.

In practice, when laser guide stars are used, such extreme conditions seem rather unrealistic. Even the current systems are able to maintain powerful enough LGSs on sky (Wizinowich et al., 2006). Nevertheless, if extremely dim guide stars are to be used, the simulations done here suggest that more advanced control algorithms might be useful to maintain the correction homogeneity. The possibilities of such control strategies are discussed for instance in (Nicolle et al., 2006).

Similar conclusions, concerning the GLAO control, have been reported also by a few other authors. For instance, (Stoesz, 2006) has shown that VWGLAO system with optimal actuator and subaperture pitch will not be affected by servo lag and wavefront sensor noise.

Besides of the robustness issue, we have demonstrated that for a successful GLAO system in the near infrared it is necessary to correct only the low order modes.

For the seeing conditions we used, a coarse one meter subaperture size seems to be enough. However, for shorter wavelengths like in MUSE, a greater number of degrees of freedom is needed (Le Louarn et al., 2005a).

It has also been shown that the resolution of a GLAO system is not endlessly improved by large telescopes and 8 LGSs are sufficient for the telescopes having a size up to 32 meters. VLTs have over 30% better resolution compared to smaller 2–4 meter telescopes, but ELTs will have only about 5% better resolution compared to VLTs in GLAO over an 8' field of view (FOV).

Nevertheless, building efficient GLAO instruments for the ELTs is still useful. First of all, they will still improve the FWHM by a factor of 2 compared to the seeing limited case. In addition, such instruments will be able to correct also the aberrations originating form the telescope (wind induced vibrations, errors due to temperature changes and so on).

Chapter 5

Optimization of the control of the pyramid sensor for extreme AO

This chapter is devoted to the adaptive optics reconstruction and control issues with the pyramid wavefront sensor. The aim is to seek optimal control methods feasible for the P-WFS in all seeing conditions. We study here a typical 8 meter telescope with a 40×40 measurement resolution XAO system.

The XAO system of the SPHERE instrument for the VLT (Beuzit et al., 2006) is based on a spatially filtered SH (Poyneer and Macintosh, 2004). Even though the pyramid sensor was seriously considered in SPHERE conceptual design, it was considered too risky at this time, especially because of the control issues. The current baseline of EPICS, the Planet Finder instrument concept for the E-ELT, is based on the pyramid sensor and thus fully justifies that the problem of nonlinearities is considered here.

Since the nonlinearity problems are most prominent without modulation, we concentrate here mainly on the nonmodulated P-WFS. However, with some extensions, the methods presented here should apply as well to the modulated sensor.

At first, in Section 5.1, a short glance is given to the P-WFS and its problems with large phase variations. Then, in Section 5.2, a theoretical approach — published in (Korkiakoski et al., 2007b) — is taken to solve these problems. We were guided by the idea of compensating the nonlinearities as well as possible. This leads to a model-based reconstruction, radically different to the conventional approach discussed in Section 3.2.

The simulation results of the model-based reconstruction (referred as Jacobian reconstruction, JR) are represented in Section 5.3. We made a set of end-to-end closed-loop AO simulations to test how much the JR can decrease the residual phase variance. Then we compared these to the case where the conventional matrix-vector-multiplication (MVM) is used. Both the classical four-sided P-WFS and a novel two-sided P-WFS (as described in Section 2.4.2) are considered in these simulations.

The results of the JR simulations indicate that the ultimate nonlinearity compensation is not necessary to achieve a satisfactory performance. However, the reconstruction must be designed correctly for each seeing level to reach the optimal performance.

This leads us to propose a modal sensitivity compensation algorithm (Korkiakoski et al., 2008) in Section 5.4. By using the novel algorithm, a wavefront recon-

struction process can take into account also the sensitivity reduction specific to the used WFS, as well as the observed seeing level. In addition, this is done so that the algorithm can be implemented in real-time AO applications. The performance of the algorithm is studied in AO simulations, and the results are illustrated in Section 5.5.

The final Section 5.6 shows our conclusions concerning the pyramid wavefront sensor control.

5.1 Properties of P-WFS

5.1.1 Pyramid sensor in more detail

As explained in Section 2.4.2, the pyramid sensor divides the incoming beam into four sub-beams as illustrated in figure 5.1. The resulting images of the sub-beams are then measured at the CCD detector.

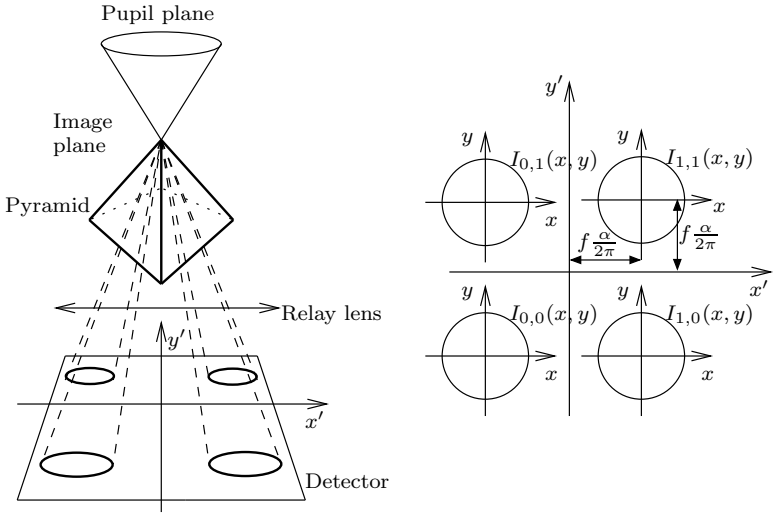

Figure 5.1: Illustration of the nonmodulated pyramid sensor and its signal composition. α is tangent of the pyramid divergence angle (Arcidiacono, 2005; Riccardi et al., 1998), f is the focal length and $f\alpha/(2\pi)$ is half of the distance between the sub-beam centers.

An example of the intensities at the CCD is shown in figure 5.2. It is seen that without any phase aberrations (or if the aberrations are very small), a significant proportion of the light is diffracted outside of the sub-pupils. This diffraction occurs also in the presence of larger phase distortions, although at a lower extent. This results in sub-beam interferences, and as will be seen later, it deteriorates the P-WFS performance if the four sub-pupils are imaged too close one another.

The pyramid sensor measurement is formed from the intensity patterns ($I_{0,0}(\mathbf{r})$, $I_{0,1}(\mathbf{r})$, $I_{1,0}(\mathbf{r})$, $I_{1,1}(\mathbf{r})$ as seen in figure 5.1) at each detector plane quadrant as

$$\begin{bmatrix} S_x(\mathbf{r}) \\ S_y(\mathbf{r}) \end{bmatrix} = \begin{bmatrix} \dfrac{I_{0,0}(\mathbf{r}) - I_{1,0}(\mathbf{r}) + I_{0,1}(\mathbf{r}) - I_{1,1}(\mathbf{r})}{I_t} \\ \dfrac{I_{0,0}(\mathbf{r}) - I_{0,1}(\mathbf{r}) + I_{1,0}(\mathbf{r}) - I_{1,1}(\mathbf{r})}{I_t} \end{bmatrix}, \tag{5.1}$$

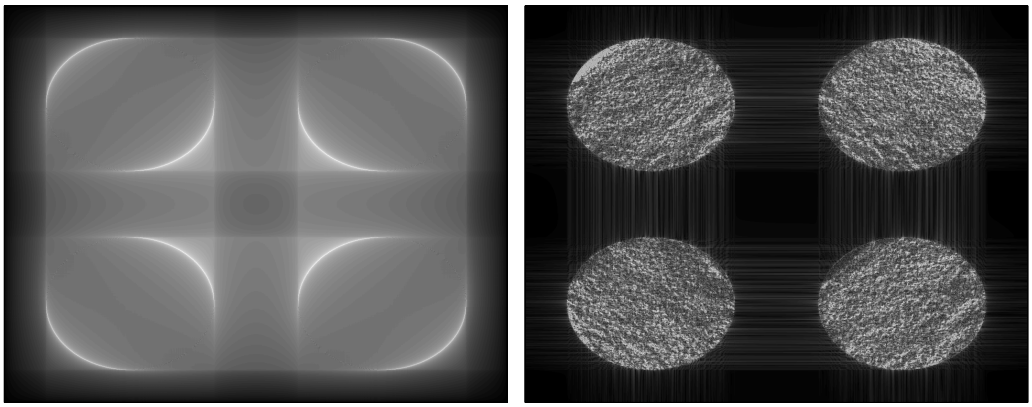

Figure 5.2: Illustration of P-WFS CCD intensities. The images are computed using a P-WFS model with a small pupil separation (center-to-center distance is 1.5 times the pupil diameter) and no modulation. Both images have a nonlinear scaling. Left: intensities of flat wavefront (reference measurement). Right: intensities of a typical closed-loop AO residual.

where I_t is the average intensity over the whole detector plane and $\mathbf{r} = [x\ y]^T$ is the location in the corresponding coordinate system. This signal composition (proposed in (Esposito and Riccardi, 2001; Vérinaud, 2004)) slightly differs from the original one presented in (Ragazzoni, 1996), where the normalization was done locally (instead of I_t). The normalization issue has later been discussed for instance in (Vérinaud et al., 2004), and the global approach has been shown more suitable for XAO applications, since it defines the signal as a linear function of the phase at weak perturbations.

Modeling a pyramid sensor

Modeling the P-WFS is a necessity to understanding its properties and designing the best possible sensors. The first models were based on geometrical optics calculations (Ragazzoni, 1996; Riccardi et al., 1998; Esposito and Riccardi, 2001). However, geometrical optics does not properly describe the peculiar diffraction effects of the sensor (Vérinaud, 2004). Thus, only wave models based on Fourier optics are considered in this thesis.

Essentially two wave-optics models have been developed to describe the performance of P-WFS. The first model neglects the interference effects between the sub-beams transmitted from the pyramid (an infinite pupil separation). The consequent analytic model is described in more detail in (Esposito and Riccardi, 2001) — each quadrant of the incoming phase is handled separately to compute the corresponding intensities at the CCD detector. In this thesis this case is referred as amplitude mask algorithm (AMA).

The second model takes into account the sub-beam interferences being more appropriate if the pupils are imaged near each other. The model, referred in this thesis as phase mask algorithm (PMA), is described in more detail in (Carbillet et al., 2005). The electric field at the P-WFS focal plane (at the tip of the pyramid prism) is multiplied by a single phase mask (as shown in appendix in equation (A.1)). Then

a Fourier transform and modulus is taken to obtain all the CCD detector intensities in a single image. The images in figure 5.2 are obtained using the PMA method.

Note that in this case, because of interferences, the signal for a null incoming wavefront is not zero and requires thus a reference measurement subtraction for an optimal wavefront reconstruction. Before using the signal shown by equation (5.1), the measurement of a flat wavefront is subtracted from it. Subtracting a reference measurement is usually also done to compensate non-common path errors in an AO system. In this thesis we always consider null non-common path errors. Some possible solutions to deal with issues in presence of non-common path errors are proposed for future work (see Section 6.1).

The AMA model can be realistic, if the sub-beams are imaged far away. Otherwise, the interferences should be taken into account. The simulation results in this thesis will show that the center-to-center pupil separation must be at least 3–5 times the pupil diameter for PMA and AMA to reach equally good closed-loop performances in all seeing conditions.

5.1.2 Problems with large phase variations

As explained in Section 2.4.2, the P-WFS has several advantages over the less sensitive SH-WFS. However, the limited dynamical range of the pyramid sensor causes problems in bad seeing conditions and at short sensing wavelengths.

For instance, the comparison of SH-WFS and P-WFS illustrated in figure 2.9 was done in conditions having a seeing of 0.85" (at 0.5 μm), sensing wavelength 0.7 μm and when a moderate modulation was applied. The Strehl ratio in those conditions was about 0.95 (at 2.2 μm). When turbulence is stronger, sensing wavelength shorter or less modulation is applied, the P-WFS is known to saturate. In bad seeing conditions, over one arcsec at 0.5 μm, this occurs even when the AO system is used in closed-loop.

An example, published in (Korkiakoski et al., 2007a), is shown in figure 5.3. The Strehl ratio is plotted as a function of the loop gain (simple integrator) for two sensing wavelengths. The conventional P-WFS reconstruction is compared with a linear sensor (described later in Section 5.3.1) and the case where an optimized amount of modulation is done during the calibration stage (when the interaction matrix is created).

It is seen that the conventional calibration works at the higher sensing wavelength 0.7 μm reaching a Strehl of 0.80 (at 1.6 μm) while the theoretical linear sensor would give a Strehl ratio of 0.85. At shorter sensing wavelength (0.5 μm), however, the Strehl of the conventional MVM drops to 0.60.

It is also seen that the bad performance of the nonmodulated P-WFS can be sidestepped to some extent, if modulation is applied at the calibration stage. By choosing an optimal amount of modulation (12 λ/D) at the 0.5 μm sensing, the Strehl ratio is significantly increased: from 0.60 to 0.74. However, at the higher sensing wavelength of 0.7 μm the optimal modulation (2 λ/D) does not have a big impact any more. It can be also mentioned that a similar helpful effect of the calibration modulation has been reported earlier by (Costa et al., 2003).

The reason for the bad performance at short sensing wavelengths or bad seeing is that the wavefront perturbations of high spatial frequencies present in the

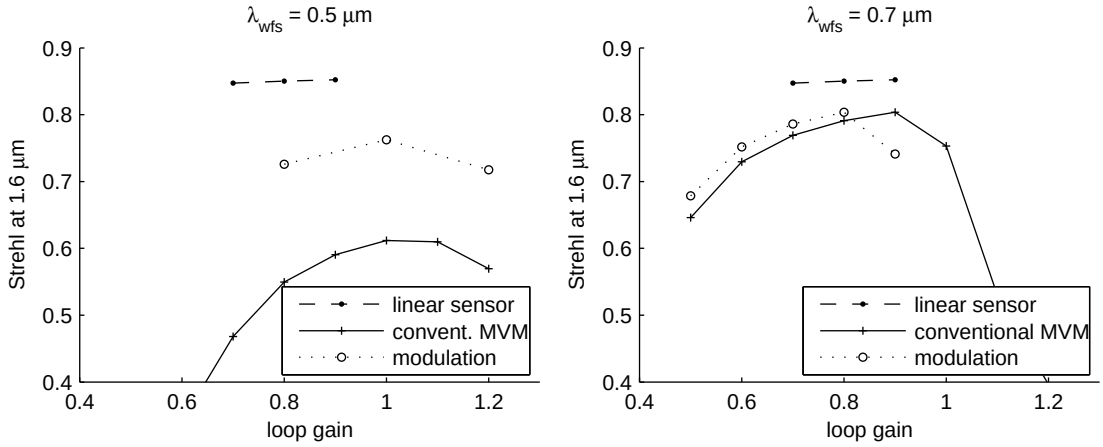

Figure 5.3: Long exposure Strehl as a function of loop gain. The dashed line is the linearized P-WFS sensor, the solid line with +-markers is the conventionally calibrated P-WFS, dotted line with circle markers is the case with modulation at calibration (12 and 2 λ/D). Left: $\lambda_{\mathrm{WFS}} = 0.5$ μm. Right: $\lambda_{\mathrm{WFS}} = 0.7$ μm.

atmosphere reduce significantly the sensitivity of the P-WFS with respect to the conditions in which an interaction matrix is recorded. (Without the turbulence mostly a diffraction limited spot is imaged on the tip of the pyramid.) Moreover, this loss of sensitivity is not evenly distributed over the DM modes. Thus, a usual global gain adjustment is actually only optimal for a reduced number of modes. The other modes are then either significantly under-corrected (large temporal error), or are in over-shoot because of a too high gain.

With P-WFS the optimal way of reconstruction depends on the magnitude of the incoming phase distortions. Not only the modes that can be measured, but also the high spatial frequency components present in the atmosphere affect the measurements. With a Shack-Hartmann WFS these result in aliasing. With P-WFS, however, these cause the measurements becoming reduced as illustrated in figure 5.4 while the aliasing problems are less significant (Vérinaud, 2004).

The effect can be illustrated in more detail by studying the effect of P-WFS saturation. We do this by pushing a mirror mode (the 3rd or 300th pseudo K-L) by different amounts and adding a typical atmospheric residual (originating from closed-loop AO simulations) on the obtained DM shapes. Three different seeing values (r_0 at 0.5 μm is 0.05, 0.08 and 0.10 m) and pure mirror mode ($r_0 = \infty$) are used. The P-WFS measurements of these resulting combined phases are then simulated using the AMA model. Finally, the corresponding modal reconstructions are computed using a conventionally calibrated command matrix.

Figure 5.5 illustrates the P-WFS saturation. Two measures are shown as a function of the applied perturbance (in terms of rms) for the original mirror mode: the reconstructed modal coefficient (3rd or 300th K-L) and the ratio between the chosen modal coefficient and the total reconstruction rms.

It is seen that the P-WFS behaves linearly until the rms of applied perturbation reaches about 50–100 nm. After this, saturation occurs: the reconstruction coefficient of the pushed mode increases much slower, and its proportion with respect

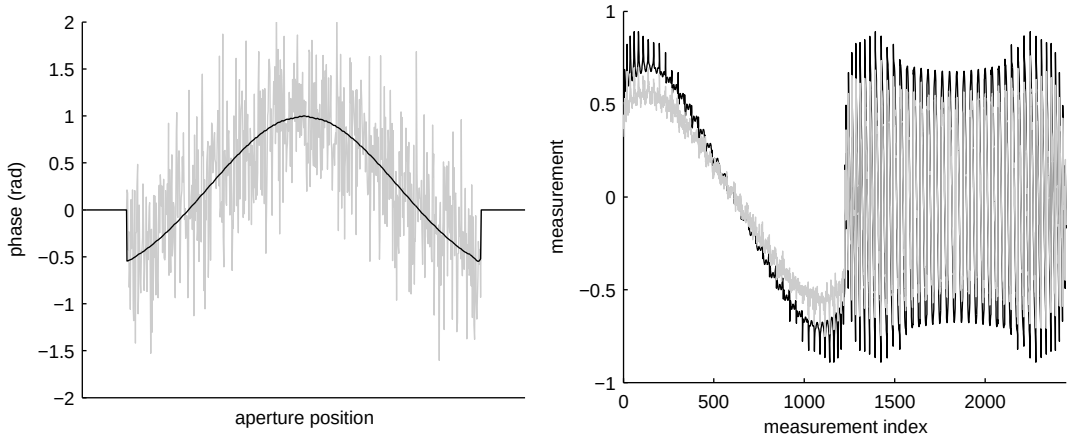

Figure 5.4: Illustration of the sensitivity reduction (Korkiakoski et al., 2008). Left: radial cuts of incoming phase at a WFS aperture, black plot is DM shape when a pure mirror mode is applied, gray plot is the mode having an atmospheric residual added on it. Right: the P-WFS signals resulting from the measurements of the corresponding phases. Indexes 1–1224 describe $S_x(\mathbf{r})$ and 1225–2448 $S_y(\mathbf{r})$ respectively.

to the other modal coefficients stops increasing — the sensor starts seeing also an increase of the other modes. When measuring only the pure mode without the atmospheric component, it is seen that this coupling starts already after the rms of applied perturbation is over about 30 nm.

It can be seen also very clearly that the reconstruction coefficient as a function of the rms of applied perturbation changes very differently for each seeing value. The worse the seeing, the lower is the slope of the plots. In addition, when comparing the K-L modes 3 and 300, significant differences can be seen: the slopes of the higher mode are over two times higher.

Thus, this shows that the loss in sensitivity, defined in this thesis as the ratio between the standard deviations of the measurement and wavefront, is heavily dependent on the seeing conditions and the sensing wavelength. Therefore, a wavefront reconstruction with the P-WFS must take into account both the seeing conditions and the specific behavior of the used sensor.

This suggests that the reconstruction should be designed carefully for each seeing case separately. However, the calibration modulation approach illustrated earlier in figure 5.3 would be extremely difficult to optimally implement in practice. No general theory exists to determine the extent of the modulation. Thus, the optimal reconstruction should be empirically determined by recording several interaction matrices with different modulations and then testing each of them in various seeing conditions.

In addition, the question arises, whether it is even possible to compensate the P-WFS saturation effect by a linear reconstruction matrix. As a consequence, before studying modal sensitivity compensation, we represent an iterative reconstruction method in the next section (Korkiakoski et al., 2007b) that can be used to evaluate the significance of the nonlinearities in the nonmodulated P-WFS.

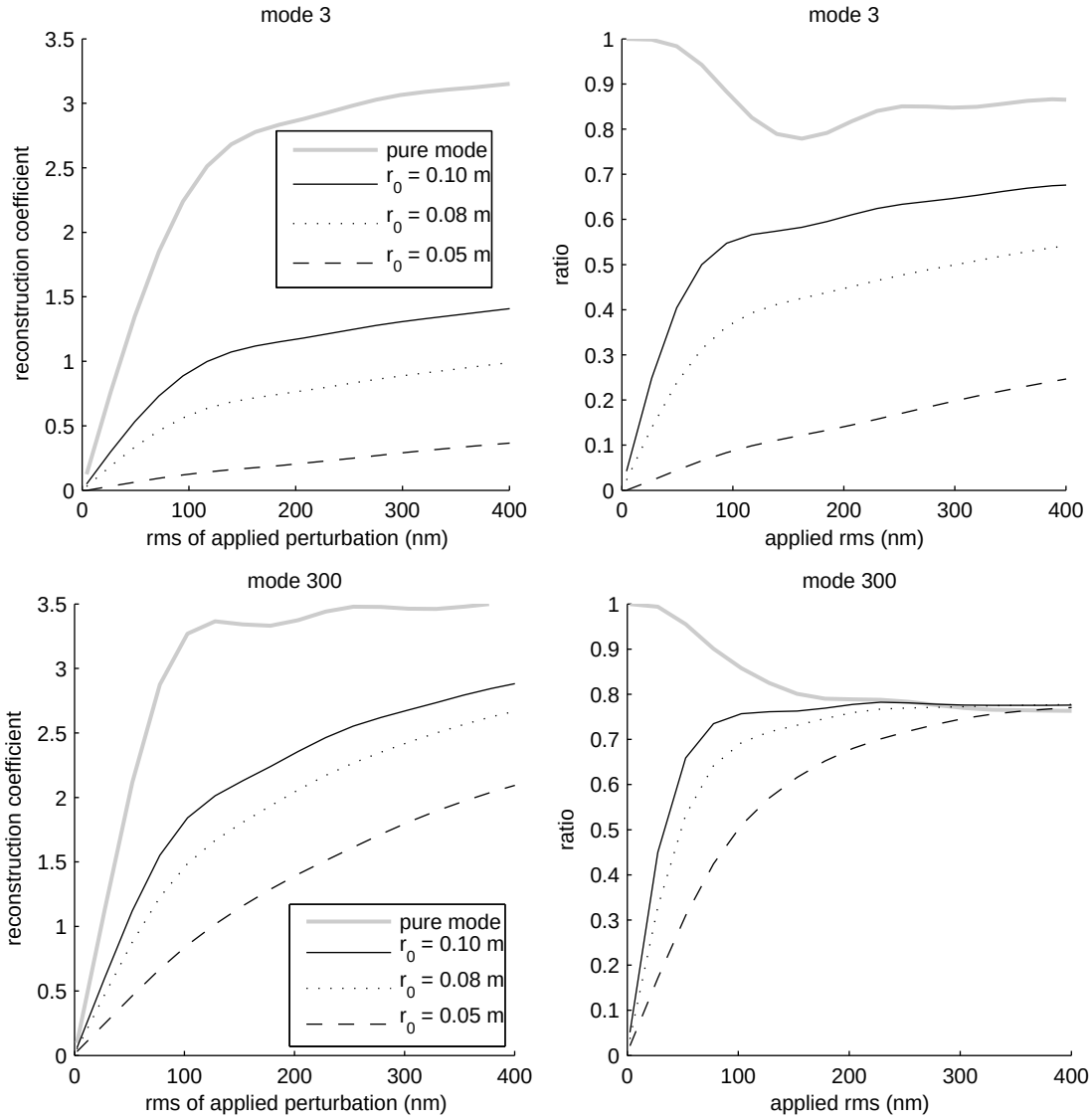

Figure 5.5: Demonstration of P-WFS saturation. A mode is pushed, a typical atmospheric residual is added on the mode (three seeing values are used: r_0 at 0.5 μm is 0.05, 0.08, 0.10 and ∞), the P-WFS measurement of the resulting shape is computed and then the modal reconstruction is computed by classical MVM. Measurement resolution is 40×40 and the AMA method is used for P-WFS simulation. Left column: the reconstructed modal coefficient as a function of applied perturbance. Right column: the ratio of the reconstruction coefficient and the total reconstruction rms.

5.2 Model based reconstruction

This section shows how a Fourier optics model of a nonmodulated P-WFS can be linearized at arbitrary phase position. These linearizations, represented by Jacobian matrices, are then used iteratively — by analogy to Newton's method — to find improved phase estimates for given measurements. Section 5.2.1 describes how this is accomplished in practice. Section 5.2.2 illustrates the properties of such Jacobian matrices and Section 5.2.3 summarizes how the Jacobian reconstruction (JR) method is used in an AO system.

As described previously, the P-WFS measurement signal is composed of the intensities at the CCD detector as shown in equation (5.1). An explicit formula for a nonmodulated sensor is derived in appendix A and given in equation (A.9). The derived model corresponds to the P-WFS with AMA assumption (see Section 5.1.1). A model not neglecting the interference terms, such as for instance the PMA method, would be much more complex.

The measurement signal in equation (5.1) is essentially a sum of sinusoidal functions of the incoming phase convolved by $1/x$, $1/y$ and delta functions. Its direct inversion is very difficult. However, it is known that the P-WFS can be operated in good seeing conditions (or using long sensing wavelengths) with a linear assumption ($S(\mathbf{r})$ is a linear function of $\phi(\mathbf{r})$). If the simple linear approximation is too inaccurate, additional methods have to be considered for the inversion problem.

If the signal of equation (5.1) is smooth enough as a function of $\phi(\mathbf{r})$, it can be linearized at all of its input values. If also each variable describing the measurement is a monotonous function of phase $\phi(\mathbf{r})$, an inverse of $S(\phi(\mathbf{r}))$ can be obtained using an iterative derivative based algorithm as shown in figure 5.6 and described in the following.

First, the signal model is used to create a linear approximation at $\phi = 0$, denoted as $\hat{S}(\phi) = J(0)\phi$. This approximation is used to find the first phase estimate $\hat{\phi}_0$ given the known signal measurement $S(\phi_r)$. Then again the model is used to create a linear approximation at $\hat{\phi}_0$ and the next phase estimate $\hat{\phi}_1$ is obtained. The iteration goes on until the real phase ϕ_r is obtained with an arbitrary accuracy.

In reality, however, the P-WFS measurement signal does not fulfill the monotonous requirements completely. The sinusoidal dependency of signal with respect to phase implies that if $\phi > \pi/2$, no inversion is possible. Nevertheless, as our simulation results will show, at least a few iterations can be carried out without problems and an improved phase estimate can be obtained.

5.2.1 Practical implementation

To linearize the signal $S(\mathbf{r})$ around $\phi(\mathbf{r})$, we need to know how a given point of the signal changes as a function of $\phi(\mathbf{r})$. For this purpose, we sample the phase with an $R \times R$ array of discrete points. R is at least as big as the resolution of the WFS measurement grid.

As figure 5.7 illustrates, this approximation gives N ($< R^2$) phase values since the phase is zero outside the aperture. Also the continuous signals $S_x(\mathbf{r})$ and $S_y(\mathbf{r})$ need to be discretized.

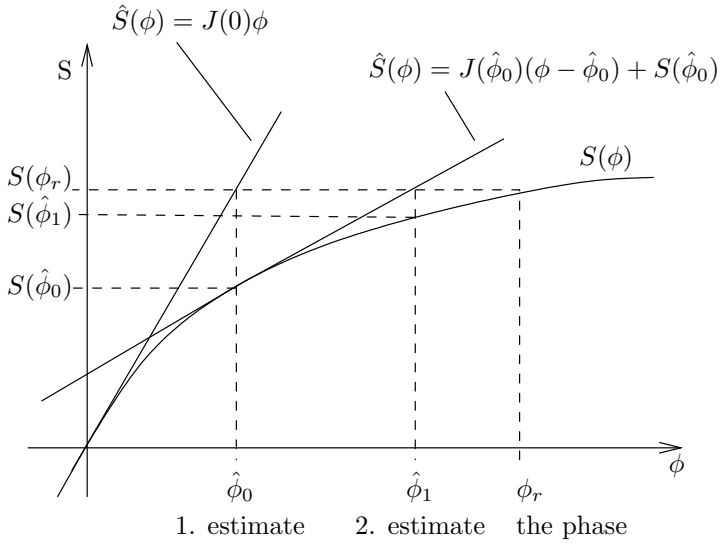

Figure 5.6: Descriptive illustration of an iterative, derivative based, numerical inversion of a monotonic nonlinear function (Korkiakoski et al., 2007b).

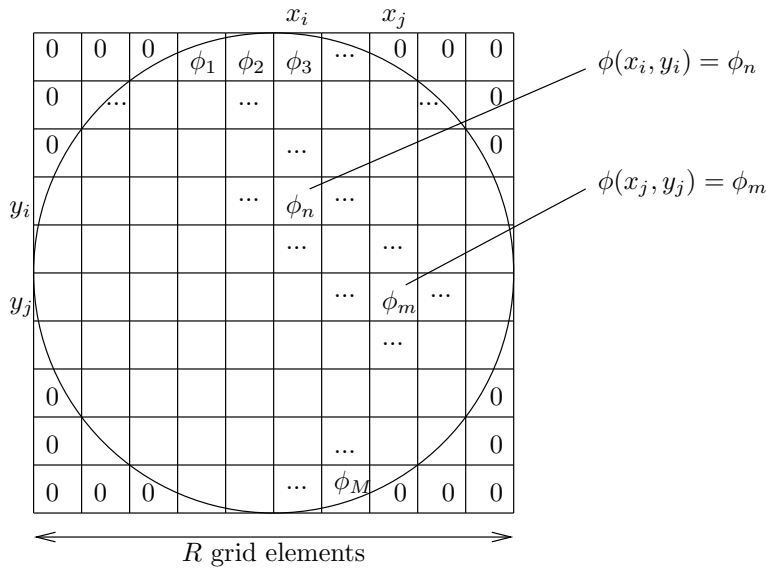

Figure 5.7: Illustration of the phase discretization for the model. An illumination threshold is required to choose which grid elements belong to the aperture and which are left outside (Korkiakoski et al., 2007b).

The signal approximation can thus be represented as an N-dimensional vector with each element being a function of the phase values over the grid,

$$\begin{aligned} S_x(x,y) &\simeq \left[S_x^1(\phi_1,\cdots,\phi_N)\cdots S_x^N(\phi_1,\cdots,\phi_N)\right] \\ S_y(x,y) &\simeq \left[S_y^1(\phi_1,\cdots,\phi_N)\cdots S_y^N(\phi_1,\cdots,\phi_N)\right], \end{aligned} \tag{5.2}$$

The elements of the signal vector can also be denoted as $S_x^{x_i,y_i}(\boldsymbol{\phi})$ meaning that the point (x_i, y_i) corresponds to the index n (see figure 5.7).

This enables making two $N \times N$ Jacobian matrices describing how the x- and y-signals change as a function of the phase in the pupil area. The Jacobian can be computed element-wise given the coordinates (x_i, y_j) for the Jacobian row and (x_j, y_j) for the Jacobian column,

$$J^{n,m}(\boldsymbol{\phi}) = \begin{bmatrix} J_x^{n,m}(\boldsymbol{\phi}) \\ J_y^{n,m}(\boldsymbol{\phi}) \end{bmatrix} = \begin{bmatrix} \dfrac{\partial S_x^{x_i,y_i}(\phi_1,\cdots,\phi_N)}{\partial \phi_{x_j,y_j}} \\ \dfrac{\partial S_y^{x_i,y_i}(\phi_1,\cdots,\phi_N)}{\partial \phi_{x_j,y_j}} \end{bmatrix}, \tag{5.3}$$

where the row and column indexes n and m corresponds to the coordinates as shown in figure 5.7.

The formulas for equation (5.3) have been derived in appendix B.

5.2.2 Properties of the Jacobian

The Jacobian matrix of equation (5.3) has twice as many rows as columns. The exact size depends on the grid points lying inside the aperture (at borders an illumination threshold is used). The number of the Jacobian elements is approximately

$$2\left[\pi\left(\frac{R}{2}\right)^2\right]\left[\pi\left(\frac{R}{2}\right)^2\right] = \frac{1}{8}\pi^2 R^4 \tag{5.4}$$

meaning that the computational requirements of the Jacobian increase to the fourth power of the resolution R.

As seen in equation (B.8), the Jacobian can be divided into two parts. The first part is due to the measurement signal of the two-sided pyramid sensor (m_x, m_y) and the latter comes from the cross-terms (c_x, c_y).

The main content of the Jacobian comes from the terms m_x and m_y. For instance, with a dimension $R = 40$ giving a Jacobian of size 2464×1232 the relative energy difference between a complete Jacobian and a Jacobian without the cross-terms,

$$\sum_{\text{elements}} \left(J_{\text{full}}(0) - J_{\text{m}}(0)\right)^2 / \sum_{\text{elements}} \left(J_{\text{full}}(0)\right)^2,$$

is 7.0%. In addition, if the cross-terms were neglected, the resulting Jacobian would be sparse. For instance, a Jacobian of 2464×1232 would have 2.7% of the elements non-zero. A system with $R = 160$ and a Jacobian of 40216×20108 would have 0.68% of the elements non-zero. It can also be noted that the cross-terms contribute only to the Jacobian elements where the contribution of m_x (or m_y) is zero.

Therefore, it is possible to consider the sparse Jacobian of the two-sided P-WFS (computed considering only terms m_x and m_y) as an approximation of the complete four-sided P-WFS Jacobian. In our simulations this approximation typically gave 1–3 percent lower Strehl ratio compared to the cases with the full Jacobian.

Yet another interesting question is, whether the Jacobian matrix can be inverted. As the matrix $J(\phi)$ has more rows than columns, the linear equation

$$\mathbf{S} = J(\boldsymbol{\phi})\boldsymbol{\phi}_w \tag{5.5}$$

is invertible given that $J(\boldsymbol{\phi})$ is well conditioned. We computed 2464×1232 sized Jacobians for several typical residual phases in an AO loop. It was found that the condition numbers were always lower than 50. A theoretical study has not been carried out, but our simulations indicate that equation (5.5) is indeed solvable with all Jacobians created in any meaningful phase input $\boldsymbol{\phi}$.

5.2.3 Application in the AO loop

Figure 5.8 illustrates the AO system we used in our simulations. The WFS measures the incoming wavefront $\boldsymbol{\phi}_w$ using an intensity pattern at the detector plane. Equation (5.1) shows how the measured intensity is interpreted as two 2-dimensional signals $S_x(\mathbf{r})$ and $S_y(\mathbf{r})$.

In a system having four $R_s \times R_s$ pixel CCD grids, $S_x(\mathbf{r})$ and $S_y(\mathbf{r})$ are sampled by $R_s \times R_s$ matrices (S_{mx} and S_{my}) where the elements outside aperture are zero. The non-zero elements of S_{mx} and S_{my} can be organized into a measurement vector $\mathbf{S}$. In the linear regime the WFS can be approximated as a linear mapping $\mathbf{S} = B\boldsymbol{\phi}_w$.

The phase reconstruction can be accomplished using either the conventional MVM (a pseudo-inverse of B is used) or the Jacobian reconstruction (JR).

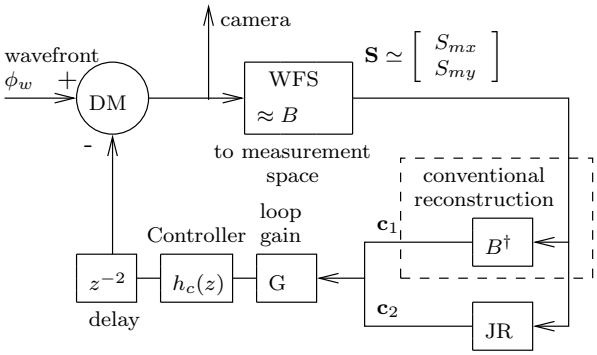

Figure 5.8: Illustration of the simulated system (Korkiakoski et al., 2007b).

To use the JR two parameters must be set — the Jacobian resolution (R) and the number of Jacobian iteration steps (N_{it}). The iteration steps are illustrated in figure 5.6. If the signal is smooth, the more Jacobian iterations, the more accurate can the reconstruction be. The Jacobian resolution, on the other hand, defines the accuracy of the model — the reconstruction is not restricted to the resolution of the measurement grid.

If only a single Jacobian iteration is used, the JR is completely a linear process. The first phase estimate (in a vector form with a resolution of $R \times R$) can be computed as

$$\boldsymbol{\phi} = \left[J(0)\right]^{\dagger} X_m \mathbf{S}, \tag{5.6}$$

where $\left[J(0)\right]^{\dagger}$ is a pseudo-inverse of the Jacobian at $\boldsymbol{\phi} = 0$ and X_m is an interpolation matrix constructed to perform a bilinear interpolation $\mathbf{S}_b = X_m \mathbf{S}$. The vector $\mathbf{S}_b$ represents the measurement signal with a resolution of $R \times R$ instead of the original CCD pixel resolution $R_s \times R_s$.

The nth element of $\boldsymbol{\phi}$ represents the phase value at the nth position on the pupil as illustrated in figure 5.7. This corresponds to phase $\phi_n g_n(\mathbf{r})$, where $g_n(\mathbf{r})$ is one inside the nth grid element ($\mathbf{r} \in r(x_i, y_i)$) and zero otherwise. The actuator commands letting the DM shape to best fit in the least squared sense the phase $\phi_n g_n(\mathbf{r})$, are computed as

$$\mathbf{v}_n = C_m^{-1} \mathbf{a}_n \phi_n, \tag{5.7}$$

where matrix C_m describes the overlapping of the actuator influence functions $f_i(\mathbf{r})$ (see section 2.3) and vector $\mathbf{a}_n$ describes the effect of the influence functions at the nth grid element,

$$C_m(i,j) = \int_{\text{aperture}} f_i(\mathbf{r}) f_j(\mathbf{r}) \mathrm{d}\mathbf{r}, \tag{5.8}$$

$$\mathbf{a}_n(i) = \int_{\text{aperture}} g_n(\mathbf{r}) f_i(\mathbf{r}) \mathrm{d}\mathbf{r}. \tag{5.9}$$

The sum of all commands $\mathbf{v}_n$ ($n = 1, \ldots, N$) is the best DM fit for the JR phase estimate $\boldsymbol{\phi}$. It is computed as

$$\mathbf{c}_2 = C_m^{-1} \left[\mathbf{a}_n \ \cdots \ \mathbf{a}_N\right] \left[J(0)\right]^{\dagger} X_m \mathbf{S}, \tag{5.10}$$

where the matrix $C_m^{-1} \left[\mathbf{a}_n \ \cdots \ \mathbf{a}_N\right] \left[J(0)\right]^{\dagger} X_m$ is a synthetic command matrix having the same dimensions as the command matrix used in the conventional MVM.

The computational requirements of the JR depend on N_{it}. When $N_{\text{it}} = 1$, the synthetic command matrix can be computed off-line as shown before. This makes JR computationally equivalent to MVM. However, if $N_{\text{it}} > 1$, the amount of computation increases dramatically — at each iteration one must recompute the Jacobian, compute a new measurement estimate and solve $\boldsymbol{\phi}^i$ from the linear equation

$$\mathbf{S}_b = J(\boldsymbol{\phi}^{i-1})(\boldsymbol{\phi}^i - \boldsymbol{\phi}^{i-1}) + \hat{\mathbf{S}}_b^{i-1}. \tag{5.11}$$

This means 50–1000 times slower reconstruction time depending on the used solver algorithms.

5.3 Simulations of model based control

5.3.1 Scope

We made a set of end-to-end AO closed-loop simulations with parameters shown in Table 5.1. We simulated an 8 meter telescope with turbulence of Fried parameter

$r_0 = 8$ cm at 0.5 μm wavelength. The simulation of the P-WFS was implemented by a straightforward application of equation (A.9).

Table 5.1: Simulation parameters (Korkiakoski et al., 2007b)

Telescope diameter	8 m
Central obstruction	none
λ_{img}	1.6 μm
λ_{WFS}	0.5, 0.7, 1.65 μm
Noise	no
Measurement resolution (R_s)	40
Frame-rate	1 kHz
Influence functions	Linear spline, no cross-coupling
Servo lag	2 frames
Controller	Simple integrator
Number of layers	2
Wind speeds	6, 15 m/s
Outer scale L_0	26 m
r_0 at 0.5 μm	0.08 m
Simulated frames	336
Simulation resolution	320×320

The simulations were based on the parallel software described in more detail in Section 2.5.2. We made most of our simulations using only a single turbulence realization as our goal is only to demonstrate the feasibility of JR. Comparisons between different models and reconstruction methods are done by using identical phase screens. However, as described later, in selected cases we also made a statistical analysis with five different turbulence realizations to show the error range of our results.

In all our simulations the Strehl ratio reached a steady state after about 100 simulated frames. The additional frames were simulated to ensure that no slowly deviating instabilities were present.

We optimized the MVM reconstruction (in terms of the best long exposure Strehl ratio) by choosing the optimal number of controlled modes. The system had 1347 degrees of freedom and we controlled 998 mirror modes (Karhunen-Loeve approximations). In this way it was not necessary to truncate any singular values when inverting the modal interaction matrix. The modal interaction matrix was made by measuring the mirror modes at the linear regime and each mode was normalized to have the same maximum value. We also tested the MVM by controlling more modes (up to 1346) and truncating the optimal number of singular values when inverting the interaction matrix. Also a zonal interaction matrix was tested. These tests, however, did not improve the performance.

As a controller, we used a simple integrator with a constant loop gain individually optimized for each simulation parameter set.

The P-WFS simulation results are compared with results obtained by using a linear sensor. The linear WFS is simulated by replacing $\cos\phi(\mathbf{r})$ by 1 and $\sin\phi(\mathbf{r})$

by $\phi(\mathbf{r})$ in the signal shown in equation (A.9). This linear WFS is then controlled with the same MVM reconstruction as the original P-WFS. This enables obtaining a clear measure of how much the nonlinearities decrease the P-WFS performance.

5.3.2 Results

At first, we tested the JR performance in a closed-loop simulation with a static phase distortion (no wind) using a sensing wavelength of 0.5 μm. In this way we could see how much of the P-WFS nonlinearity can ideally be compensated. It was noted that the final steady level of the Strehl ratio, when using the conventional MVM, was 0.860 (the linear sensor), 0.845 (two-sided P-WFS) or 0.825 (four-sided P-WFS). The JR with $N_{\mathrm{it}} = 1$ gave as good results as the MVM and the help of the additional Jacobian iterations was negligible.

This loss of 0.015–0.035 in Strehl ratio may be explained by a higher sensitivity to aliasing for the P-WFS in the nonlinear regime. We also noted that a single Jacobian iteration was enough in all our further simulations. Therefore, we will consider in the following only JR with $N_{\mathrm{it}} = 1$.

Next we consider the real closed-loop simulations with temporal evolution of the turbulence by shifting the phase screens based on the wind speed values. In figure 5.9 we analyze the effect of loop gain when using the P-WFS. The long exposure Strehl ratio is plotted for the conventional MVM and JR with both two- and four-sided P-WFS. These results are averaged from five different turbulence realizations.

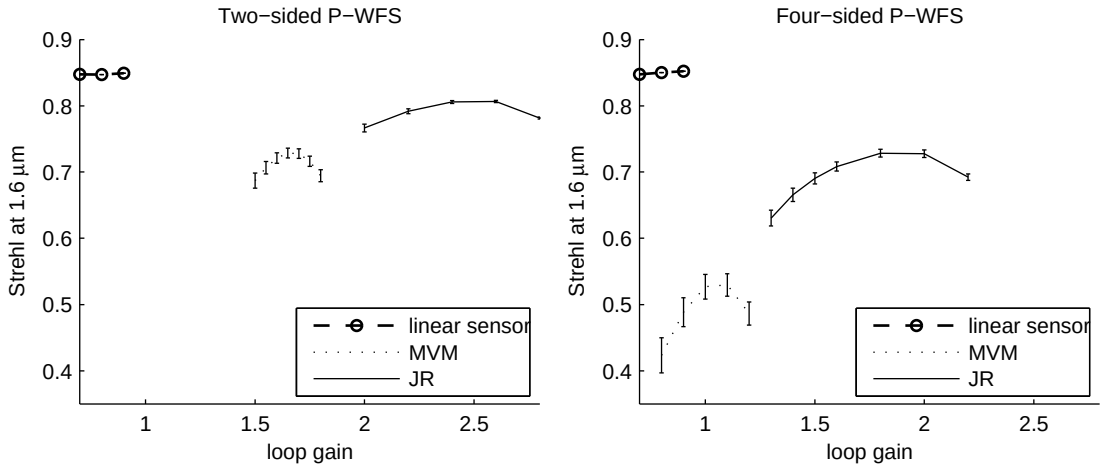

Figure 5.9: Long exposure Strehl as a function of loop gain ($\lambda_{\mathrm{WFS}} = 0.5$ μm). Averages and standard errors from five set of simulations are shown. Circle markers with dashed lines show the results with a linear sensor, dotted lines with conventional MVM and solid lines with JR ($R = 160$, $N_{\mathrm{it}} = 1$). Left: two-sided P-WFS. Right: four-sided P-WFS. (Korkiakoski et al., 2007b).

It can be noted that the two-sided P-WFS performs better than the four-sided classical P-WFS (the optimal Strehl ratios are 0.73 and 0.53 (MVM) or 0.81 and 0.73 (JR)). This result is also confirmed by (Phillion and Baker, 2006) and suggests that the cross-terms of equation (B.1) contribute significantly to the nonlinear behavior of the four-sided pyramid sensor.

Concerning the dependency on loop gain, we need to draw the attention on the fact that the optimum Strehl ratios are obtained at gains higher than one, even for the JR method which should, in principle, better describe the measurement accuracy. Indeed, the optimum gains of the JR (1.8 and 2.6) are higher compared to the optimum gains of the MVM (1.0 and 1.65). However, the optimal Strehl ratios of JR are always 0.05–0.15 better than of the MVM reconstruction.

This peculiar behavior suggests that a normalization issue exists in the pyramid model. Among possible reasons, the fraction of light diffracted by the very sharp prism edges out of the four geometrical pupils may not be described with sufficient accuracy by the model and could explain this normalization issue. This definitely needs a deeper analysis.

It was noted that the higher the Jacobian resolution, the better is the performance. A resolution of $R = 80$ gave about 0.015 worse Strehl ratios (compared to $R = 160$) and $R = 40$ was too low to make the AO loop stable.

Next we simulated both two- and four-sided P-WFS for three different sensing wavelengths: 0.5, 0.7 and 1.65 μm. The optimum Strehl ratios of those simulations are shown in Table 5.2.

Table 5.2: Optimal Strehl ratios (Korkiakoski et al., 2007b)

	Two-sided P-WFS			Four-sided P-WFS		
λ_{WFS} (μm)	1.65	0.7	0.5	1.65	0.7	0.5
linear sensor	0.849	0.849	0.849	0.852	0.852	0.852
MVM	0.849	0.837	0.729	0.848	0.804	0.530
JR[a]	0.842	0.837	0.807	0.840	0.809	0.728

[a] $R = 160, N_{\mathrm{it}} = 1$

It can be seen that when using a two-sided P-WFS with any reconstruction method, almost the optimal Strehl ratio of 0.85 can be obtained at high wavelengths. However, at $\lambda_{\mathrm{WFS}} = 0.5$ μm the Strehl ratio is already 0.12 lower with MVM reconstruction and 0.04 lower with JR. The four-sided P-WFS gives even worse results. The Strehl ratio at $\lambda_{\mathrm{WFS}} = 0.5$ μm is with MVM 0.32 lower and with JR 0.12 lower than the optimum.

Thus, the JR is indeed most useful at the nonlinear regime of the P-WFS. At $\lambda_{\mathrm{WFS}} = 1.65$ μm the JR gives 0.007 worse Strehl ratio compared the MVM reconstruction. This can be explained by the approximative nature of the JR. Correctly calibrated MVM is by definition the optimal way of reconstruction, if the sensor is fully linear. JR, on the other hand, uses an approximated model to compute the actuator commands — and slight inaccuracies are inevitable.

In high contrast imaging it is also important to optimize the power spectral density (PSD), defined as

$$\mathrm{PSD}(\mathbf{f}) = \left\langle \left| \mathscr{F}\{\phi(\mathbf{r})\} \right|^2 \right\rangle, \tag{5.12}$$

where $\mathscr{F}\{\phi(\mathbf{r})\}$ is the Fourier transform of the residual phase and $\langle \cdot \rangle$ denotes temporal averaging.

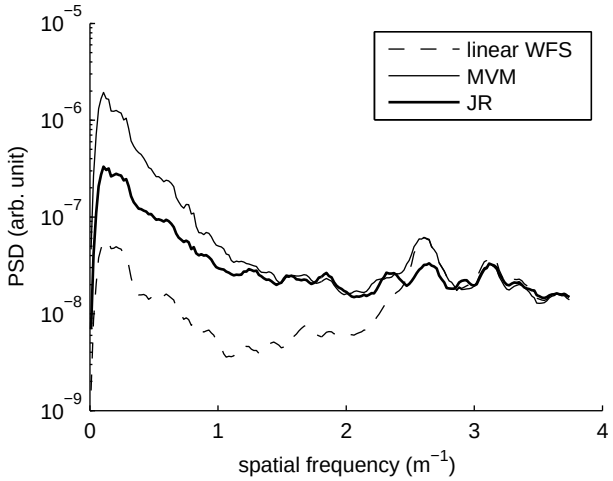

Figure 5.10: Radially averaged power spectral densities of the residual phases in two-sided P-WFS simulations with optimal loop gains at $\lambda_{\mathrm{WFS}} = 0.5$ μm. JR was used with $R = 160$ and $N_{\mathrm{it}} = 1$. (Korkiakoski et al., 2007b).

The radially averaged PSDs of the two-sided P-WFS simulation using the optimal loop gains at $\lambda_{\mathrm{WFS}} = 0.5$ μm are shown in figure 5.10.

It can be seen that the JR mainly helps to reduce the residual energy at low spatial frequencies (< 1.0 m^{-1}), which is particularly important for the detection of exoplanets at small angular separations from their host star (Vérinaud et al., 2005). The reduction at the lowest spatial frequencies is to one third of the case where MVM reconstruction was applied. However, with larger frequencies JR gives practically the same results as the MVM.

5.3.3 Discussion

It has been shown that the performance of the conventionally calibrated MVM can be improved by using a diffraction model with a synthetic Jacobian based reconstruction matrix as described here.

We analyzed the JR performance in difficult conditions ($r_0 = 0.08$ m and $\lambda_{\mathrm{WFS}} = 0.5$ μm), where the optimal Strehl ratio given by a linear sensor was about 0.85. The Strehl ratio of a classical four-sided P-WFS can be improved from 0.53 up to 0.73 and the ratio of a two-sided P-WFS from 0.73 up to 0.81.

It can be concluded that the two-sided P-WFS is more linear compared to the four-sided P-WFS. This means that the cross-terms — not present in the two-sided P-WFS — are responsible of most of the nonlinearity properties in the classical pyramid sensor.

In addition, it was seen that most of the JR Strehl ratio improvement is achieved by only a single Jacobian iteration — the increase of the additional iterations is negligible. This implies that the P-WFS indeed saturates rather fast and the nonlinearities cannot be efficiently compensated in the conditions encountered by a typical AO system. Besides, in typical closed-loop AO the pyramid sensor is operated in the linear regime as illustrated in figure 5.5.

However, we demonstrated that the linear approximation of the JR gives better

results compared to the conventionally calibrated MVM. This can be explained by the problems in the conventional calibration. As illustrated by figures 5.4 and 5.5, the sensitivity reduction — if not taken into account — is guaranteed to cause problems when measuring high wavefront distortions. Indeed, it has been shown that building an interaction matrix in the linear regime (small perturbation) by recording the response of the WFS to, for instance, DM modes applied alone, and then inverting the corresponding interaction matrix, is not optimum. Nevertheless, when using the synthetically computed command matrix, it became possible to apply higher loop gains to better adjust to the worse seeing conditions.

To conclude, the linear reconstruction is feasible for AO closed-loop operation with the nonmodulated pyramid sensor in bad seeing conditions. However, to optimally design the linear reconstructor, a priori information (i.e., von Karman power law and the value of the Fried parameter) of the incoming wavefront can be used with more advanced control algorithms. But for this, a better insight in the pyramid model nonlinearities is needed. The next section will address this issue.

5.4 Sensitivity compensation

This section presents an alternative to the JR method to design the reconstruction matrix.

The method, published in (Korkiakoski et al., 2008), is based on a heuristic modal sensitivity compensation, directly inspired by figure 5.4. In this method, AO control system provides data that can be used to obtain improved "estimates" of the residual phase power spectrum. These estimates are then used to compute suitable modal sensitivity compensation and the reconstruction matrix is updated consequently.

Section 5.5 will then demonstrate how this reconstruction method performs in complete end-to-end AO closed-loop simulations. In particular, we compare the performance of a modal predictive controller (see Section 3.3.3) and a simple integrator when the compensation is applied.

5.4.1 Overview of the method

Our new approach is based on three main steps to be fulfilled by the control system:

1. The first step consists of collecting a series of DM commands and sensor measurements during a given period (a few seconds or so) in closed-loop. From these data (and the knowledge of the turbulence statistics), we compute an estimation of the spatial power spectrum of the real residual wavefront error that occurred during this period. A similar approach already exists and has been implemented in PUEO for PSF estimation from closed-loop data (Véran et al., 1997). The way we implement this first step is described in Section 5.4.2.

2. The second step consists of an estimation of the modal sensitivity loss. Our goal is to estimate for each DM mode what is the loss of sensitivity in presence of residuals with a PSD similar to the one we have estimated from the real data.

This step requires much more computations than the first step and is computed off-line. The method consists of using a wave optics code based on fast Fourier transforms as a model of the real system and thus to estimate the sensitivity loss by simulations. The output of this step are Sensitivity Compensation Coefficients (SCCs) which represent the correction to be applied to the modal wavefront reconstruction to compensate the loss. This step is described in Section 5.4.3.

3. Finally the third step consists of updating the modal wavefront reconstruction matrix by correcting the reconstruction coefficients with the SCCs (see Section 5.4.4).

Then a new iteration starting with step 1 follows and the process is forced to converge iteratively to the optimal correction by successive improvements in the values of the SCCs. The steps are also illustrated in figure 5.11.

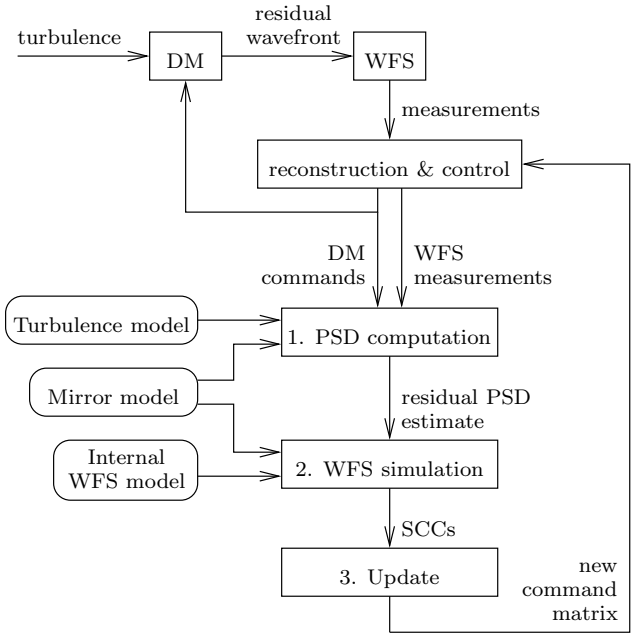

Figure 5.11: Diagram of the method of sensitivity compensation in closed-loop (Korkiakoski et al., 2008).

5.4.2 PSD estimation from closed-loop data

As the DM cannot correct spatial frequencies higher than the cutoff frequency, the temporally averaged spatial power spectrum density (PSD) of the phase obeys the von Karman power law outside the cutoff frequency ($1/(2d)$ with actuator grid spacing being d). Inside the cutoff frequency the residual PSD can be estimated from the WFS measurements. Thus, the PSD estimate can be decomposed as

$$\tilde{\phi}_{\text{resi}}(\mathbf{f}) = \begin{cases} \tilde{\phi}_{\text{LF}}(\mathbf{f}), & \text{when } f \leq 1/(2d) \\ C\left(f^2 + L_0^{-2}\right)^{-11/6}, & \text{when } f > 1/(2d) \end{cases}, \tag{5.13}$$

where $\mathbf{f}$ is the spatial frequency and $f = |\mathbf{f}|$. This requires the estimation of a seeing dependent parameter C and the measurement dependent function $\tilde{\phi}_{\mathrm{LF}}(\mathbf{f})$. The outer scale L_0 has a negligible effect when $f > 1/(2d)$ and its accurate determination is not necessary for telescopes having a diameter of only 8 meters.

Next is shown how to estimate $\tilde{\phi}_{\mathrm{resi}}(\mathbf{f})$ by using the modal DM commands and the sensor measurements collected from some time interval.

The phase shapes of the DM at time step k can be written as

$$\phi^k_{\mathrm{DM}}(\mathbf{x}) = \sum_{i=1}^{M} y_i(k) M_i(\mathbf{x}), \tag{5.14}$$

where the summing is done over the M controlled mirror modes, $M_i(\mathbf{x})$ are functions describing the phase shapes of the modes and $y_i(k)$ are the modal DM commands at time step k. Thus, we assume that the phase shapes of the applied mirror modes are known explicitly (i.e., no hysteresis or DM nonlinearities).

Similarly, the residual phase — without the high spatial frequencies — at time step k can be written as

$$\phi^k_{\mathrm{LF}}(\mathbf{x}) = \sum_{i=1}^{M} c'_i(k) M_i(\mathbf{x}), \tag{5.15}$$

where $c'_i(k)$ are the modal reconstruction coefficients. They are obtained by using the actual modal command matrix applied to the measurement series.

The corresponding temporally averaged PSD estimates of equations (5.14) and (5.15) can be written as

$$\tilde{\phi}_{\mathrm{DM}}(\mathbf{f}) = \frac{1}{N_k} \sum_{k=k_1}^{k_2} \left| \mathscr{F}\{\mathcal{W}(\mathbf{x}) \sum_{i=1}^{M} y_i(k) M_i(\mathbf{x})\} \right|^2, \tag{5.16}$$

$$\tilde{\phi}_{\mathrm{LF}}(\mathbf{f}) = \frac{1}{N_k} \sum_{k=k_1}^{k_2} \left| \mathscr{F}\{\mathcal{W}(\mathbf{x}) \sum_{i=1}^{M} c'_i(k) M_i(\mathbf{x})\} \right|^2, \tag{5.17}$$

where the outer summing (indexed with k) is taken over the selected time steps and $N_k = k_2 - k_1 + 1$ is chosen to be large enough for sufficient turbulent statistics. $\mathscr{F}\{\cdot\}$ denotes a Fourier transform and $\mathcal{W}(\mathbf{x})$ is a windowing function decreasing the effect of finite sampling of $M_i(\mathbf{x})$, for example a two-dimensional Blackman window (Hayes, 1996).

The residual PSD estimate $\tilde{\phi}_{\mathrm{LF}}(\mathbf{f})$ can be substituted as such into equation (5.13). The DM PSD estimate should be equal to the incoming turbulence PSD inside the cutoff frequency and thus it can be used in determining the coefficient C.

In principle, the coefficient C could be estimated with any method determining the seeing of the turbulence, for instance (Véran et al., 1997), and then using the relation

$$C = 0.1517\ r_0^{-5/6}, \tag{5.18}$$

where r_0 is the Fried parameter. However, here we use an approach taking the information from all the applied DM commands.

The value of L_0 is not determined, but as long as it is sufficiently large, it holds that the von Karman turbulence and $\tilde{\phi}_{\mathrm{DM}}(\mathbf{f})$ are almost equal over the range of

$b < f < 1/(2d)$, where b is about 1/5 of the cutoff frequency. Too small a value of b requires knowledge of L_0 and too large a value of b wastes information from $\tilde{\phi}_{\mathrm{DM}}(\mathbf{f})$. The value of C is computed as

$$C = \frac{\int_{b<f<1/(2d)} \tilde{\phi}_{\mathrm{DM}}(\mathbf{f})\ \mathrm{d}\mathbf{f}}{\int_{b<f<1/(2d)} \left(f^2 + \hat{L}_0^{-2}\right)^{-11/3} \mathrm{d}\mathbf{f}}, \tag{5.19}$$

where $\hat{L}_0^{-2}$ is a small constant. This constant C is then substituted into equation (5.13).

5.4.3 Off-line estimation of SCCs with a wave-optics model

To estimate the SCCs we are going to use a wave-optics model of the P-WFS. For this task we need to compute random phase screens realizations that follow the residual PSD computed at step 1. These random phase screens are computed by filtering random noise,

$$\hat{\phi}(\mathbf{x}) = \mathrm{Re}\left\{\mathscr{F}^{-1}\{n(\mathbf{f})\left[\tilde{\phi}_{\mathrm{resi}}(\mathbf{f})\right]^{\frac{1}{2}}\}\right\}, \tag{5.20}$$

where $n(\mathbf{f})$ is white and normally distributed noise with zero mean and unit variance, and $\tilde{\phi}_{\mathrm{resi}}(\mathbf{f})$ is computed as shown in equation (5.13).

If needed, several realizations of $\hat{\phi}(\mathbf{x})$ can be drawn from a single PSD. However, as it will be explained, in the cases we studied a single realization was sufficient.

Next it is shown how we compute the SCCs. We assume that the used P-WFS is known: there exists a model mapping a given phase to the P-WFS signal (i.e., we have an internal P-WFS model). Also the explicit knowledge of the applied mirror modes is still required.

From the used model it follows that each measurement element (total N elements provided) can be described as a function of the phase at the P-WFS aperture. In the following they are denoted as $m_j(\,\cdot\,)$, $j = 1,\ \ldots,\ N$.

When calibrating the P-WFS conventionally (applying mirror modes at the linear regime of the sensor), the ith column of the interaction matrix can be modeled as

$$\mathbf{m}_i^0 = \begin{bmatrix} m_1\big(\alpha M_i(\mathbf{x}) + 0\big) \\ \vdots \\ m_N\big(\alpha M_i(\mathbf{x}) + 0\big) \end{bmatrix} - \begin{bmatrix} m_1\big(0\big) \\ \vdots \\ m_N\big(0\big) \end{bmatrix}, \tag{5.21}$$

where $\alpha M_i(\mathbf{x})$ is the shape of the mirror after the ith mode is pushed by an amount of α. The addition of zero is explicitly written to emphasize that this formula describes the measurements without the residual phase of the atmosphere. The first term is the measurement of the ith mode and the second term is the reference measurement for the DM being flat.

Then we choose a measure for how "strongly" the ith mode is seen. It is described by the energy $\left(\mathbf{m}_i^0\right)^T \mathbf{m}_i^0$.

Similarly, we can describe how well the mode is seen when there is a residual phase added on the calibration measurement. In that case the energy would be $\left(\mathbf{m}_i^{\phi}\right)^T \mathbf{m}_i^{\phi}$, where

$$\mathbf{m}_i^{\phi} = \begin{bmatrix} m_1\left(\alpha M_i(\mathbf{x}) + \hat{\phi}(\mathbf{x})\right) \\ \vdots \\ m_N\left(\alpha M_i(\mathbf{x}) + \hat{\phi}(\mathbf{x})\right) \end{bmatrix} - \begin{bmatrix} m_1\left(\hat{\phi}(\mathbf{x})\right) \\ \vdots \\ m_N\left(\hat{\phi}(\mathbf{x})\right) \end{bmatrix}. \tag{5.22}$$

Here we have just replaced the flat reference phase by the residual realization $\hat{\phi}(\mathbf{x})$.

It is seen directly that $\left(\mathbf{m}_i^{\phi}\right)^T \mathbf{m}_i^{\phi}$ would be equal to $\left(\mathbf{m}_i^{0}\right)^T \mathbf{m}_i^{0}$ if the sensor were linear. However, in the case of a P-WFS, the addition of the residual makes the energy $\left(\mathbf{m}_i^{\phi}\right)^T \mathbf{m}_i^{\phi}$ smaller than $\left(\mathbf{m}_i^{0}\right)^T \mathbf{m}_i^{0}$. This also means that when creating the modal reconstruction based on the obtained measurements, the ith modal component becomes — without compensation — underestimated.

We scale the modal reconstruction coefficients in the same proportion as the ratio of these energies suggests. Thus, the SCCs for a given phase realization $\hat{\phi}(\mathbf{x})$ are defined as

$$\xi_i(\hat{\phi}(\mathbf{x})) = \left[\frac{\left(\mathbf{m}_i^{0}\right)^T \mathbf{m}_i^{0}}{\left(\mathbf{m}_i^{\phi}\right)^T \mathbf{m}_i^{\phi}}\right]^{\frac{1}{2}} = \left[\frac{\sum_{j=1}^{N}\left[m_j\left(\alpha M_i(\mathbf{x})\right) - m_j(0)\right]^2}{\sum_{j=1}^{N}\left[m_j\left(\hat{\phi}(\mathbf{x}) + \alpha M_i(\mathbf{x})\right) - m_j\left(\hat{\phi}(\mathbf{x})\right)\right]^2}\right]^{\frac{1}{2}}. \tag{5.23}$$

The SCCs should not depend on the amount the modes are pushed at the calibration stage. Therefore, the expression should have a limit as $\alpha \to 0$, but it can be numerically computed for sufficiently small values of α.

Since the residual realizations $\hat{\phi}(\mathbf{x})$ represent the real residual only through their stochastic properties, the actual SCCs must be defined as an ensemble average,

$$\hat{\xi}_i = \left\langle \xi_i(\hat{\phi}(\mathbf{x})) \right\rangle, \tag{5.24}$$

where the phase realizations are computed as shown by equation (5.20).

As long as the atmospheric seeing conditions and the average residual variance stay similar, $\tilde{\phi}_{\text{resi}}(\mathbf{f})$ and thus the SCCs should also stay constant. In our simulations that has been shown to be true.

In addition, as mentioned, we found that only a single realization of $\hat{\phi}(\mathbf{x})$ (using equation (5.20)) was enough. Indeed, using more realizations did not change the $\hat{\xi}_i$ significantly. This is possible since we studied high order systems providing many measurements (large N).

5.4.4 Update of command matrix with modal sensitivity compensation

At the beginning of the algorithm we initialize the SCCs to a value of one. The reconstruction matrix is obtained conventionally: a pseudo-inverse with a truncated

SVD is made for the interaction matrix containing the measurements of each applied mode.

Thus, the reconstruction is obtained as

$$\mathbf{c}(k) = B^{\dagger}\mathbf{s}(k), \tag{5.25}$$

where $\mathbf{s}(k)$ is the P-WFS measurement at time step k organized into a vector of N elements and $B^{\dagger}$ is the $M \times N$ command matrix (M being the number of controlled modes, N the number of the measurements).

As a first order approximation, we assume the SCCs are mutually uncorrelated. Thus, each modal reconstruction coefficient is corrected independently and the improved reconstruction can be described by a matrix operation,

$$\begin{bmatrix} c'_1(k) \\ \vdots \\ c'_M(k) \end{bmatrix} = \begin{bmatrix} \hat{\xi}_i & & \\ & \ddots & \\ & & \hat{\xi}_M \end{bmatrix} B^{\dagger}\mathbf{s}(k), \tag{5.26}$$

where $c'_i(k)$ are the corrected modal reconstruction coefficients at time step k and $\hat{\xi}_i$ are the corresponding SCCs.

The updated command matrix (denoted in the following as $B^{\dagger}_m(k')$) is thus $B^{\dagger}$ multiplied by a diagonal matrix with SCCs at its diagonal.

5.4.5 Optimal control

The use of SCCs as a part of closed-loop operation is illustrated in figure 5.12. At first, the WFS measurements are transformed into a modal space as shown in equation (5.26). Then, the modal coefficients are fed to a dynamic controller $h_c(z)$ (we tested both a simple integrator and a modal predictive controller) to obtain the modal DM commands $y_i(k)$. Finally, as explained in Section 3.2, these must be mapped to the corresponding actuator commands using a matrix operation,

$$\begin{bmatrix} u_1(k) \\ \vdots \\ u_{N_a}(k) \end{bmatrix} = Z \begin{bmatrix} y_1(k) \\ \vdots \\ y_M(k) \end{bmatrix}, \tag{5.27}$$

where matrix Z of size $N_a \times M$ (N_a being the number of actuators) is designed (as explained in Section 3.2) to map the M modal coefficients into a vector containing the actuator voltages.

As far as we know, no results concerning an optimal modal control of an AO loop specifically with P-WFS has yet been published. Suggestions for an optimal control exist, for OMGI (discussed in Section 3.3.2), modal prediction with a higher order dynamics (see Section 3.3.3) or minimum variance control based on state-space formulation (see Section 3.3.4). These methods, however, do not take into account any sensor specific features and assume the linearity of the wavefront sensor.

Typically, optimality means minimizing the residual variance and is achieved by adjusting the controller parameters given that the only error source is Gaussian noise added on to the sensor measurements. The system time lag is taken into account

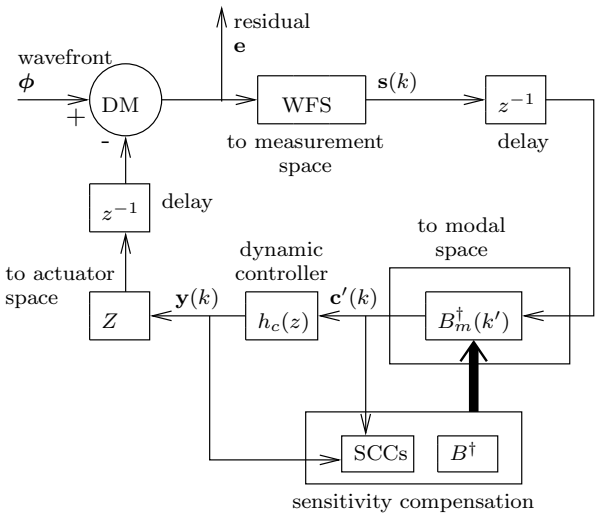

Figure 5.12: Illustration of a closed-loop AO system with sensitivity compensation (Korkiakoski et al., 2008).

and the Kalman filter based approaches also use a model of the incoming turbulence statistics.

However, when these general control algorithms are applied as such for conventionally calibrated P-WFS, they give inferior results. This happens since the seeing dependent measurement reduction is not taken into account.

Nevertheless, when the P-WFS based modal reconstruction is corrected with the sensitivity compensation, applying more advanced modal control techniques becomes possible. In this study we have chosen to demonstrate (due to an easy implementation) the use of a modal predictive controller as described in Section 3.3.3. This takes into account the loop delay and measurement noise and — when used with a Shack-Hartmann WFS — is shown in simulations to be very near to the optimum (Le Roux et al., 2004).

5.5 Simulation of sensitivity compensation

We made a set of end-to-end AO simulations to study the properties of the control algorithm. We studied a similar 8 meter telescope and turbulence model used also for the JR simulations. However, some differences were necessary to run more realistic simulations: the pupil resolution was increased to 640×640 and the number of simulated time steps was 3000. In addition, the number of controlled actuators and modes was increased to 1377 and 1020 respectively. When the P-WFS beam interferences at the CCD detector were simulated (i.e., the PMA method used, see Section 5.4.3), the pupil separation was $3.0 \times$ pupil diameter.

We did all our simulations without simulating photon or read-out noise, misalignments or other error sources (e.g., imperfection of the pyramid prism). In addition, the model $m_j(\,\cdot\,)$ we used in equation (5.23) was identical to what we used when actually simulating the P-WFS.

In all our simulations using the predictive control we chose the number of con-

troller parameters as $p = 4$, $q = 3$ (see Section 3.3.3 for the definition of the parameters). These were found as reasonable numbers since any increase of them made no visible improvement. We also restricted the maximum number of samples used in the optimal control parameter estimation to 500. This was done to make sure that the P-WFS anomalies at the nonlinear regime (before the loop stabilizing) cause no problems. However, we found that the predictive control was very robust and the restriction had only small effects.

5.5.1 Algorithm operation

At first, we illustrate the effect of the SCCs. We simulate the XAO case of the 8 meter telescope with a seeing $r_0 = 0.05$ m at 0.5 μm and use the PMA case for the P-WFS. In this section we consider controlling the loops only with the simple integrator having a single optimized loop gain.

The interval $[k_1,\ k_2]$ needed in equations (5.16) and (5.17) is chosen such that at most 500 time steps are used and the start of the loop is skipped. Thus, k_2 is the current time step index and k_1 is $\max(50,\ k_{\text{end}} - 500 + 1)$.

In figure 5.13 we show the short exposure Strehl ratio at 1.6 μm as a function of time in simulation with and without the use of SCCs. We also show the points at which the re-computation of the SCCs is done.

It can be seen that the Strehl ratio is increased roughly from 0.1 to 0.3 by the use of the SCCs. When using the SCCs the loop "closes" slower, but as soon as the correct SCCs are found, the performance increases dramatically. The differences at the start are due to the fact that the used loop gains (0.6 and 3.2) are optimized for the final performance and the default SCCs are set to one.

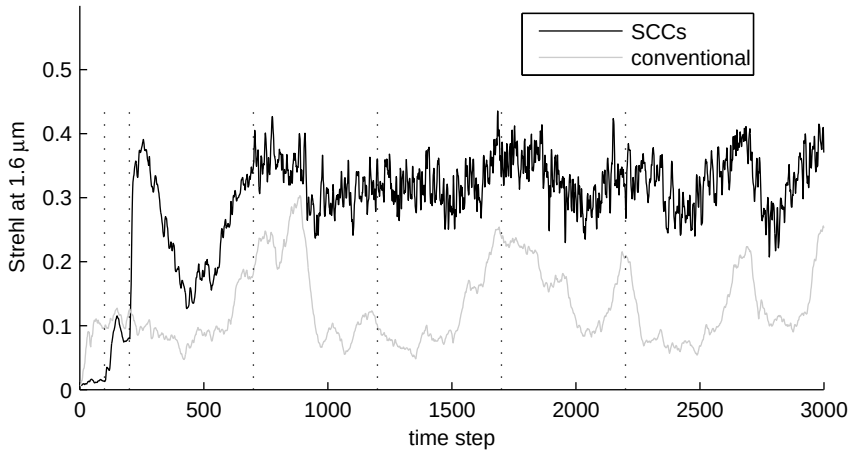

Figure 5.13: Loop convergence with and without SCCs. The simulations are made with a simple integrator using optimized loop gains (0.6 with SCCs and 3.2 with conventional command matrix) giving corresponding Strehl ratios of 0.32 and 0.06. The vertical lines show the positions at which the SCCs are recomputed. Both cases are made with $r_0 = 0.05$ and the P-WFS is simulated with PMA. (Korkiakoski et al., 2008).

In figure 5.14 we illustrate the accuracy and evolution of the residual PSD estima-

tion (in the simulation with SCCs). It can be seen that outside the cutoff frequency $1/(2d)$ the estimated and actual PSD match always quite well, but the low spatial frequencies are underestimated. At low frequencies the first PSD estimate is on the average roughly 100 times lower than the actual one, but the difference with the latter estimates is less than 10 times. This is due to the greater measurement accuracy after the SCCs have been computed.

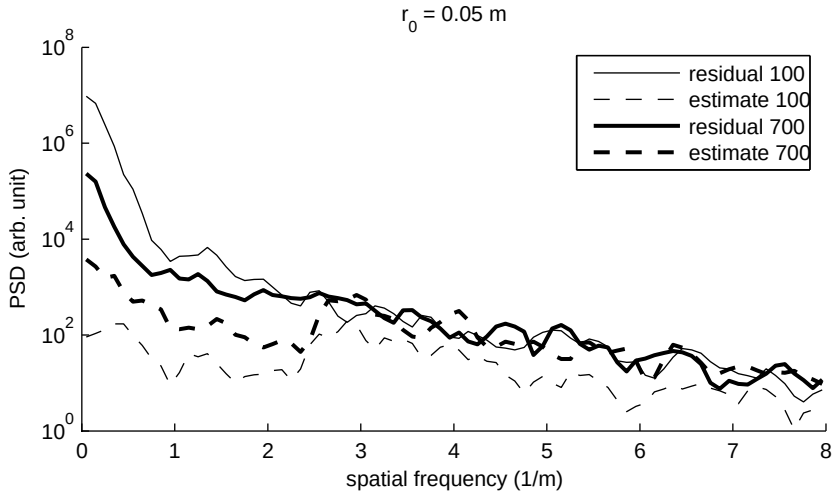

Figure 5.14: Radially averaged PSDs of the residuals and their estimates. The thin plots are made at time steps 100 and the thick plots at time steps 700. The simulation was made with $r_0 = 0.05$ m and the P-WFS is simulated with PMA. (Korkiakoski et al., 2008).

In figure 5.15 we show the values of the SCCs as a function of mode at different computation steps. To concentrate on the most interesting properties, we show the SCCs for modes 1–150 — for higher order modes the plots merely follow the shown trend. Three different seeing values are considered (r_0 being 0.05, 0.08, 0.10 m).

It can be seen that at $r_0 = 0.05$ m the first computation gives descending values starting from about 8. At the last mode (1020) they reach a value of 2.5. At $r_0 = 0.10$ m the corresponding range is 3.2–2. The next steps increase the SCCs, especially at the lower modes. At $r_0 = 0.05$ m the range converges approximately to 40–4.5, at $r_0 = 0.10$ m to 6–2.4. After the third computation the SCCs remain stable — on average the variations are 2–5%. The SCCs of the lowest modes (1–5), however, can have larger variations (5–11%).

To conclude, the iterative approach to compute the SCCs is very efficient, only a few iterations are required to obtain relatively stable values. In addition, as seen in the Strehl-plot in figure 5.13, the control is not very sensitive to the incorrect values of SCCs — even the first SCC computation is helping to increase the Strehl a lot. The AO loop control relying on the reconstruction using the SCCs is also robust. The SCC variations up to 10% cause no notable changes to the short exposure Strehl ratio and the repeated SCC re-computations make no stability problems.

The pace at which the SCCs are re-computed is not critical, as long as it is done frequently enough to compensate the change of seeing. However, in all our following simulations we have re-computed the SCCs at the same time steps as shown in figure

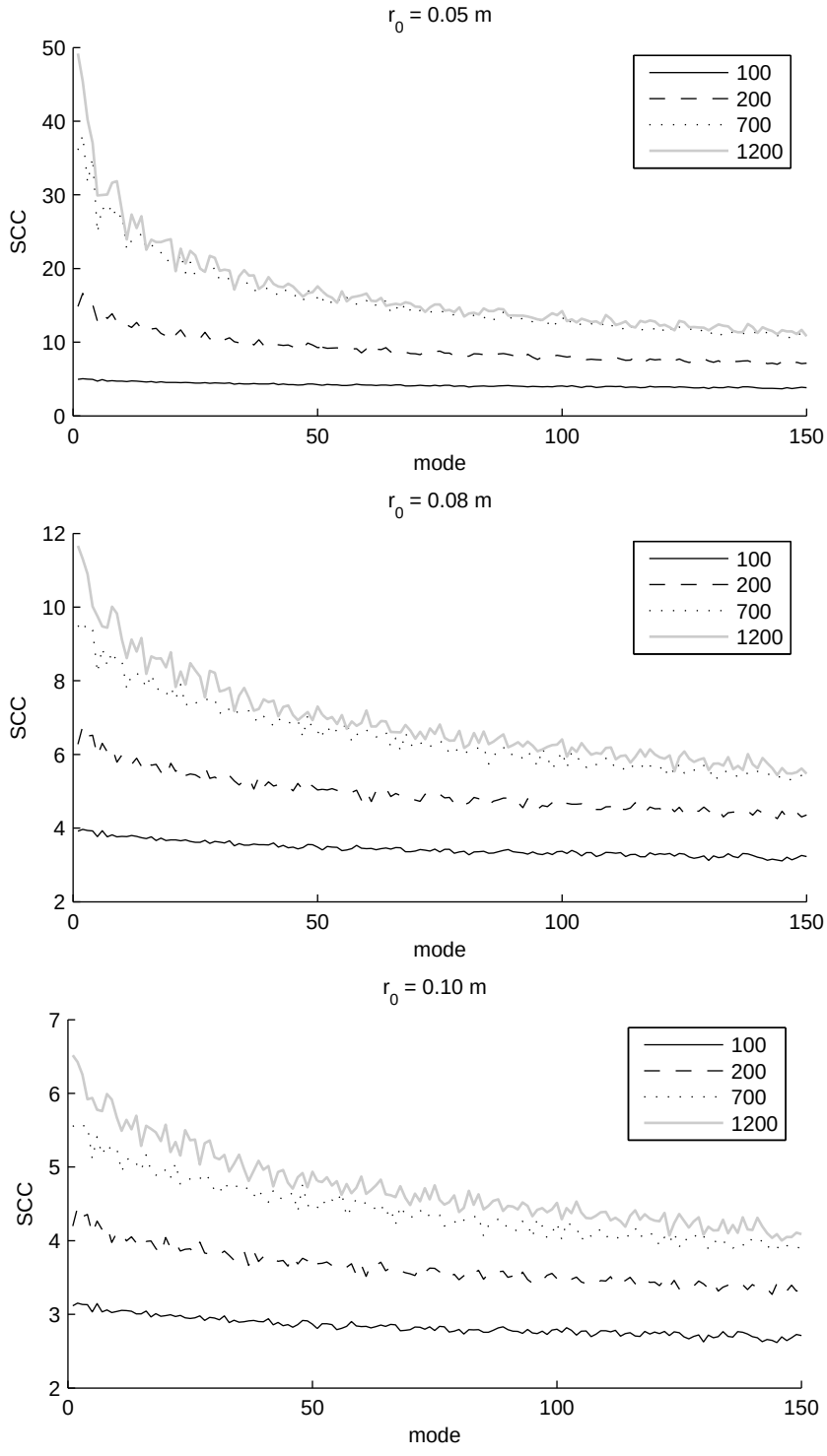

Figure 5.15: SCCs for the first 150 modes. The coefficients are shown at time steps 100, 200, 700 and 1200. The simulations are made with three seeing values (r_0 being 0.05, 0.08 and 0.10 m) and using the PMA case with the P-WFS. As a controller here a simple integrator is used with optimized loop gains. (Korkiakoski et al., 2008).

5.13.

5.5.2 Performance

SCCs without noise

Next, we made extensive simulations at three seeing levels (r_0 being 0.05, 0.08 and 0.10 m) with both the AMA and PMA cases. In figure 5.16 we show the long exposure Strehl ratio as a function of loop gain and also the Strehl ratio when the modal predictive control is applied.

The optimal Strehl ratios in the given cases are also summarized in Table 5.3 (four upper rows).

Table 5.3: Optimal Strehl ratios at 1.6 μm

sensor	control	$r_0 = 0.05$ m	$r_0 = 0.08$ m	$r_0 = 0.10$ m
AMA	PI[a]	0.55	0.80	0.88
AMA	predictor	0.60	0.82	0.89
PMA	PI[a]	0.32	0.75	0.87
PMA	predictor	0.37	0.80	0.88
Without temporal error				
AMA		0.65	0.85	0.90
PMA		0.45	0.83	0.90

[a]Simple integrator with optimized loop gain

From these results, we highlight the following points:

- The Strehl ratio as a function of loop gain depends a lot on the seeing. Without SCCs the optimum is obtained at gains between 1 and 3.5, but when SCCs are used the phenomenon is far less important. The optimal gain is always about 0.7.
- The SCCs help to increase the optimal Strehl ratio even without the predictive control. Depending on the seeing and sensor, the increase is 0.05–0.40. Especially in bad seeing the increase is significant.
- The modal predictive control increases the Strehl ratio an additional 0.01–0.05. This increase is also more notable in bad seeing.
- The P-WFS simulated with AMA has a better performance compared to the PMA case. Depending on the seeing and control, the difference is 0.006–0.22. Especially in bad seeing the sensor without sub-beam interferences gives significantly better results.

The P-WFS gives the better results the more independent the sub-images at the CCD detector are. It can be mentioned that we tested the PMA case using also other pupil separations. When increasing the distances of the sub-images, the P-WFS performance with PMA slowly approaches the AMA case where all cross-pupil

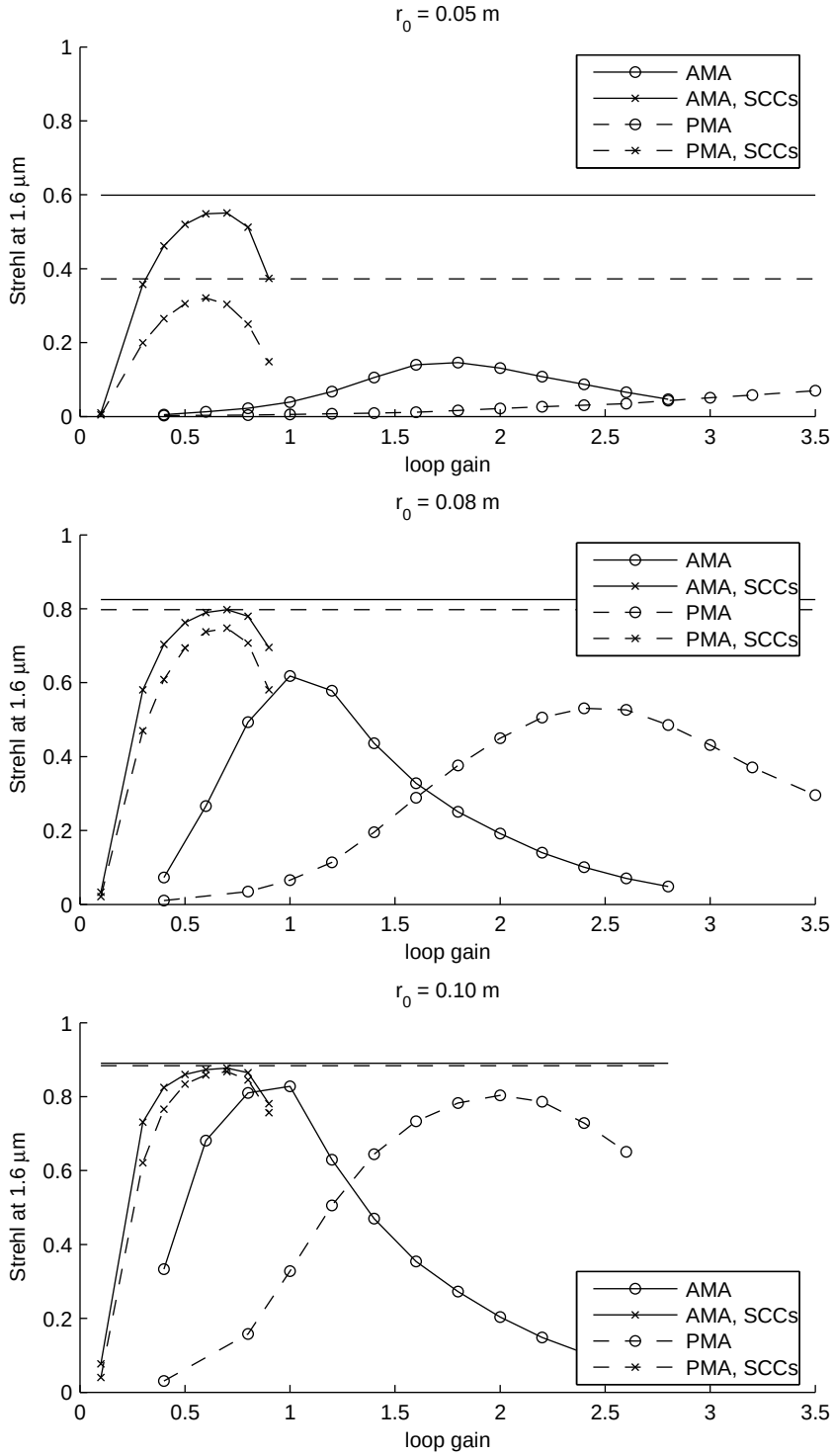

Figure 5.16: Typical Strehl ratios as function of loop gain at several seeing levels (r_0 is 0.05, 0.08 and 0.10 m). Solid lines are made without the sub-beam interferences (AMA) and dashed lines with the PMA case. Lines with markers are made with the simple integrator (x-markers with the SCCs, o-markers without the SCCs). The horizontal lines without markers show the Strehl ratio level when the modal predictive control is applied with SCCs. (Korkiakoski et al., 2008).

diffraction effects are neglected. The separation (center to center), however, have to be more than 5 times the corresponding pupil diameter to get close to the ideal level also in bad seeing ($r_0 = 0.05$ m).

In addition, we compute the Strehl ratios in cases where the turbulence is not evolving (a static phase screen). This illustrates an ultimate upper limit for the AO loop control. Averages of five independent screens are shown in Table 5.3 (two lower rows). The loss in Strehl ratio due to temporal error (0.01–0.08) is significant only in bad seeing. At $r_0 = 0.08$ m the temporal error means a loss of 0.03 in Strehl ratio, at $r_0 = 0.10$ m the loss is 0.01–0.02.

Thus, in most cases the combined use of the SCCs and the modal predictive control is efficient enough to keep the AO loop relatively close to its sensor specific ideal performance.

It can be also mentioned that when using a theoretical linear sensor as described before (P-WFS model linearized by replacing the sinusoids by their first order Taylor polynomials), the Strehl in bad seeing is not decreasing as much as shown in Table 5.3. At $r_0 = 0.05$ m with the predictive control the Strehl ratio would be 0.73 (0.08 better than AMA without temporal error) and at $r_0 = 0.08$ m it would be 0.87 (0.02 better than AMA without temporal error). This suggests that while being extremely helpful, the use of the SCCs is still unable to remove all the nonlinearity effects present in a nonmodulated P-WFS.

5.6 Conclusions of P-WFS control

5.6.1 Success of sensitivity compensation

In the previous section, it has been shown that the performance of a nonmodulated P-WFS can be significantly improved by compensating the sensitivity of the measured modes.

When calibrated conventionally (i.e., interaction matrix created by recording measurements of the DM modes — without turbulence residuals — at the linear regime of the sensor), the considered system was working well in good conditions (seeing $r_0 > 0.10$ m at 0.5 μm and sensing wavelength $\lambda_{\mathrm{WFS}} > 0.5$ μm). Strehl ratios over 0.85 at 1.6 μm were obtained. However, in worse seeing ($r_0 = 0.05$ m) the performance collapsed to below 0.10. Nevertheless, in such difficult cases the sensitivity compensation was capable of increasing the Strehl ratio by 0.30–0.40 (to 0.60 with AMA and 0.37 with PMA).

The enormous improvement is possible since the high frequency components in the residual phase affect differently the sensitivity with which each mode is measured. For instance, our simulations indicate that in bad seeing at $r_0 = 0.05$ m, the lowest modes (tip and tilt) can have a measurement up to 40 times smaller than their real value. Without adjusting these modal sensitivity differences it becomes impossible to control efficiently an AO loop by adjusting a single loop gain.

It is also demonstrated that the modal predictive control can be successfully applied with a nonmodulated P-WFS as long as the loss of sensitivity is compensated. This gives an additional improvement of 0.01–0.05 in Strehl ratio and — even more important — makes it easy to control a P-WFS optimally in all seeing conditions.

Although not explicitly simulated, the results shown here indicate that using a P-WFS based AO system in rapidly varying seeing conditions is possible. As long as the seeing gets correctly estimated, the wavefront reconstruction can be consequently adjusted to give a good performance. We have shown that at least 500 samples (0.5 s) are enough to successfully represent the seeing level.

In addition, it can be noted that the sensitivity compensation algorithm outperforms even the Jacobian reconstruction. This can be explained by the fact that the JR — even in its iterative form — is effectively unable to combine the (a priori) information of the residual PSD and the wavefront sensor nonlinearity properties.

However, we cannot totally exclude the possibility that the numerical iteration of equation (5.11) tends to converge to a local minimum. This would cause the iterative JR reconstruction to give slightly worse estimates compared to an ideal theoretical reconstruction. This could perhaps be avoided by using more effective algorithms for solving the nonlinear equation.

5.6.2 Practical issues

The sensitivity compensation as used here is directly applicable to a real-time AO application. It requires explicit knowledge only from a few well known system dependent parameters: P-WFS model (basically the pupil separation) and the phase shapes of the controlled mirror modes.

The additional real time computation requirements of the SCCs are not demanding. As the update of SCCs is required only after a significant change in seeing conditions, their computation does not have to be real-time. Nevertheless, if the model in equation (5.23) is computationally heavy, some effort must be made such that the coefficient computation takes only a fraction of a minute.

At least two things can significantly ease these efforts: the computations can be parallelized. Each mode is handled independently and if enough parallel computational units are available, the computation time can be reduced to a fraction of its serial version. Besides, as the dependency of the SCCs with mode number is known and observed to be relatively smooth (see figure 5.15), only a fraction (10% to 20% for instance) of well chosen SCCs needs to be evaluated with the wave-optics code; the other SCCs can then be computed by interpolation, saving thus a large part of computing power needed. In addition, also a lookup table mapping predefined values of r_0 to corresponding SCCs can be considered.

We believe that the accuracy of the modeled parameters is not critical. For instance, at $r_0 = 0.05$ m the compensation coefficients can vary easily by 10% (between different re-computations after reaching the steady state) without any significant effect in the Strehl ratio. In addition, the application of the sensitivity compensation is robust by nature: due to the P-WFS saturation properties there is a minimal risk of loop instability caused by using too large SCCs.

It should also be mentioned that we have considered here only a monochromatic case. If the spectral bandwidth of the P-WFS sensing wavelength is — in a real system — significantly increased (especially towards shorter wavelengths), this must be taken into account. Jacobians will need to be adapted to multichromaticity by averaging Jacobians at different wavelengths covering the spectral domain. Also

the P-WFS internal model in the SCC computation will need the corresponding modifications.

However, the work presented here is only the first step in studying the P-WFS control with the sensitivity compensation. A deeper study is required to analyze in more detail the impact of several error sources on the used algorithms — and the sensitivity compensation method must be extended to include these error sources. Those include, for instance, photon and detector noise, pyramid misalignments, pyramid prism manufacturing defects and inaccuracies in the mirror modes determination.

In addition, it can be pointed out that the sensitivity compensation method described here can be applied to any other wavefront sensor whose internal model is known. It could be especially straightforward — and useful — for the P-WFS with modulation, but also a quad-cell Shack-Hartmann could perhaps benefit from the approach applied here.

Chapter 6

Future work and conclusions

In this final chapter the direction of our future work is briefly introduced in Section 6.1. This includes, for instance, investigating in more detail the impact of noise for the sensitivity compensation and also simulations for the ELTs.

Finally, in Section 6.2, the most important conclusions of this thesis are summarized.

6.1 Future work

Noise impact

When dealing with noisy P-WFS signals, we have still a few issues to clarify. For instance, it has been observed that subtracting the reference signal (non-zero measurement for a flat incoming wavefront due to the interference term) from the P-WFS measurement is not always the optimal way. In fact, to reach an optimum, a condition dependent sensitivity adjustment gain must be applied to the reference. In other words, instead of computing the P-WFS signal as

$$\mathbf{m}(\phi(\mathbf{x})) = \begin{bmatrix} m_1\big(\phi(\mathbf{x})\big) \\ \vdots \\ m_N\big(\phi(\mathbf{x})\big) \end{bmatrix} - \begin{bmatrix} m_1\big(0\big) \\ \vdots \\ m_N\big(0\big) \end{bmatrix}, \tag{6.1}$$

better results would be obtained with

$$\mathbf{m}(\phi(\mathbf{x})) = \begin{bmatrix} m_1\big(\phi(\mathbf{x})\big) \\ \vdots \\ m_N\big(\phi(\mathbf{x})\big) \end{bmatrix} - \beta \begin{bmatrix} m_1\big(0\big) \\ \vdots \\ m_N\big(0\big) \end{bmatrix}, \tag{6.2}$$

where β is the scaling factor optimized for current conditions and $m_i\big(\cdot\big)$ describes the process how the ith measurement element is obtained from the detector intensities (see Section 5.1 for more details). However, this is a problem only for the P-WFS as modeled by the PMA method (see Section 5.1.1) — the reference measurement of the AMA method is zero, in the case the non-common path aberrations are null. In the presence of the non-common path aberrations, sensitivity compensation must be applied also to the reference signal for both PMA and AMA cases. In this case the

β-factor becomes a parameter $\beta(i)$ that depends on the content of the non-common path aberrations in terms of controlled modes.

This issue of the reference subtraction is not studied in the context of this thesis, but will be an important topic of our future work.

A few preliminary simulation results with a non-optimal β are shown in Table 6.1. There we compare the Strehl ratio of a nonmodulated P-WFS (conventional and sensitivity compensated) to the well known Shack-Hartman WFS working without spatial filtering. The P-WFS has the same parameters as used in Section 5.5.2 and the SH-WFS is chosen to give the same number of measurements. The conventional P-WFS is controlled with an optimized simple integrator, the P-WFS with SCCs and the SH-WFS use the modal predictor. The seeing is bad ($r_0 = 0.05$ m).

Table 6.1: Optimal Strehl ratios at 1.6 μm

	P-WFS[a], conventional	P-WFS[a], SCCs	SH-WFS[b]
10 photons[c]	0.08	0.43	0.47
13 photons[c]	0.09	0.44	0.49

[a] $\beta = 0$
[b] field of view per subaperture 2.4", 8×8 CCD pixels per subaperture
[c] Photons per subaperture per frame (1 ms)

It is seen that the use of SCCs is dramatically improving the P-WFS results also in the presence of noise. However, the optimal performance is not obtained and SH-WFS slightly outperforms the P-WFS in the shown cases. This happens both because the reference subtraction is not optimized and because the sensitivity compensation method is not yet extended to handle noisy measurements.

Preliminary simulations with ELTs

In the previous text we have illustrated our P-WFS simulations with an 8 meter telescope and a typical XAO system.

As well as the shown XAO case, we also tested a SCAO system with the same 8 meter telescope, but used a coarser resolution (16×16) corresponding to 0.5 meter subapertures. Also that system was improved by the sensitivity compensation, although the improvement (1–3% in Strehl ratio at 1.6 μm) was not as dramatic as in the XAO cases. A more thorough study would be appropriate to clarify this issue.

For the next generation AO systems, it would be also interesting to see how the P-WFS performs with ELTs. Next we briefly illustrate these emerging issues.

We chose to simulate a 42 meter ELT system with the same resolution corresponding to 0.5 meter subapertures. We also used the same turbulence profile and phase sampling (16 simulation pixels per "subaperture") as before. The measurement resolution was 84×84, number of actuators 5797, and we controlled 4347 modes. No central obstruction was modeled.

It turned out that the nonlinearity issues with the bigger telescope were more serious compared to the 8 meter case. Thus, we were not able to close the loop with

$r_0 = 0.10$ m, $\lambda_{\mathrm{WFS}} = 0.7$ μm and a nonmodulated P-WFS. These problems might also be related to the reference subtraction issue mentioned in the previous section.

However, we used a bit higher sensing wavelengths (0.9–1.6 μm) to be able to close the loop. With the shortest wavelength (0.9 μm), the performance could be slightly improved by the use of the SCCs. Those results are visualized in figure 6.1. Only the cases 0.9 μm and 1.6 μm are illustrated, the other results are between the shown plots.

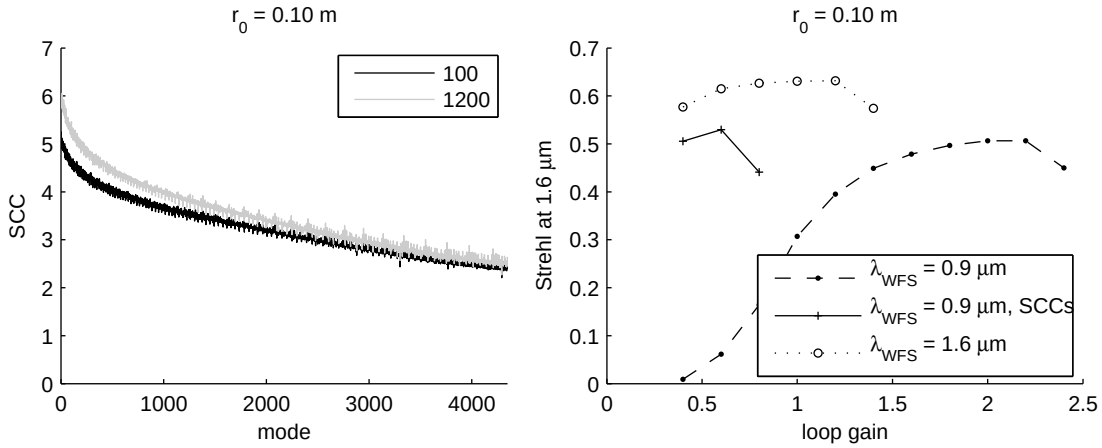

Figure 6.1: Sensitivity compensation demonstration for a 42 meter telescope having a measurement resolution of 84×84. We use here the PMA method, r_0 is 0.10 m and photon flux is 1000 photons/subaperture/frame. Left: SCCs for a sensing wavelength of 0.9 μm (at time steps 100 and 1200). Right: Strehl ratio as a function of loop gain. The conventional reconstruction is shown for sensing wavelengths 0.9 μm (dashed line) and 1.6 μm (dotted line, circle markers). SCCs are used for $\lambda_{\mathrm{WFS}} = 0.9$ μm (solid line).

It can be seen that also here the SCCs are not helping as dramatically as in the XAO case. The optimum Strehl ratio of the conventional reconstruction (0.51) can be increased only to 0.53. The range of the final SCCs is roughly 6–2.5. When compared to our XAO simulations, it can be mentioned that a comparable SCC range was able to increase the Strehl ratio from 0.80 to 0.87.

It is also seen that the optimum Strehl ratio (0.53) obtained at $\lambda_{\mathrm{WFS}} = 0.9$ μm is significantly lower compared to what is obtained at $\lambda_{\mathrm{WFS}} = 1.6$ μm (0.63). This is due to the larger wavefront distortions at shorter wavelengths.

Indeed, these simulations suggest that a system having a rather low measurement resolution (0.5 meter subapertures) does not benefit very much from the use of the SCCs — efficient nonlinearity compensation would require an XAO system. Nevertheless, the SCCs are still helping to keep the loop gain dependency predictable. In this case, the optimal Strehl with SCCs is obtained with a gain of 0.6, but without SCCs the optimum gain is 2.2. It is also worth noting that no instability issues with the sensitivity compensation were seen.

Our study with the ELTs is however only a preliminary step and leaves out a few interesting questions. Besides the issues mentioned before, a few important simulation subjects of our further research are briefly listed here:

- The sensitivity compensation should be tested with a modulated P-WFS. In principle, this is very straightforward: only the P-WFS model is slightly modified. The results would be interesting especially for the ELTs. Nevertheless, such a study is computationally extremely demanding and we have postponed it until our AO simulation cluster can be upgraded.

- To carry out the sensitivity compensation simulations with XAO systems on ELTs, a significant optimization of our simulation code is required. In the current implementation the memory requirements of the P-WFS wave optics model (FFT computation) would exceed the capacity of the cluster. The low order SCAO simulations shown in figure 6.1 are at the limit of our current simulation capabilities.

- The effect of the central obstruction must be studied with the sensitivity compensation. This has already been reported earlier to be a problem with a nonmodulated P-WFS (Le Louarn et al., 2004b). Also other aperture obstructions (like the secondary mirror supports, "spiders", in the ELTs) can have an effect on the P-WFS performance.

6.2 Conclusions

The conclusions of this thesis are summarized next.

The wavefront reconstruction and control of adaptive optics have been the main topic in this thesis. In particular, we have concentrated on two specific regimes: wide field imaging using GLAO as it will be used by MUSE and Hawk-I at the VLT and high resolution imaging of very small fields using XAO, which is of great interest for instruments like SPHERE or EPICS.

We have studied the performance of typical AO systems in these cases using ESO's numerical Monte Carlo simulation tool, OCTOPUS. To carry out the study, new functionalities were implemented for OCTOPUS (for instance, code to accomplish the calculations required for the modal approaches and to simulate more realistic phase evolution). These additions, as well as the major properties of OCTOPUS, are described in the text and in given references.

Concerning GLAO, we have demonstrated its performance by showing several examples in various cases. We studied the optimality of the conventional control algorithms (with SH-WFSs) in cases having asymmetric guide star patterns and dim reference objects. We also studied the GLAO performance in ELTs and the effect of the subaperture size. We concluded that that the control of GLAO is robust and its usefulness in all the studied cases is obvious. In addition, this can be achieved without additional advanced control techniques in most realistic cases.

Concerning XAO, we have concentrated on the nonlinearity issues of the pyramid sensor, known to be potentially a superior choice for the next generation XAO systems. The work developed in this frame led to two articles published in a refereed journal. We have mostly restricted our study to the cases where the nonlinearity properties are most prominent: no modulation, bad seeing and short sensing wavelengths. As a first step, we studied only an 8 meter telescope with a measurement resolution of 40×40.

At first, a novel approach has been presented to evaluate and overcome the P-WFS nonlinearity issues. We have described an iterative, model based, reconstruction method that, in principle, can be used to compute the wavefront reconstruction at arbitrary accuracy. This is achieved by successive linearizations of the model, represented as Jacobian matrices.

The reconstruction method, referred in the text as the Jacobian reconstruction, however, requires an exact model of the used sensor and has far too high computation requirements for current real-time applications. Nevertheless, while being a rather theoretical approach, the simulations using the Jacobian reconstruction show that in closed-loop AO operation the nonlinearity effects of P-WFS can be compensated by only a small amount compared to a well optimized linear reconstruction.

The well optimized linear reconstruction, on the other hand, is not achieved by the conventional way to calibrate a pyramid sensor, that is, measure a set of mirror modes in a linear regime, compile an interaction matrix and invert it.

Thus, we propose in the text a heuristic method to create an improved linear reconstruction. We use the knowledge that in the presence of large phase distortions the P-WFS measurements of certain modes tend to get reduced. This reduction is heavily dependent on the mode. We combine the knowledge of the turbulence (von Karman power law, strength of seeing obtained from WFS measurements) and a model of the sensor. This leads to iteratively improving reconstruction matrices and we have shown that the method efficiently compensates the loss of sensitivity.

In the XAO cases we studied, the sensitivity compensation was able to dramatically improve the performance in the most difficult conditions. In addition, other beneficial effects include having more foreseeable loop gain dependence and a possibility to use modal predictive control with P-WFS.

One of the most important conclusions of this thesis is that we have shown that the P-WFS nonlinearity effects can be efficiently compensated. This has a significant importance for all the high resolution AO systems based on P-WFS. Currently only one such system is being constructed: the first light AO instrument for the LBT (Esposito et al., 2006). The work shown in this thesis could be directly applied to that system.

In addition, the future pyramid sensor based XAO instruments, like EPICS, will benefit from this work. We have now demonstrated the importance of the P-WFS sensitivity compensation for small XAO systems. If the illustrated algorithm works as well for the larger XAO instruments on the ELTs, the result would be of extreme importance to the next generation planet finder instruments.

Thus, the suitability of the P-WFS for the ELTs is one of the main topics that will be developed in our future works. In particular, we are interested whether the sensitivity compensation is useful with a modulated P-WFS.

Appendix A

Pyramid signal

In the following the pyramid wavefront sensor Fourier optics model is described as derived in (Korkiakoski et al., 2007b). The complex amplitudes at the detector plane (illustrated in figure 5.1) can be written as

$$\Psi_p(\mathbf{r}') = \Psi(\mathbf{r}') * \mathscr{F}^{-1}\{T_{\mathrm{pyr}}(\mathbf{f}')\}, \tag{A.1}$$

where $\Psi(\mathbf{r}') = P(\mathbf{r}')\exp(i\phi(\mathbf{r}'))$ is the complex amplitude in the pupil plane ($P(\mathbf{r}')$ being the aperture function) and $T_{\mathrm{pyr}}(\mathbf{f}')$ is pyramid transmittance function given as

$$\begin{aligned} T_{\mathrm{pyr}}(\mathbf{f}') &= \sum_{n=0}^{1}\sum_{m=0}^{1} T_{n,m}(\mathbf{f}) \\ &= \sum_{n=0}^{1}\sum_{m=0}^{1} H((-1)^n f_x', (-1)^m f_y') \exp\left\{-i\alpha\left[(-1)^n f_x' - c + (-1)^m f_y' - c\right]\right\}. \end{aligned} \tag{A.2}$$

Here $H(x,y)$ is the two dimensional Heaviside function ($H(x,y) = 1$, when x and $y > 0$ and zero otherwise), α is tangent of the pyramid divergence angle (as defined in (Arcidiacono, 2005; Riccardi et al., 1998)) and c is half of the distance between two opposite pyramid corners. Thus, the complex amplitudes can be written as

$$\Psi_p(\mathbf{r}') = \sum_{n=0}^{1}\sum_{m=0}^{1} \Psi_{n,m}(\mathbf{r}'), \tag{A.3}$$

where

$$\Psi_{n,m}(\mathbf{r}') = \Psi\left(x' - (-1)^n\frac{\alpha}{2\pi}, y' - (-1)^m\frac{\alpha}{2\pi}\right) * \mathscr{F}^{-1}\{H(\mathbf{f})\}\left((-1)^n x', (-1)^m y'\right), \tag{A.4}$$

where the Fourier transform of the Heaviside function is

$$\begin{aligned} &\mathscr{F}^{-1}\{H(\mathbf{f})\}\left((-1)^n x, (-1)^m y\right) = \\ &\quad \frac{1}{4}\delta(x,y) - \frac{(-1)^{n+m}}{4\pi^2} p.v.\frac{1}{xy} + \frac{i}{4\pi}\left[(-1)^n\left(p.v.\frac{1}{x}\delta(y)\right) + (-1)^m\left(\delta(x)p.v.\frac{1}{y}\right)\right] \end{aligned} \tag{A.5}$$

with $p.v.$ denoting the principal value. The intensity at the detector plane is

$$\begin{aligned} I_p(\mathbf{r}') &= \Psi(\mathbf{r}')\Psi^*(\mathbf{r}') \\ &= \sum_{n=0}^{1}\sum_{m=0}^{1}\Psi_{n,m}(\mathbf{r}')\Psi^*_{n,m}(\mathbf{r}') + 2\sum_{n=0}^{1}\sum_{m=0}^{1}\sum_{\substack{n'=0\\n'\neq n}}^{1}\sum_{\substack{m'=0\\m'\neq m}}^{1} Re\left[\Psi_{n,m}(\mathbf{r}')\Psi^*_{n',m'}(\mathbf{r}')\right]. \end{aligned} \tag{A.6}$$

When assuming that the four waves are far from each other, the interferences between them can be neglected. Then intensity becomes

$$I_p(\mathbf{r}') \approx \sum_{n=0}^{1}\sum_{m=0}^{1} I_{n,m}(\mathbf{r}'), \tag{A.7}$$

where

$$I_{n,m}(\mathbf{r}') = \Psi_{n,m}(\mathbf{r}')\Psi^*_{n,m}(\mathbf{r}') \tag{A.8}$$

are the intensities in each quadrant. The pyramid sensor measurement is obtained by dividing the detector plane into four sections and combining the intensities as shown in equation 5.1. When substituting equations (A.8), (A.4) and (A.5) into equation (5.1), the pyramid measurement signal can be written as

$$\begin{aligned} I_tS_x(x,y) = -\frac{1}{\pi}\Bigg\{ & R_\Psi(x,y)\left[I_\Psi(x,y) * \left(p.v.\frac{1}{x}\delta(y)\right)\right] \\ & -I_\Psi(x,y)\left[R_\Psi(x,y) * \left(p.v.\frac{1}{x}\delta(y)\right)\right]\Bigg\} \\ -\frac{1}{\pi^3}\Bigg\{ & \left[R_\Psi(x,y) * p.v.\frac{1}{xy}\right]\left[I_\Psi(x,y) * \left(\delta(x)p.v.\frac{1}{y}\right)\right] \\ & -\left[I_\Psi(x,y) * p.v.\frac{1}{xy}\right]\left[R_\Psi(x,y) * \left(\delta(x)p.v.\frac{1}{y}\right)\right]\Bigg\} \\ I_tS_y(x,y) = -\frac{1}{\pi}\Bigg\{ & R_\Psi(x,y)\left[I_\Psi(x,y) * \left(\delta(x)p.v.\frac{1}{y}\right)\right] \\ & -I_\Psi(x,y)\left[R_\Psi(x,y) * \left(\delta(x)p.v.\frac{1}{y}\right)\right]\Bigg\} \\ -\frac{1}{\pi^3}\Bigg\{ & \left[R_\Psi(x,y) * p.v.\frac{1}{xy}\right]\left[I_\Psi(x,y) * \left(p.v.\frac{1}{x}\delta(y)\right)\right] \\ & -\left[I_\Psi(x,y) * p.v.\frac{1}{xy}\right]\left[R_\Psi(x,y) * \left(p.v.\frac{1}{x}\delta(y)\right)\right]\Bigg\}, \end{aligned} \tag{A.9}$$

where $R_\Psi(x,y) = P(x,y)\cos\phi(x,y)$, $I_\Psi(x,y) = P(x,y)\sin\phi(x,y)$. $P(x,y)$ is the field amplitude and $\phi(x,y)$ is the field phase value. The amplitude $P(x,y)$ is assumed to be a constant P inside of the pupil and zero outside.

Appendix B

Pyramid signal linearization

The formulas for equation (5.3) are derived in (Korkiakoski et al., 2007b) and repeated here. The discretised phase approximation vector $[\phi_1, \cdots, \phi_N]$ is abbreviated in this section as $\boldsymbol{\phi}$.

At first, it can be noted that the measurement of the four-sided pyramid sensor is a sum of the two-sided pyramid sensor measurement (m_x, m_y) and cross-terms (c_x, c_y). Thus, the signal vector can be written as

$$\begin{aligned} S_x^{x_i,y_i}(\boldsymbol{\phi}) &= m_x^{x_i,y_i}(\boldsymbol{\phi}) + c_x^{x_i,y_i}(\boldsymbol{\phi}) \\ S_y^{x_i,y_i}(\boldsymbol{\phi}) &= m_y^{x_i,y_i}(\boldsymbol{\phi}) + c_y^{x_i,y_i}(\boldsymbol{\phi}), \end{aligned} \tag{B.1}$$

where

$$\begin{aligned} m_x^{x_i,y_i}(\boldsymbol{\phi}) &= -\frac{1}{\pi}\Big\{P(x_i,y_i)\cos\phi_{x_i,y_i}C_{\text{sinx}}(x_i,y_i) - P(x_i,y_i)\sin\phi_{x_i,y_i}C_{\text{cosx}}(x_i,y_i)\Big\} \\ m_y^{x_i,y_i}(\boldsymbol{\phi}) &= -\frac{1}{\pi}\Big\{P(x_i,y_i)\cos\phi_{x_i,y_i}C_{\text{siny}}(x_i,y_i) - P(x_i,y_i)\sin\phi_{x_i,y_i}C_{\text{cosx}}(x_i,y_i)\Big\} \\ c_x^{x_i,y_i}(\boldsymbol{\phi}) &= -\frac{1}{\pi^3}\Big\{C_{\text{cosxy}}(x_i,y_j)C_{\text{siny}}(x_i,y_j) - C_{\text{sinxy}}(x_i,y_j)C_{\text{cosy}}(x_i,y_j)\Big\} \\ c_y^{x_i,y_i}(\boldsymbol{\phi}) &= -\frac{1}{\pi^3}\Big\{C_{\text{cosxy}}(x_i,y_j)C_{\text{sinx}}(x_i,y_j) - C_{\text{sinxy}}(x_i,y_j)C_{\text{cosx}}(x_i,y_j)\Big\} \end{aligned} \tag{B.2}$$

having the convolution matrices defined as

$$\begin{aligned} C_{\text{sinx}}(x_i,y_i) &= \iint\limits_{x',y'} P(x',y')\sin\phi_{x',y'}\tfrac{1}{x_i-x'}\delta(y_i-y')\ \mathrm{d}x'\mathrm{d}y' \\ C_{\text{cosx}}(x_i,y_i) &= \iint\limits_{x',y'} P(x',y')\cos\phi_{x',y'}\tfrac{1}{x_i-x'}\delta(y_i-y')\ \mathrm{d}x'\mathrm{d}y' \\ C_{\text{siny}}(x_i,y_i) &= \iint\limits_{x',y'} P(x',y')\sin\phi_{x',y'}\tfrac{1}{y_i-y'}\delta(x_i-x')\ \mathrm{d}x'\mathrm{d}y' \\ C_{\text{cosy}}(x_i,y_i) &= \iint\limits_{x',y'} P(x',y')\cos\phi_{x',y'}\tfrac{1}{y_i-y'}\delta(x_i-x')\ \mathrm{d}x'\mathrm{d}y' \\ C_{\text{sinxy}}(x_i,y_j) &= \iint\limits_{x',y'} P(x',y')\sin\phi_{x',y'}\tfrac{1}{(x_i-x')(y_i-y')}\ \mathrm{d}x'\mathrm{d}y' \\ C_{\text{cosxy}}(x_i,y_j) &= \iint\limits_{x',y'} P(x',y')\cos\phi_{x',y'}\tfrac{1}{(x_i-x')(y_i-y')}\ \mathrm{d}x'\mathrm{d}y'. \end{aligned} \tag{B.3}$$

The terms m_x, m_y, c_x and c_y can be derived in respect to the phase values at each

grid element. The Jacobian matrices of m_x and m_y become relatively sparse,

$$\frac{\partial m_x^{x_i,y_i}(\boldsymbol{\phi})}{\partial \phi_{x_j,y_j}} = \begin{cases} -\frac{1}{\pi}\Big\{ & P\cos\phi_{x_i,y_i}\cos\phi_{x_j,y_j}D_{mx}(i,j) \\ & +P\sin\phi_{x_i,y_i}\sin\phi_{x_j,y_j}D_{mx}(i,j)\Big\}, \\ -\frac{1}{\pi}\Big\{ & -P\sin\phi_{x_i,y_i}C_{\text{sinx}}(x_i,y_i) \\ & -P\cos\phi_{x_i,y_i}C_{\text{cosx}}(x_i,y_i)\Big\}, \\ 0, & \end{cases} \begin{array}{l} \text{if } x_i \neq x_j \text{ and } y_i = y_j \\ \\ \text{if } x_i = x_j \text{ and } y_i = y_j \\ \\ \text{otherwise} \end{array}$$

$$\frac{\partial m_y^{x_i,y_i}(\boldsymbol{\phi})}{\partial \phi_{x_j,y_j}} = \begin{cases} -\frac{1}{\pi}\Big\{ & P\cos\phi_{x_i,y_i}\cos\phi_{x_j,y_j}D_{my}(i,j) \\ & +P\sin\phi_{x_i,y_i}\sin\phi_{x_j,y_j}D_{my}(i,j)\Big\}, \\ -\frac{1}{\pi}\Big\{ & -P\sin\phi_{x_i,y_i}C_{\text{siny}}(x_i,y_i) \\ & -P\cos\phi_{x_i,y_i}C_{\text{cosy}}(x_i,y_i)\Big\}, \\ 0, & \end{cases} \begin{array}{l} \text{if } y_i \neq y_j \text{ and } x_i = x_j \\ \\ \text{if } y_i = y_j \text{ and } x_i = x_j \\ \\ \text{otherwise,} \end{array} \tag{B.4}$$

where the distance matrices D_{mx} and D_{my} depend only on the horizontal and vertical distances of the grid elements. They are computed as

$$\begin{aligned} D_{mx}(i,j) &= \int_{x'\in r(x_j,y_j)} P(x',y')\frac{1}{x_i - x'}\,\mathrm{d}x', \\ D_{my}(i,j) &= \int_{y'\in r(x_j,y_j)} P(x',y')\frac{1}{y_i - y'}\,\mathrm{d}y', \end{aligned} \tag{B.5}$$

where $r(x_j, y_j)$ is the region representing the grid element (x_j, y_j). Assuming that all the grid elements (x_j, y_j) lay completely inside the pupil (having a constant width d), the distance matrices become

$$\begin{aligned} D_{mx}(i,j) = & \\ & \frac{1}{d}\Big\{\big[(x_i - x_j + d - \epsilon)\log|x_i - x_j + d - \epsilon| - (x_i - x_j - \epsilon)\log|x_i - x_j - \epsilon|\big] \\ & -\big[(x_i - x_j + \epsilon)\log|x_i - x_j + \epsilon| - (x_i - x_j - d + \epsilon)\log|x_i - x_j - d + \epsilon|\big]\Big\}, \end{aligned} \tag{B.6}$$

where ϵ approaches to zero and x_i, x_j are the middle coordinates of grid elements (x_i, y_i) and (x_j, y_j).

In the same way the the derivatives of the cross-terms can be computed,

$$\frac{\partial c_x^{x_i,y_i}(\boldsymbol{\phi})}{\partial \phi_{x_j,y_j}} = \begin{cases} \frac{1}{\pi^3}\Big\{ & C_{\text{sinxy}}(x_i,y_i)\sin\phi_{x_j,y_j} D_{my}(i,j) \\ + & C_{\text{cosxy}}(x_j,y_j)\cos\phi_{x_j,y_j} D_{my}(i,j)\Big\}, & \text{if } x_i = x_j \\ \frac{1}{\pi^3}\Big\{ & -\cos\phi_{x_j,y_j} D_{mx}(i,j) D_{my}(i,j) C_{\text{cosy}}(x_i,y_i) \\ & -\sin\phi_{x_j,y_j} D_{mx}(i,j) D_{my}(i,j) C_{\text{siny}}(x_i,y_i)\Big\}, & \text{if } x_i \neq x_j \end{cases}$$

$$\frac{\partial c_y^{x_i,y_i}(\boldsymbol{\phi})}{\partial \phi_{x_j,y_j}} = \begin{cases} \frac{1}{\pi^3}\Big\{ & C_{\text{sinxy}}(x_i,y_i)\sin\phi_{x_j,y_j} D_{mx}(i,j) \\ + & C_{\text{cosxy}}(x_j,y_j)\cos\phi_{x_j,y_j} D_{mx}(i,j)\Big\}, & \text{if } y_i = y_j \\ \frac{1}{\pi^3}\Big\{ & -\cos\phi_{x_j,y_j} D_{mx}(i,j) D_{my}(i,j) C_{\text{cosx}}(x_i,y_i) \\ & -\sin\phi_{x_j,y_j} D_{mx}(i,j) D_{my}(i,j) C_{\text{sinx}}(x_i,y_i)\Big\}, & \text{if } y_i \neq y_j. \end{cases} \tag{B.7}$$

Thus, the Jacobian is then formed by substituting equations (B.1), (B.4), (B.5), (B.6) and (B.7) into equation (5.3),

$$\begin{aligned} J_x^{n,m}(\boldsymbol{\phi}) &= \frac{\partial m_x^{x_i,y_i}(\boldsymbol{\phi})}{\partial \phi_{x_j,y_j}} + \frac{\partial c_x^{x_i,y_i}(\boldsymbol{\phi})}{\partial \phi_{x_j,y_j}} \\ J_y^{n,m}(\boldsymbol{\phi}) &= \frac{\partial m_y^{x_i,y_i}(\boldsymbol{\phi})}{\partial \phi_{x_j,y_j}} + \frac{\partial c_y^{x_i,y_i}(\boldsymbol{\phi})}{\partial \phi_{x_j,y_j}}. \end{aligned} \tag{B.8}$$

Appendix C

Stellar magnitudes

In astronomy, the stellar brightness is most often expressed as stellar magnitudes. It is defined as (Rigaut, 1994),

$$m_\lambda = -2.5\left[\log_{10}(N_{ph}) - \log_{10}(T\tau\eta\lambda\Delta_\lambda) - 22.7 - ZP_\lambda\right], \tag{C.1}$$

where N_{ph} is the number of photons per square meter per sampling time T, τ is system transmission, η is the detector efficiency, λ is the sensing wavelength, Δ_λ is the sensor bandwidth and ZP_λ is a constant defined for star being spectral type A0.

Next the approximate connection between the stellar magnitude and photon number per subaperture per frame for the configurations used in this thesis are illustrated in table C.1. It is assumed that the sensing wavelength is 0.7 μm, bandwith is $\Delta_\lambda = 0.4$ μm, transmittance is $\tau = 0.25$ and the sensor efficiency is $\eta = 0.4$.

Table C.1: Photon fluxes (1 kHz) for stellar magnitudes

magnitude	n_{ph}/subap.[a]	n_{ph}/subap.[b]	n_{ph}/subap.[c]	n_{ph}/subap.[d]
22	-	-	-	1
20	-	-	-	5
19	-	-	-	15
17	-	-	1	100
16	-	-	5	250
15	-	1	10	500
13	1	10	14	5000
12	2	15	100	10 000
10	15	100	1000	50 000
8	100	1000	5000	500 000
5	1000	10 000	100 000	5 000 000

[a] 8 m telescope, 40×40 subapertures, 1 kHz frame rate
[b] 42 m telescope, 84×84 subapertures, 1 kHz frame rate
[c] 8 m telescope, 8×8 subapertures, 500 Hz frame rate
[d] 8 m telescope, 1 subaperture (global tip-tilt detection), 500 Hz frame rate

Author's contribution

In the following I briefly describe my own contribution in the research reported in this dissertation.

The work has been carried out at European Southern Observatory (ESO) during 2004–2007. I worked under a PhD student contract enabling full time devotion to the research. Before starting the PhD program, I also wrote my master's thesis at ESO (Korkiakoski, 2004).

The first part of my work at ESO, not extensively reported in this thesis, concentrated on updating the OCTOPUS simulation tool. Based on well discussed physical models and instructed by Miska Le Louarn and Christophe Vérinaud, I wrote parallel C-code to simulate a coronagraph (Korkiakoski et al., 2004) and spatial filter for SH-WFS (Korkiakoski et al., 2004). The spatial filter has been used in the works reported in (Vérinaud et al., 2004, 2005). I also wrote code for applying the modal control methods.

The development of OCTOPUS code during my stay at ESO has also been beneficial for the work published in (Le Louarn et al., 2004a,b, 2005b, 2006). Also works using the Matlab interface for OCTOPUS, written by me, has been published (Correia et al., 2006).

After the work dealing mainly with OCTOPUS development, I concentrated on the GLAO study reported here in chapter 4 and in (Korkiakoski et al., 2006). I collaborated with my instructor Miska Le Louarn to find a reasonable set of configurations to simulate. His help was significant also when using OCTOPUS for the reported simulations, and a major part of the simulation code had been written by him. The part of my work dealing with analytic GLAO estimates has been more independent: it was accomplished with the help of the published literature and a kind hint from Andrei Tokovinin for numerical evaluation of his formulas.

When the GLAO study had been concluded as reported here, I continued working with the pyramid WFS. In this part of work I got significant help from Christophe Vérinaud. He provided me with excellent explanations from the principles of the P-WFS, codes to simulate it (both the amplitude mask and phase mask algorithm) and hints to test how the P-WFS sensitivity can be compensated modally.

My first contribution for the pyramid sensor research is the model based reconstruction of P-WFS, published in a refereed journal (Korkiakoski et al., 2007b). I developed independently the linearization of the P-WFS signal, its Jacobian matrix representation and did the corresponding simulations (with OCTOPUS). However, it should be mentioned that besides of the help of Christophe Vérinaud, I owe here to Rodolphe Conan, whose amplitude mask based P-WFS model (see appendix A) I used in that work.

The next major contribution published in this thesis is the P-WFS sensitivity compensation method. When following the hints provided by Christophe Vérinaud, I formulated clearly how the compensation is computed and showed how a priori model of atmosphere is used in the method. Only these additions make it possible to use the method as such in the real time AO applications. This work has been published in a preliminary conference publication (Korkiakoski et al., 2007a) and finally in a refereed journal (Korkiakoski et al., 2008).

References

D. R. Andersen, D. Crampton, K. Szeto, S. Morris, M. Lloyd-Hart, R. Myers, J. Stoesz, A. Tokovinin, T. Butterley, N. M. Milton, J.-P. Véran, and R. Wilson. Modeling a GLAO system for the Gemini Observatory. In E. Brent, L. and B. Domenico, Calia, editors, *Advances in Adaptive Optics II*, volume 6272 of *Proc. SPIE*, page 62725B, July 2006a.

D. R. Andersen, J. Stoesz, S. Morris, M. Lloyd-Hart, D. Crampton, T. Butterley, B. Ellerbroek, L. Jolissaint, N. M. Milton, R. Myers, K. Szeto, A. Tokovinin, J.-P. Véran, and R. Wilson. Performance Modeling of a Wide-Field Ground-Layer Adaptive Optics System. *Publ. Astron. Soc. Pac.*, 118:1574–1590, Nov. 2006b.

C. Arcidiacono. Beam divergence and vertex angle measurements for refractive pyramids. *Optics Communications*, 252:239–246, July 2005.

C. Arcidiacono, M. Lombini, E. Diolaiti, J. Farinato, and R. Ragazzoni. Laboratory testing the layer oriented wavefront sensor for the multiconjugate adaptive optics demonstrator. In B. L. Ellerbroek and D. Bonaccini Calia, editors, *Advances in Adaptive Optics II*, volume 6272 of *Proc. SPIE*, page 627227, July 2006.

H. W. Babcock. The Possibility of Compensating Astronomical Seeing. *Publ. Astron. Soc. Pac.*, 65:229–+, Oct. 1953.

C. Baranec, M. Lloyd-Hart, and N. M. Milton. Ground-Layer Wave Front Reconstruction from Multiple Natural Guide Stars. *The Astrophysical Journal*, 661: 1332–1338, June 2007.

B. J. Bauman, D. T. Gavel, K. E. Waltjen, G. J. Freeze, R. L. Hurd, E. L. Gates, C. E. Max, S. S. Olivier, and D. M. Pennington. Update on optical design of adaptive optics system at Lick Observatory. In R. K. Tyson, D. Bonaccini, and M. C. Roggemann, editors, *Adaptive Optics Systems and Technology II*, volume 4494 of *Proc. SPIE*, pages 19–29, Feb. 2002.

J.-L. Beuzit, M. Feldt, K. Dohlen, D. Mouillet, P. Puget, J. Antici, A. Baruffolo, P. Baudoz, A. Berton, A. Boccaletti, M. Carbillet, J. Charton, R. Claudi, M. Downing, P. Feautrier, E. Fedrigo, T. Fusco, R. Gratton, N. Hubin, M. Kasper, M. Langlois, C. Moutou, L. Mugnier, J. Pragt, P. Rabou, M. Saisse, H. M. Schmid, E. Stadler, M. Turrato, S. Udry, R. Waters, and F. Wildi. SPHERE: A 'Planet Finder' Instrument for the VLT. *The Messenger*, 125:29–+, Sept. 2006.

A. Burvall, E. Daly, S. R. Chamot, and C. Dainty. Linearity of the pyramid wavefront sensor. *Optics Express*, 14:11925–11934, Dec. 2006.

M. Carbillet, C. Vérinaud, B. Femenía, A. Riccardi, and L. Fini. Modelling astronomical adaptive optics - I. The software package CAOS. *Mon. Not. R. Astron. Soc.*, 356:1263–1275, Feb. 2005.

D. C. Chen, S. M. Jones, D. A. Silva, and S. S. Olivier. High-resolution adaptive optics scanning laser ophthalmoscope with dual deformable mirrors. *Journal of the Optical Society of America A*, 24:1305–1312, May 2007.

T. Y. Chew, R. M. Clare, and R. G. Lane. A comparison of the Shack Hartmann and pyramid wavefront sensors. *Optics Communications*, 268:189–195, Dec. 2006.

J. Choi, J. Demmel, I. Dhillon, J. Dongarra, S. Ostrouchov, A. Petitet, K. Stanley, D. Walker, and R. C. Whaley. ScaLAPACK: a portable linear algebra library for distributed memory computers - design issues and performance. *Computer Physics Communications*, 97:1–2, Aug. 1996.

R. M. Clare and R. G. Lane. Wavefront sensing from spatial filtering at the focal plane. In R. K. Tyson and M. Lloyd-Hart, editors, *Astronomical Adaptive Optics Systems and Applications*, volume 5169 of *Proc. SPIE*, pages 43–54, Dec. 2003.

R. M. Clare and R. G. Lane. Comparison of wavefront sensing with the Shack-Hartmann and pyramid sensors. In D. Bonaccini Calia, B. L. Ellerbroek, and R. Ragazzoni, editors, *Advancements in Adaptive Optics*, volume 5490 of *Proc. SPIE*, pages 1211–1222, Oct. 2004.

Y. Clenet, M. E. Kasper, N. Ageorges, C. Lidman, T. Fusco, O. Marco, M. Hartung, D. Mouillet, B. Koehler, G. Rousset, and N. N. Hubin. NACO performance: status after 2 years of operation. In D. Bonaccini Calia, B. L. Ellerbroek, and R. Ragazzoni, editors, *Advancements in Adaptive Optics*, volume 5490 of *Presented at the Society of Photo-Optical Instrumentation Engineers (SPIE) Conference*, pages 107–117, Oct. 2004.

C. Correia, E. Fedrigo, M. Le Louarn, C. Vérinaud, and V. Korkiakoski. Multirate control of high-order adaptive optics systems. In B. L. Ellerbroek and D. C. Bonaccini, editors, *Advances in Adaptive Optics II*, volume 6272 of *Proc. SPIE*, page 62722R, July 2006.

J. B. Costa. Modulation effect of the atmosphere in a pyramid wave-front sensor. *Applied Optics*, 44:60–66, Jan. 2005.

J. B. Costa, R. Ragazzoni, A. Ghedina, M. Carbillet, C. Vérinaud, M. Feldt, S. Esposito, E. Puga, and J. Farinato. Is there need of any modulation in the pyramid wavefront sensor? In P. L. Wizinowich and D. Bonaccini, editors, *Adaptive Optical System Technologies II.*, volume 4839 of *Proc. SPIE*, pages 288–298, Feb. 2003.

J. B. Costa, M. Stumpf, and M. Feldt. Testing a nonmodulated pyramid wavefront sensor. In D. Bonaccini Calia, B. L. Ellerbroek, and R. Ragazzoni, editors, *Advancements in Adaptive Optics*, volume 5490 of *Proc. SPIE*, pages 1304–1314, Oct. 2004.

C. Dessenne, P.-Y. Madec, and G. Rousset. Optimization of a Predictive Controller for Closed-Loop Adaptive Optics. *Applied Optics*, 37:4623–4633, July 1998.

R. Donaldson, D. Bonaccini, J. Brynnel, B. Buzzoni, L. M. Close, B. Delabre, C. DuPuy, J. Farinato, E. Fedrigo, N. N. Hubin, E. Marchetti, S. Stroebele, and S. Tordo. MACAO and its application for the VLT interferometer. In P. L. Wizinowich, editor, *Adaptive Optical Systems Technology*, volume 4007 of *Proc. SPIE*, pages 82–93, July 2000.

F. Eisenhauer, R. Abuter, K. Bickert, F. Biancat-Marchet, H. Bonnet, J. Brynnel, R. D. Conzelmann, B. Delabre, R. Donaldson, J. Farinato, E. Fedrigo, R. Genzel, N. N. Hubin, C. Iserlohe, M. E. Kasper, M. Kissler-Patig, G. J. Monnet, C. Roehrle, J. Schreiber, S. Stroebele, M. Tecza, N. A. Thatte, and H. Weisz. SINFONI - Integral field spectroscopy at 50 milli-arcsecond resolution with the ESO VLT. In M. Iye and A. F. M. Moorwood, editors, *Instrument Design and Performance for Optical/Infrared Ground-based Telescopes*, volume 4841 of *Proc. SPIE*, pages 1548–1561, Mar. 2003.

B. L. Ellerbroek and G. Cochran. Wave optics propagation code for multiconjugate adaptive optics. In R. K. Tyson, D. Bonaccini, and M. C. Roggemann, editors, *Adaptive Optics Systems and Technology II*, volume 4494 of *Proc. SPIe*, pages 104–120, Feb. 2002.

B. L. Ellerbroek and F. Rigaut. Methods for correcting tilt anisoplanatism in laser-guide-star-based multiconjugate adaptive optics. *Journal of the Optical Society of America A*, 18:2539–2547, Oct. 2001.

B. L. Ellerbroek and C. R. Vogel. Simulations of closed-loop wavefront reconstruction for multiconjugate adaptive optics on giant telescopes. In R. K. Tyson and M. Lloyd-Hart, editors, *Astronomical Adaptive Optics Systems and Applications*, volume 5169 of *Proc. SPIE*, pages 206–217, Dec. 2003.

S. Esposito and A. Riccardi. Pyramid Wavefront Sensor behavior in partial correction Adaptive Optic systems. *Astron. Astrophys.*, 369:L9–L12, Apr. 2001.

S. Esposito, O. Feeney, and A. Riccardi. Laboratory test of a pyramid wavefront sensor. In P. L. Wizinowich, editor, *Adaptive Optical Systems Technology*, volume 4007 of *Proc. SPIE*, pages 416–422, July 2000a.

S. Esposito, A. Riccardi, and O. Feeney. Closed-loop performance of pyramid wavefront sensor. In T. D. Steiner and P. H. Merritt, editors, *Laser Weapons Technology*, volume 4034 of *Proc. SPIE*, pages 184–189, July 2000b.

S. Esposito, A. Tozzi, A. Puglisi, E. Pinna, A. Riccardi, S. Busoni, L. Busoni, P. Stefanini, M. Xompero, D. Zanotti, and F. Pieralli. First light AO system

for LBT: toward on-sky operation. In B. L. Ellerbroek and D. Bonaccini Calia, editors, *Advances in Adaptive Optics II*, volume 6272 of *Proc. SPIE*, page 62720A, July 2006.

E. Fedrigo, R. Donaldson, C. Soenke, R. Myers, S. Goodsell, D. Geng, C. Saunter, and N. Dipper. SPARTA: the ESO standard platform for adaptive optics real time applications. In B. L. Ellerbroek and D. Bonaccini Calia, editors, *Advances in Adaptive Optics II*, volume 6272 of *Proc. SPIE*, page 627210, July 2006.

O. Feeney. *Theory and Laboratory Characterisation of Novel Wavefront Sensor for Adaptive Optics Systems*. PhD thesis, National University of Ireland, 2001.

M. Feldt, D. Peter, S. Hippler, T. Henning, J. Aceituno, and M. Goto. PYRAMIR: first on-sky results from an infrared pyramid wavefront sensor. In B. L. Ellerbroek and D. C. Bonaccini, editors, *Advances in Adaptive Optics II*, volume 6272 of *Proc. SPIE*, page 627218, July 2006.

J. R. Fienup. Phase retrieval algorithms: a comparison. *Applied Optics*, 21:2758–2769, Aug. 1982.

R. Foy. The Cone Effect. In N. Ageorges and C. Dainty, editors, *Laser Guide Star Adaptive Optics for Astronomy*, pages 107–+. Kluwer Academic Publishers (Dordrecht), 2000.

D. L. Fried. Statistics of a Geometric Representation of Wavefront Distortion. *Journal of the Optical Society of America (1917-1983)*, 55:1427–1435, 1965.

D. L. Fried. Time-delay-induced mean-square error in adaptive optics. *Journal of the Optical Society of America A*, 7:1224–1227, July 1990.

M. Frigo and S. G. Johnson. The design and implementation of FFTW3. *Proceedings of the IEEE*, 93(2):216–231, 2005. special issue on "Program Generation, Optimization, and Platform Adaptation".

R. Q. Fugate. Two generations of laser-guide-star adaptive-optics experiments at the Starfire Optical Range. *Journal of the Optical Society of America A*, 11:310–324, 1994.

T. Fusco, C. Petit, G. Rousset, J.-M. Conan, and J.-L. Beuzit. Closed-loop experimental validation of the spatially filtered Shack-Hartmann concept. *Optics Letters*, 30:1255–1257, June 2005.

T. Fusco, G. Rousset, J.-F. Sauvage, C. Petit, J.-L. Beuzit, K. Dohlen, D. Mouillet, J. Charton, M. Nicolle, M. Kasper, P. Baudoz, and P. Puget. High-order adaptive optics requirements for direct detection of extrasolar planets: Application to the SPHERE instrument. *Optics Express*, 14:7515–7534, 2006.

T. Fusco, S. Thomas, M. Nicolle, A. Tokovinin, V. Michau, and G. Rousset. Optimization of center of gravity algorithms in a Shack-Hartmann sensor. In B. L. Ellerbroek and D. Bonaccini Calia, editors, *Advances in Adaptive Optics II*, volume 6272 of *Proc. SPIE*, page 627219, July 2006.

D. T. Gavel and D. Wiberg. Toward Strehl-optimizing adaptive optics controllers. In P. L. Wizinowich and D. Bonaccini, editors, *Adaptive Optical System Technologies II*, volume 4839 of *Proc. SPIE*, pages 890–901, Feb. 2003.

E. Gendron and P. Lena. Astronomical adaptive optics. 1: Modal control optimization. *Astron. Astrophys.*, 291:337–347, Nov. 1994.

E. Gendron and P. Lena. Astronomical adaptive optics. II. Experimental results of an optimized modal control. *Astronomy and Astrophysics Supplement*, 111: 153–+, May 1995.

A. Ghedina, M. Cecconi, R. Ragazzoni, J. Farinato, A. Baruffolo, G. Crimi, E. Diolaiti, S. Esposito, L. Fini, M. Ghigo, E. Marchetti, T. Niero, and A. Puglisi. On Sky Test of the Pyramid Wavefront Sensor. In P. L. Wizinowich and D. Bonaccini, editors, *Adaptive Optical System Technologies II*, volume 4839 of *Proc. SPIE*, pages 869–877, Feb. 2003.

R. Gilmozzi and J. Spyromilio. The European Extremely Large Telescope (E-ELT). *The Messenger*, 127:11–+, Mar. 2007.

O. Guyon. Limits of Adaptive Optics for High-Contrast Imaging. *The Astrophysical Journal*, 629:592–614, Aug. 2005.

O. Guyon, B. Gallet, E. A. Pluzhnik, H. Takami, and M. Tamura. High contrast imaging with focal plane wavefront sensing for ground based telescopes. In B. L. Ellerbroek and D. Bonaccini Calia, editors, *Advances in Adaptive Optics II*, volume 6272 of *Proc. SPIE*, page 62723C, July 2006.

M. H. Hayes. *Statistical digital signal processing and modeling*. John Wiley & Sons, Inc., New York, Chichester, Brisbane, Toronto, Signapore, 1996.

E. Hecht. *Optics, 3rd ed.* Addison-Wesley, 1998.

F. Henault, R. Bacon, H. Dekker, B. Delabre, S. Djidel, J.-P. Dubois, N. Hubin, B. Lantz, W. Lau, M. Le Louarn, I. J. Lewis, J.-L. Lizon, J. Lynn, L. Pasquini, R. Reiss, and M. M. Roth. MUSE optomechanical design and performance. In A. F. M. Moorwood and M. Iye, editors, *Ground-based Instrumentation for Astronomy*, volume 5492 of *Proc. SPIE*, pages 909–920, Sept. 2004.

J. A. Johnson, R. Kupke, D. Gavel, and B. Bauman. Pyramid wavefront sensing: theory and component technology development at LAO. In B. L. Ellerbroek and D. C. Bonaccini, editors, *Advances in Adaptive Optics II*, volume 6272 of *Proc. SPIE*, page 62724R, July 2006.

M. Kasper. *Optimization of an adaptive optics system and its application to high-resolution imaging spectroscopy of T Tauri*. PhD thesis, University of Heidelberg, 2000.

R. L. Kendrick, D. S. Acton, and A. L. Duncan. Phase-diversity wave-front sensor for imaging systems. *Applied Optics*, 33:6533–6546, Sept. 1994.

V. Korkiakoski. Parallel simulation of a coronagraph for extremely large telescopes. Master's thesis, Helsinki University of Technology, 2004.

V. Korkiakoski, M. Le Louarn, and C. Vérinaud. Combining spatially filtered Shack-Hartmann wavefront sensing and coronography in closed loop AO simulations. In D. Bonaccini Calia, B. L. Ellerbroek, and R. Ragazzoni, editors, *Advancements in Adaptive Optics*, volume 5490 of *Proc. SPIE*, pages 695–704, Oct. 2004.

V. Korkiakoski, M. Le Louarn, and C. Vérinaud. Simulations of ground-layer adaptive optics for extremely large telescopes. In B. L. Ellerbroek and D. C. Bonaccini, editors, *Advances in Adaptive Optics II*, volume 6272 of *Proc. SPIE*, page 62725A, July 2006.

V. Korkiakoski, C. Vérinaud, and M. Le Louarn. Modal Gain Optimization for Pyramid Wavefront Sensor. In *"Adaptive Optics: Analysis and Methods"*, OSA Technical Digest (CD), 2007a.

V. Korkiakoski, C. Vérinaud, M. Le Louarn, and R. Conan. Comparison between a model-based and a conventional pyramid sensor reconstructor. *Applied Optics*, 46:6176–6184, 2007b.

V. Korkiakoski, C. Vérinaud, and M. Le Louarn. Improving the performance of a pyramid wavefront sensor with modal sensitivity compensation. *Applied Optics*, 47:79–87, 2008.

N. F. Law and R. G. Lane. Wavefront estimation at low light levels. *Optics Communications*, 126:19–24, Feb. 1996.

M. Le Louarn and N. Hubin. Wide-field adaptive optics for deep-field spectroscopy in the visible. *Mon. Not. R. Astron. Soc.*, 349:1009–1018, Apr. 2004.

M. Le Louarn and N. Hubin. Improving the seeing with wide-field adaptive optics in the near-infrared. *Mon. Not. R. Astron. Soc.*, 365:1324–1332, Feb. 2006.

M. Le Louarn, N. Hubin, M. Sarazin, and A. Tokovinin. New challenges for adaptive optics: extremely large telescopes. *Mon. Not. R. Astron. Soc.*, 317:535–544, Sept. 2000.

M. Le Louarn, C. Vérinaud, V. Korkiakoski, and E. Fedrigo. Parallel simulation tools for AO on ELTs. In D. Bonaccini Calia, B. L. Ellerbroek, and R. Ragazzoni, editors, *Advancements in Adaptive Optics*, volume 5490 of *Proc. SPIE*, pages 705–712, Oct. 2004a.

M. Le Louarn, C. Vérinaud, N. Yaitskova, V. Korkiakoski, E. Fedrigo, and N. N. Hubin. Simulations of (MC)AO for a 100-m telescope. In D. Bonaccini Calia, B. L. Ellerbroek, and R. Ragazzoni, editors, *Advancements in Adaptive Optics*, volume 5490 of *Proc. SPIE*, pages 649–660, Oct. 2004b.

M. Le Louarn, N. Hubin, and B. Delabre. Adaptive Optics for MUSE. In W. Brandner and M. E. Kasper, editors, *Science with Adaptive Optics*, Proceedings of the ESO Workshop Held at Garching, Germany, pages 36–+, 2005a.

M. Le Louarn, C. Vérinaud, and V. Korkiakoski. Simulation of MCAO on (extremely) large telescopes. *C. R. Physique*, 11:1070–1080, Dec. 2005b.

M. Le Louarn, C. Vérinaud, V. Korkiakoski, N. Hubin, and E. Marchetti. Adaptive optics simulations for the European Extremely Large Telescope. In B. L. Ellerbroek and D. C. Bonaccini, editors, *Advances in Adaptive Optics II*, volume 6272 of *Proc. SPIE*, page 627234, July 2006.

B. Le Roux. Optimal control law for Adaptive Optics, application to MCAO and XAO. In *EAS Publications Series*, volume 22 of *EAS Publications Series*, pages 139–150, 2006.

B. Le Roux and M. Carbillet. Advantage of a predictive control law for extreme adaptive optics imaging. In C. Aime and F. Vakili, editors, *IAU Colloq. 200: Direct Imaging of Exoplanets: Science & Techniques*, pages 597–602, 2006.

B. Le Roux, J.-M. Conan, C. Kulcsár, H.-F. Raynaud, L. M. Mugnier, and T. Fusco. Optimal control law for classical and multiconjugate adaptive optics. *Journal of the Optical Society of America A*, 21:1261–1276, July 2004.

M. Lloyd-Hart and N. M. Milton. Multi-conjugate adaptive optics for a new generation of giant telescopes. In J. R. P. Angel and R. Gilmozzi, editors, *Future Giant Telescopes*, volume 4840 of *Proc. SPIE*, pages 18–26, Jan. 2003.

D. P. Looze. Minimum variance control structure for adaptive optics systems. *Journal of the Optical Society of America A*, 23:603–612, Mar. 2006.

D. P. Looze, M. Kasper, S. Hippler, O. Beker, and R. Weiss. Optimal Compensation and Implementation for Adaptive Optics Systems. *Experimental Astronomy*, 15: 67–88, Apr. 2003.

B. Macintosh, J. Graham, D. Palmer, R. Doyon, D. Gavel, J. Larkin, B. Oppenheimer, L. Saddlemyer, J. K. Wallace, B. Bauman, J. Evans, D. Erikson, K. Morzinski, D. Phillion, L. Poyneer, A. Sivaramakrishnan, R. Soummer, S. Thibault, and J.-P. Veran. The Gemini Planet Imager. In B. L. Ellerbroek and D. Bonaccini Calia, editors, *Advances in Adaptive Optics II*, volume 6272 of *Proc. SPIE*, page 62720L, July 2006.

R. B. Makidon, A. Sivaramakrishnan, M. D. Perrin, L. C. Roberts, Jr., B. R. Oppenheimer, R. Soummer, and J. R. Graham. An Analysis of Fundamental Waffle Mode in Early AEOS Adaptive Optics Images. *Publ. Astron. Soc. Pac.*, 117: 831–846, Aug. 2005.

E. Marchetti, N. N. Hubin, E. Fedrigo, J. Brynnel, B. Delabre, R. Donaldson, F. Franza, R. Conan, M. Le Louarn, C. Cavadore, A. Balestra, D. Baade, J.-L. Lizon, R. Gilmozzi, G. J. Monnet, R. Ragazzoni, C. Arcidiacono, A. Baruffolo, E. Diolaiti, J. Farinato, E. Vernet-Viard, D. J. Butler, S. Hippler, and A. Amorin. MAD the ESO multi-conjugate adaptive optics demonstrator. In P. L. Wizinowich and D. Bonaccini, editors, *Adaptive Optical System Technologies II*, volume 4839 of *Proc. SPIE*, pages 317–328, Feb. 2003.

E. Marchetti, R. Brast, B. Delabre, R. Donaldson, E. Fedrigo, C. Frank, N. Hubin, J. Kolb, M. Le Louarn, J.-L. Lizon, S. Oberti, F. Quirós-Pacheco, R. Reiss, J. Santos, S. Tordo, A. Baruffolo, P. Bagnara, A. Amorim, and J. Lima. MAD star oriented: laboratory results for ground layer and multi-conjugate adaptive optics. In B. L. Ellerbroek and D. Bonaccini Calia, editors, *Advances in Adaptive Optics II*, volume 6272 of *Proc. SPIE*, page 62720O, July 2006.

E. Marchetti, R. Brast, B. Delabre, R. Donaldson, E. Fedrigo, C. Frank, N. Hubin, J. Kolb, M. L. Louarn, J. L. Lizon, S. Oberti, R. Reiss, C. Soenke, S. Tordo, A. Baruffolo, P. Bagnara, A. Amorim, and J. Lima. "MAD on-sky results in star oriented mode". In *"Adaptive Optics: Analysis and Methods"*, OSA Technical Digest (CD), 2007.

C. E. Max, S. S. Olivier, H. W. Friedman, J. An, K. Avicola, B. V. Beeman, H. D. Bissinger, J. M. Brase, G. V. Erbert, D. T. Gavel, K. Kanz, M. C. Liu, B. Macintosh, K. P. Neeb, J. Patience, and K. E. Waltjen. Image Improvement from a Sodium-Layer Laser Guide Star Adaptive Optics System. *Science*, 277:1649–1652, Sept. 1997.

R. Muradore, E. Fedrigo, and C. Correia. LQ control design for adaptive optics systems based on MIMO identified model. In E. Brent, L. and B. Domenico, Calia, editors, *Advances in Adaptive Optics II*, volume 6272 of *Proc. SPIE*, page 62725H, July 2006.

J. Nelson and G. H. Sanders. TMT status report. In L. M. Stepp, editor, *Ground-based and Airborne Telescopes*, volume 6267 of *Proc. SPIE*, page 626728, July 2006.

M. Nicolle. *Analyse de front d'onde pour les optiques adaptatives de nouvelle génération*. PhD thesis, Université Parix XI, 2006.

M. Nicolle, T. Fusco, G. Rousset, and V. Michau. Improvement of Shack-Hartmann wave-front sensor measurement for extreme adaptive optics. *Optics Letters*, 29: 2743–2745, Dec. 2004.

M. Nicolle, T. Fusco, V. Michau, G. Rousset, and J.-L. Beuzit. Performance analysis of multi-object wave-front sensing concepts for GLAO. In R. K. Tyson and M. Lloyd-Hart, editors, *Astronomical Adaptive Optics Systems and Applications II*, volume 5903 of *Proc. SPIE*, pages 248–259, Aug. 2005.

M. Nicolle, T. Fusco, V. Michau, G. Rousset, and J.-L. Beuzit. Optimization of star-oriented and layer-oriented wavefront sensing concepts for ground layer adaptive optics. *Journal of the Optical Society of America A*, 23:2233–2245, Sept. 2006.

R. J. Noll. Zernike polynomials and atmospheric turbulence. *Journal of the Optical Society of America (1917-1983)*, 66:207–211, 1976.

P. S. Pacheco. *Parallel programming with MPI*. Morgan Kaufmann Publishers, Inc, 1997.

R. N. Paschall and D. J. Anderson. Linear quadratic Gaussian control of a deformable mirror adaptive optics system with time-delayed measurements. *Applied Optics*, 32:6347–6358, Nov. 1993.

J. Paufique, P. Biereichel, B. Delabre, R. Donaldson, R. Esteves, E. Fedrigo, P. Gigan, D. Gojak, N. Hubin, M. Kasper, U. Käufl, J. L. Lizon, E. Marchetti, S. Oberti, J. F. Pirard, E. Pozna, J. Santos, S. Stroebele, and S. Tordo. On-sky results of the adaptive optics MACAO for the new IR-spectrograph CRIRES at VLT. In B. L. Ellerbroek and D. Bonaccini Calia, editors, *Advances in Adaptive Optics II*, volume 6272 of *Proc. SPIE*, page 627216, July 2006.

C. Petit, F. Quiros-Pacheco, J.-M. Conan, C. Kulcsar, H.-F. Raynaud, T. Fusco, and G. Rousset. Kalman-filter-based control for adaptive optics. In D. Bonaccini Calia, B. L. Ellerbroek, and R. Ragazzoni, editors, *Advancements in Adaptive Optics*, volume 5490 of *Proc. SPIE*, pages 1414–1425, Oct. 2004.

D. W. Phillion and K. Baker. Two-sided pyramid wavefront sensor in the direct phase mode. In B. L. Ellerbroek and D. C. Bonaccini, editors, *Advances in Adaptive Optics II*, volume 6272 of *Proc. SPIE*, July 2006.

P. Piatrou and M. Roggemann. Performance analysis of Kalman filter and minimum variance controllers for multi conjugate adaptive optics. In M. T. Gruneisen, J. D. Gonglewski, and M. K. Giles, editors, *Advanced Wavefront Control: Methods, Devices, and Applications III*, volume 5894 of *Proc. SPIE*, pages 288–296, Aug. 2005.

L. A. Poyneer and B. Macintosh. Spatially-filtered wave-front sensor for high-order adaptive optics. *Journal of the Optical Society of America A*, 21:810–819, 2004.

L. A. Poyneer and J.-P. Véran. Optimal modal Fourier-transform wavefront control. *Journal of the Optical Society of America A*, 22:1515–1526, Aug. 2005.

F. Quiros-Pacheco. *Reconstruction and control laws for multi-conjugate adaptive optics in astronomy.* PhD thesis, PhD Thesis, London: Imperial College, [2007] 247 p., 2007.

F. Quiros-Pacheco, C. Petit, J.-M. Conan, T. Fusco, and E. Marchetti. Control laws for a multiconjugate adaptive optics system. In D. Bonaccini Calia, B. L. Ellerbroek, and R. Ragazzoni, editors, *Advancements in Adaptive Optics*, volume 5490 of *Proc. SPIE*, pages 1460–1471, Oct. 2004.

R. Racine and B. L. Ellerbroek. Profiles of nighttime turbulence above Mauna Kea and isoplanatism extension in adaptive optics. In R. K. Tyson and R. Q. Fugate, editors, *Adaptive Optical Systems and Applications*, volume 2534 of *Proc. SPIE*, pages 248–257, Aug. 1995.

R. Ragazzoni. Pupil plane wavefront sensing with an oscillating prism. *Journal of Modern Optics*, 43:289–293, Feb. 1996.

R. Ragazzoni and J. Farinato. Sensitivity of a pyramidic Wave Front sensor in closed loop Adaptive Optics. *Astron. Astrophys.*, 350:L23–L26, Oct. 1999.

R. Ragazzoni, E. Diolaiti, and E. Vernet. A pyramid wavefront sensor with no dynamic modulation. *Optics Communications*, 208:51–60, July 2002.

A. Riccardi, N. Bindi, R. Ragazzoni, E. S., and P. Stefanini. Laboratory characterization of a foucault-like wavefront sensor for adaptive optics. In D. Bonaccini Calia and R. K. Tyson, editors, *Adaptive Optical System Technologies*, volume 3353 of *Proc. SPIE*, pages 941–951, 1998.

F. Rigaut. Ground Conjugate Wide Field Adaptive Optics for the ELTs. In E. Vernet, R. Ragazzoni, S. Esposito, and N. Hubin, editors, *Beyond conventional adaptive optics : a conference devoted to the development of adaptive optics for extremely large telescopes. Proceedings of the Topical Meeting held May 7-10, 2001, Venice, Italy. Garching, Germany: European Southern Observatory, 2002 ESO Conference and Workshop Proceedings, ISBN 3923524617*, volume 58, pages 11–+, 2002.

F. Rigaut. Astronomical reference sources. In D. M. Alloin and J.-M. Mariotti, editors, *Adaptive Optics for Astronomy*, pages 163–174. NATO ASI Series, 1994.

F. J. Rigaut, B. L. Ellerbroek, and R. Flicker. Principles, limitations, and performance of multiconjugate adaptive optics. In P. L. Wizinowich, editor, *Adaptive Optical Systems Technology*, volume 4007 of *Proc. SPIE*, pages 1022–1031, July 2000.

F. Roddier. Imaging through the atmosphere. In F. Roddier, editor, *Adaptive Optics in Astronomy*, pages 9–22. Cambridge university press, 1999a.

F. Roddier. Theoretical aspects. In F. Roddier, editor, *Adaptive Optics in Astronomy*, pages 25–56. Cambridge university press, 1999b.

F. Roddier. Historical context. In F. Roddier, editor, *Adaptive Optics in Astronomy*, pages 3–7. Cambridge university press, 1999c.

F. Roddier and F. Rigaut. The UH-CFHT systems. In F. Roddier, editor, *Adaptive Optics in Astronomy*, pages 205–234. Cambridge university press, 1999.

G. Rousset. Wave-front sensors. In F. Roddier, editor, *Adaptive Optics in Astronomy*, pages 91–130. Cambridge university press, 1999.

G. Rousset and J.-L. Beuzit. The COME-ONE/ADONIS systems. In F. Roddier, editor, *Adaptive Optics in Astronomy*, pages 171–203. Cambridge university press, 1999.

G. Rousset, F. Lacombe, P. Puget, E. Gendron, R. Arsenault, P. Y. Kern, D. Rabaud, P.-Y. Madec, N. N. Hubin, G. Zins, E. Stadler, J. Charton, P. Gigan, and P. Feautrier. Status of the VLT Nasmyth adaptive optics system (NAOS). In P. L. Wizinowich, editor, *Adaptive Optical Systems Technology*, volume 4007 of *Proc. SPIE*, pages 72–81, July 2000.

D. G. Sandler. The design of laser beacon ao systems. In F. Roddier, editor, *Adaptive Optics in Astronomy*, pages 271–330. Cambridge university press, 1999a.

D. G. Sandler. Overview of adaptive optics with laser beacons. In F. Roddier, editor, *Adaptive Optics in Astronomy*, pages 255–270. Cambridge university press, 1999b.

M. Séchaud. Wave-front compensation devices. In F. Roddier, editor, *Adaptive Optics in Astronomy*, pages 57–90. Cambridge university press, 1999.

J. A. Stoesz. Constraining the GLAO parameter space with turbulence profile models. In B. L. Ellerbroek and D. Bonaccini Calia, editors, *Advances in Adaptive Optics II*, volume 6272 of *Proc. SPIE*, page 62724M, July 2006.

J. A. Stoesz, L. Jolissaint, J.-P. Veran, and J. LeDue. An analytic model for natural guide star wide-field adaptive optics. In D. Bonaccini Calia, B. L. Ellerbroek, and R. Ragazzoni, editors, *Advancements in Adaptive Optics*, volume 5490 of *Proc. SPIE*, pages 713–720, Oct. 2004a.

J. A. Stoesz, J.-P. Veran, F. J. Rigaut, G. Herriot, L. Jolissaint, D. Frenette, J. Dunn, and M. Smith. Evaluation of the on-sky performance of Altair. In D. Bonaccini Calia, B. L. Ellerbroek, and R. Ragazzoni, editors, *Advancements in Adaptive Optics*, volume 5490 of *Proc. SPIE*, pages 67–78, Oct. 2004b.

S. Ströbele, R. Arsenault, R. Bacon, R. Biasi, D. Bonaccini-Calia, M. Downing, R. D. Conzelmann, B. Delabre, R. Donaldson, M. Duchateau, S. Esposito, E. Fedrigo, D. Gallieni, W. K. P. Hackenberg, N. Hubin, M. Kasper, M. Kissler-Patig, M. Le Louarn, R. McDermid, S. Oberti, J. Paufique, A. Riccardi, R. Stuik, and E. Vernet. The ESO Adaptive Optics Facility. In B. L. Ellerbroek and D. Bonaccini Calia, editors, *Advances in Adaptive Optics II*, volume 6272 of *Proc. SPIE*, page 62720B, July 2006.

S. Thomas, T. Fusco, A. Tokovinin, M. Nicolle, V. Michau, and G. Rousset. Comparison of centroid computation algorithms in a Shack-Hartmann sensor. *Mon. Not. R. Astron. Soc.*, 371:323–336, Sept. 2006.

A. Tokovinin. Seeing improvement with ground-layer adaptive optics. *Astron. Astrophys.*, 116:941–951, 2004.

A. Tokovinin, M. Le Louarn, and M. Sarazin. Isoplanatism in a multiconjugate adaptive optics system. *Journal of the Optical Society of America A*, 17:1819–1827, 2000.

A. Tokovinin, S. Thomas, B. Gregory, N. van der Bliek, P. Schurter, R. Cantarutti, and E. Mondaca. Design of ground-layer turbulence compensation with a Rayleigh beacon. In D. Bonaccini Calia, B. L. Ellerbroek, and R. Ragazzoni, editors, *Advancements in Adaptive Optics*, volume 5490 of *Proc. SPIE*, pages 870–878, Oct. 2004.

A. A. Tokovinin, B. Gregory, H. E. Schwarz, V. Terebizh, and S. Thomas. A visible-light AO system for the 4.2m SOAR telescope. In P. L. Wizinowich and D. Bonaccini, editors, *Adaptive Optical System Technologies II*, volume 4839 of *Proc. SPIE*, pages 673–680, Feb. 2003.

T. Travouillon, J. S. Lawrence, and L. Jolissaint. Ground-layer adaptive optics performance in Antarctica. In D. Bonaccini Calia, B. L. Ellerbroek, and R. Ragazzoni, editors, *Advancements in Adaptive Optics*, Proc. SPIE, pages 934–942, Oct. 2004.

R. K. Tyson. *Principles of Adaptive Optics*. Academic Press, Inc., San Diego, 1991.

M. A. van Dam, D. Le Mignant, and B. A. Macintosh. Performance of the Keck Observatory Adaptive-Optics System. *Applied Optics*, 43:5458–5467, Oct. 2004.

J.-P. Véran, F. Rigaut, H. Maître, and D. Rouan. Estimation of the adaptive optics long-exposure point-spread function using control loop data. *Journal of the Optical Society of America A*, 14:3057–3069, Nov. 1997.

C. Vérinaud. On the nature of the measurements provided by a pyramid wave-front sensor. *Optics Communications*, 233:27–38, Mar. 2004.

C. Vérinaud, M. Le Louarn, V. Korkiakoski, and J. Braud. Simulations of extreme AO: a comparison between Shack-Hartmann and pyramid-based systems. In D. Bonaccini Calia, B. L. Ellerbroek, and R. Ragazzoni, editors, *Advancements in Adaptive Optics*, volume 5490 of *Proc. SPIE*, pages 1177–1188, Oct. 2004.

C. Vérinaud, M. Le Louarn, V. Korkiakoski, and M. Carbillet. Adaptive optics for high-contrast imaging: pyramid sensor versus spatially filtered Shack-Hartmann sensor. *Mon. Not. R. Astron. Soc.*, 357:L26–L30, Feb. 2005.

C. Vérinaud, N. Hubin, M. Kasper, J. Antichi, P. Baudoz, J.-L. Beuzit, A. Boccaletti, A. Chalabaev, K. Dohlen, E. Fedrigo, C. Correia Da Silva, M. Feldt, T. Fusco, A. Gandorfer, R. Gratton, H. Kuntschner, F. Kerber, R. Lenzen, P. Martinez, E. Le Coarer, A. Longmore, D. Mouillet, R. Navarro, J. Paillet, P. Rabou, F. Rahoui, F. Selsis, H. M. Schmid, R. Soummer, D. Stam, C. Thalmann, J. Tinbergen, M. Turatto, and N. Yaitskova. The EPICS project for the European Extremely Large Telescope: outcome of the Planet Finder concept study for OWL. In B. L. Ellerbroek and D. Bonaccini Calia, editors, *Advances in Adaptive Optics II*, volume 6272 of *Proc. SPIE*, page 62720M, July 2006.

E. Vernet, M. Kasper, C. Vérinaud, E. Fedrigo, S. Tordo, N. Hubin, S. Esposito, E. Pinna, A. Puglisi, A. Tozzi, A. G. Basden, S. J. Goodsell, G. D. Love, and R. M. Myers. Extreme adaptive optics system optimization with the high order test bench. In B. L. Ellerbroek and D. Bonaccini Calia, editors, *Advances in Adaptive Optics II*, volume 6272 of *Proc. SPIE*, page 62722K, July 2006.

E. Vernet-Viard, C. Arcidiacono, P. Bagnara, A. Baruffolo, E. Diolaiti, J. Farinato, M. Lombini, and R. Ragazzoni. Layer-oriented wavefront sensor for a multiconjugate adaptive optics demonstrator. *Optical Engineering*, 44:6601–+, Sept. 2005.

J. Y. Wang and J. K. Markey. Modal compensation of atmospheric turbulence phase distortion. *Journal of the Optical Society of America (1917-1983)*, 68:78–87, 1978.

D. Wiberg, L. Johnson, and D. Gavel. Adaptive optics control of wind blown turbulence via translation and prediction. In B. L. Ellerbroek and D. Bonaccini Calia,

editors, *Advances in Adaptive Optics II*, volume 6272 of *Proc. SPIE*, page 62722X, July 2006.

D. M. Wiberg, C. E. Max, and D. T. Gavel. Geometric view of adaptive optics control. *Journal of the Optical Society of America A*, 22:870–880, May 2005.

W. J. Wild. Predictive optimal estimators for adaptive-optics systems. *Optics Letters*, 21:1433–1435, Sept. 1996.

A. Wirth, J. Navetta, D. Looze, S. Hippler, A. Glindemann, and D. Hamilton. Real-Time Modal Control Implementation for Adaptive Optics. *Applied Optics*, 37:4586–4597, July 1998.

P. L. Wizinowich, D. Le Mignant, A. H. Bouchez, R. D. Campbell, J. C. Y. Chin, A. R. Contos, M. A. van Dam, S. K. Hartman, E. M. Johansson, R. E. Lafon, H. Lewis, P. J. Stomski, D. M. Summers, C. G. Brown, P. M. Danforth, C. E. Max, and D. M. Pennington. The W. M. Keck Observatory Laser Guide Star Adaptive Optics System: Overview. *Publ. Astron. Soc. Pac.*, 118:297–309, Feb. 2006.

O. Wulff and D. Looze. Nonlinear control for pyramid sensors in adaptive optics. In B. L. Ellerbroek and D. C. Bonaccini, editors, *Advances in Adaptive Optics II*, volume 6272 of *Proc. SPIE*, 2006.

HELSINKI UNIVERSITY OF TECHNOLOGY CONTROL ENGINEERING

Editor: H. Koivo

Report 143 Tenno, A.
Modelling and Evaluation of Valve-Regulated Lead-Acid Batteries. September 2004.

Report 144 Hyötyniemi, H.
Hebbian Neuron Grids: System Theoretic Approach. September 2004.

Report 145 Hyötyniemi, H. (ed.)
Complex Systems: Science at the Edge of Chaos - Collected papers of the Spring 2003 postgraduate seminar. October 2004.

Report 146 Paanasalo, J.
Modelling and Control of Printing Paper Surface Winding. June 2005.

Report 147 Mohamed, F.
Microgrid Modelling and Simulation. March 2006.

Report 148 Mäenpää, T.
Robust Model Predictive Control for Cross-Directional Processes. May 2006.

Report 149 Kantola, K.
Modelling, Estimation and Control of Electroless Nickel Plating Process of Printed Circuit Board Manufacturing. March 2006.

Report 150 Virtanen, T.
Fault Diagnostics and Vibration Control of Paper Winders. June 2006.

Report 151 Hyötyniemi, H.
Neocybernetics in Biological Systems. August 2006.

Report 152 Hasu, V.
Radio Resource Management in Wireless Communication: Beamforming, Transmission Power Control, and Rate Allocation. June 2007.

Report 153 Hrb•ek, J.
Active Control of Rotor Vibration by Model Predictive Control - A simulation study. May 2007.

Report 154 Mohamed, F. A.
Microgrid Modelling and Online Management. January 2008.

Report 155 Eriksson, L., Elmusrati, M., Pohjola, M. (eds.)
Introduction to Wireless Automation - Collected papers of the spring 2007 postgraduate seminar. April 2008.

Report 156 Korkiakoski, V.
Improving the Performance of Adaptive Optics Systems with Optimized Control Methods. April 2008.

ISBN 978-951-22-9411-4

ISSN 0356-0872

Yliopistopaino, Helsinki 2008